DISS. ETH NO. 28377

First-principles investigation of chemical disorder effects on the magnetic properties in $L1_0$-FeNi

A thesis submitted to attain the degree of

DOCTOR OF SCIENCES of ETH ZURICH
(Dr. sc. ETH Zurich)

presented by

Ankit Izardar

M.Sc. in Materials Science and Simulation, Interdisciplinary Centre for Advanced
Materials Simulation (ICAMS), Ruhr-Universität Bochum

born on 05.04.1990

citizen of India

accepted on the recommendation of

Prof. Dr. Claude Ederer, examiner
Prof. Dr. Stefano Sanvito, co-examiner
Prof. Dr. Jörg F. Löffler, co-examiner

2022

Ankit Izardar

First-principles investigation of chemical disorder effects on the magnetic properties in $L1_0$-FeNi

Zürich, March 2022

Dedicated to the loving memory of my mother, Meena Izardar

1968 – 2019

ABSTRACT

The ever increasing demand for highly energy-efficient devices has accelerated research into the development of new as well as the improvement of existing functional materials. In particular, functional magnetic materials, for example, permanent magnets, which form crucial components in the devices used for electric power production and conversion are of vital importance in this quest. Recently, there has been a huge increase in demand for permanent magnets containing cheap and abundant elements due to the increasing use of renewable energy sources such as wind, tidal and hydro. At present, rare-earth-based magnets account for the majority of the global sales, but in the past years, there has been a huge fluctuation in price and uncertainty in the supply of the rare-earth elements, which makes these magnets unsustainable for future use. Thus, in this context, it is of interest to develop magnets with performance in between cheap magnets like transition-metal-based ferrite, AlNiCo, etc. and the rather expensive rare-earth-based magnets such as $Nd_2Fe_{14}B$ and $SmCo_5$. Such "mid-range magnets" can be used in applications where the high performance of the rare-earth-based magnets is not necessarily required but are used anyways due to the absence of permanent magnet with moderate performance and, therefore, leading to high costs.

Quantum mechanical methods based density functional theory (DFT) are a powerful tool to accurately calculate magnetic properties such as saturation magnetization, magneto-crystalline anisotropy energy (MAE) and the exchange interactions, which are important in determining the performance of a permanent magnet. In this thesis, I explore the magnetic properties of a promising rare-earth free permanent magnet candidate, $L1_0$-FeNi, by employing DFT calculations. In particular, I investigate the effect of chemical disorder on the magnetic properties of $L1_0$-FeNi, since the synthesis of fully ordered samples is extremely challenging. To model the chemical disorder, I employ supercell averaging technique to take into account the effect of local symmetry-breaking of a specific chemical environment around an individual atom. These effects are not included in effective medium approaches such as coherent potential approximation often employed to treat the chemical disorder in random alloys. I show that such effects are of utmost importance when investigating the effect of increasing Fe-content on the MAE in $L1_0$-FeNi.

In the first project of this thesis, I present a systematic study of the coupling between magnetic and chemical degrees of freedom in $L1_0$-FeNi. Most importantly, I examine how the degree of chemical order affects the MAE and demonstrate that a reduction in the chemical disorder by about 25% does not lead to a significant decrease in the MAE.

Moreover, I show that the MAE and the Fe orbital moment anisotropy (OMA) are correlated, which provides an avenue to investigate how local chemical environment leading to high OMA can be used to further optimize the MAE in $L1_0$-FeNi. This lays the foundation for my second project which was done in collaboration with Mayan Si, a master student at ETH Zurich, supervised by me.

In the second project, we focus on how the MAE in $L1_0$-FeNi depends on specific local chemical environment and stoichiometry and whether it is possible to further increase the MAE by optimizing the composition and distribution of constituent elements. Our investigation reveals that it is indeed possible to design an optimized structure with an increased MAE based on the favourable local chemical environment as a guide. Based on this analysis, we then demonstrate that the MAE for structures with 62.5% Fe-content increases by about 25% relative to the case of a fully ordered equiatomic structure which confirms previous experimental studies. I then perform a detailed study of the correlation between the local chemical environment and the OMA values and find that it is unlikely that a detailed quantitative understanding of the MAE can be achieved.

Furthermore, I incorporate the effect of electron-electron interactions present in rather localized d-orbitals in Fe and Ni on the MAE in $L1_0$-FeNi by employing DFT$+U$ calculations. This study reveals that the electron-electron Coulomb interaction controlled by the parameter U can have a significant impact on the magnetic properties, in particular, the MAE in $L1_0$-FeNi alloy.

In the final project of my thesis, I study the effect of chemical disorder on the magnetic exchange interactions and consequently the Curie temperature in $L1_0$-FeNi. I demonstrate that the variations in the local chemical environment can have a significant effect on the magnetic exchange interactions. To measure the impact of such variations in the magnetic exchange couplings, I employ Monte-Carlo simulations and perform a model study of the Heisenberg model with first nearest neighbour interactions sampled from Gaussian distributions on an fcc lattice, and demonstrate that the variation occurring in the magnetic exchange coupling due to the chemical disorder can lead to a strong reduction in T_c.

Finally, I summarize and conclude my thesis and give a perspective for the $L1_0$-FeNi as a rare-earth free permanent magnet.

ZUSAMMENFASSUNG

Die ständig steigende Nachfrage nach hoch energieeffizienten Geräten hat die Forschung zur Entwicklung und Verbesserung von Funktionsmaterialien beschleunigt. Insbesondere funktionelle magnetische Werkstoffe, z. B. Dauermagnete, die entscheidende Komponenten in Geräten für die Stromerzeugung und -umwandlung darstellen, sind bei dieser Suche von entscheidender Bedeutung. In letzter Zeit ist die Nachfrage nach Dauermagneten, die billige und reichlich vorhandene Elemente enthalten, aufgrund der zunehmenden Nutzung erneuerbarer Energiequellen wie Wind-, Gezeiten- und Wasserkraft stark gestiegen. Gegenwärtig machen Magnete auf der Basis von Seltenen Erden den Großteil des weltweiten Absatzes aus, aber in den letzten Jahren gab es enorme Preisschwankungen und Unsicherheiten bei der Versorgung mit Seltenen Erden, was diese Magnete für die Zukunft unbrauchbar macht. In diesem Zusammenhang besteht das derzeitige Interesse darin, Magnete zu entwickeln, deren Leistung zwischen billigen Magneten wie Ferriten auf Übergangsmetallbasis, AlNiCo usw. und den recht teuren Magneten auf Seltenerdbasis wie $Nd_2Fe_{14}B$ und $SmCo_5$ liegt. Solche "Mittelbereichsmagnete" können in Anwendungen eingesetzt werden, bei denen die hohe Leistung der Magnete auf Seltenerdbasis nicht unbedingt erforderlich ist, die aber dennoch verwendet werden, weil es keine Permanentmagnete mit mäßiger Leistung gibt, was zu hohen Kosten führt.

Quantenmechanische Methoden auf der Grundlage der Dichtefunktionaltheorie (DFT) sind ein leistungsfähiges Werkzeug zur genauen Berechnung magnetischer Eigenschaften wie Sättigungsmagnetisierung, magnetokristalline Anisotropie-Energie (MAE) und Austauschwechselwirkungen, die für die Leistung eines Dauermagneten wichtig sind. In meiner Dissertation untersuche ich die magnetischen Eigenschaften eines vielversprechenden Kandidaten für einen freien Dauermagneten mit seltenen Erden, $L1_0$-FeNi, mit Hilfe von DFT-Berechnungen. Insbesondere untersuche ich die Auswirkungen chemischer Unordnung auf die magnetischen Eigenschaften von $L1_0$-FeNi, da die Synthese vollständig geordneter Proben äußerst schwierig ist. Um die chemische Unordnung zu modellieren, setze ich die Technik der Superzellen-Mittelung ein, um den Effekt der lokalen Symmetriebrechung einer spezifischen chemischen Umgebung um ein einzelnes Atom zu berücksichtigen. Diese Effekte sind in den Ansätzen des effektiven Mediums, wie z. B. der Näherung des kohärenten Potenzials, die häufig zur Behandlung der chemischen Unordnung in Zufallslegierungen verwendet werden, nicht enthalten. Ich zeige, dass solche Effekte von größter Bedeutung sind, wenn man die Auswirkungen eines steigenden Fe-Gehalts auf die MAE in $L1_0$-FeNi untersucht.

Im ersten Projekt dieser Arbeit präsentiere ich eine systematische Untersuchung der Kopplung zwischen magnetischen und chemischen Freiheitsgraden in $L1_0$-FeNi. Vor allem untersuche ich, wie sich der chemische Ordnungsgrad auf die MAE auswirkt und zeige, dass eine Verringerung der chemischen Unordnung um etwa 25% nicht zu einer signifikanten Abnahme der MAE führt. Darüber hinaus zeige ich, dass die MAE und die Fe-Orbitalmomentanisotropie (OMA) korreliert sind, was einen Weg eröffnet, um zu untersuchen, wie die lokale chemische Umgebung, die zu einer hohen OMA führt, zur weiteren Optimierung der MAE in $L1_0$-FeNi genutzt werden kann. Dies bildet die Grundlage für mein zweites Projekt, das in Zusammenarbeit mit Mayan Si, einer Masterstudentin an der ETH Zürich, unter meiner Leitung durchgeführt wurde.

Im zweiten Projekt konzentrieren wir uns auf die Frage, wie die MAE in $L1_0$-FeNi von der spezifischen lokalen chemischen Umgebung und der Stöchiometrie abhängt und ob es möglich ist, die MAE durch Optimierung der Zusammensetzung und Verteilung der Bestandteile weiter zu erhöhen. Unsere Untersuchung zeigt, dass es in der Tat möglich ist, eine optimierte Struktur mit einer erhöhten MAE zu entwerfen, die auf der günstigen lokalen chemischen Umgebung als Leitfaden basiert. Auf der Grundlage dieser Analyse zeigen wir dann, dass die MAE für Strukturen mit 62,5% Fe-Gehalt um etwa 25% im Vergleich zu einer vollständig geordneten äquiatomischen Struktur ansteigt, was frühere experimentelle Studien bestätigt. Anschließend führe ich eine detaillierte Untersuchung der Korrelation zwischen der lokalen chemischen Umgebung und den OMA-Werten durch und stelle fest, dass es unwahrscheinlich ist, damit ein detailliertes quantitatives Verständnis der MAE zu erzielen. Darüber hinaus beziehe ich die Auswirkungen starker Elektron-Elektron-Wechselwirkungen, die in eher lokalisierten d-Orbitalen in Fe und Ni vorhanden sind, auf die MAE in $L1_0$-FeNi ein, indem ich DFT$+U$-Rechnungen verwende. Diese Studie zeigt, dass Coulomb-Elektronenwechselwirkungen, die durch den Parameter U gesteuert werden, einen signifikanten Einfluss auf die magnetischen Eigenschaften haben können, insbesondere auf das MAE in der $L1_0$-FeNi-Legierung.

Im Abschlussprojekt meiner Dissertation untersuche ich die Auswirkung chemischer Unordnung auf die magnetischen Austauschwechselwirkungen und folglich die Curie-Temperatur in $L1_0$-FeNi. Ich zeige, dass die Variationen in der lokalen chemischen Umgebung einen signifikanten Einfluss auf die magnetischen Austauschwechselwirkungen haben können. Um die Auswirkung solcher Variationen in den magnetischen Austauschkopplungen zu messen, verwende ich Monte-Carlo-Simulationen und führe eine Modellstudie des Heisenberg-Modells mit Nächste-Nachbarn-Wechselwirkungen durch, die aus Gauß-Verteilungen auf einem fcc-Gitter generiert werden, und zeige, dass die Variation in der magnetis-

chen Austauschkopplung aufgrund der chemischen Unordnung zu einer starken Verringerung von T_c führen kann.

Schließlich fasse ich meine Arbeit zusammen und gebe einen Ausblick auf $L1_0$-FeNi als freien Seltenerd-Dauermagneten.

ACKNOWLEDGEMENTS

I want to thank all the people who have supported and helped me on my way to PhD during the past four years.

First, I would like to thank my supervisor, Prof. Claude Ederer, for his unmatched dedication and mentorship throughout the last four years. I am thankful to you for everything you have taught me and for always supporting me when needed.

I want to thank Prof. Nicola Spaldin for her exceptional leadership and for creating a great working environment. Thank you very much for all your valuable feedback on my presentations during the group meetings.

Special thank goes to Alexander Edström for his excellent guidance and support throughout my PhD. I also want to thank my project student Mayan Si, with whom we made some exciting scientific discoveries. Thanks a lot for your hard work. It was a pleasure working with you.

Many thanks to all former and present members of the Materials Theory group who have made my doctoral studies such an enjoyable and memorable time: Alberto, Alex H, Alex E, Andrea, Aria, Awadhesh, Bastien, Carl, Chiara, Dominik, Florian, Jaime, Kane, Marek, Max, Natalya, Peter, Quintin, Sayantika, Sophie B, Sophie W, Tara, Tobias, Xanthe, and all the former and present master students.

Special thanks go to Natalya and Dominik for guiding me at the beginning of my PhD, and for all the fun out-of-office activities including several visits to the rope parks.

I am thankful to Natalya, Tobias, Kane, and Tara for being amazing officemates. Special thanks goes to Susanne, who made my everyday life so much easier by taking care of all the administrative work.

I would further like to express my gratitude to Rebecca Janisch, Ralf Drautz, Tilmann Hickel, Matous Mrovec for giving me the opportunity to work on exciting projects during my masters at ICAMS.

I would like to thank my parents Meena, Rajendra, Sashi, and my mother- and father-in-law Babita and Bhagwandas and my brother, Yash, who have continuously supported me in my efforts.

Finally, a heartfelt thanks goes out to my wife, Palak, for her irreplaceable moral support and patience. None of this would have been possible without your support. Thank you for always being there for me.

Ask the right questions, and nature will open the doors to her secrets
– C.V. Raman

CONTENTS

LIST OF FIGURES

LIST OF ACRONYMS

DFT   Density functional theory

MAE   Magnetocrystalline anisotropy energy

OMA   Orbital moment anisotropy

DLM   Disordered local moment

FM   Ferromagnetic

LDA   Local density approximation

SOC   Spin-orbit coupling

SOAP Smooth overlap of atomic positions

t-SNE t-stochastic neighbor embdding

SC   Self-consistent

MFT   Magnetic force theorem

WF   Wannier function

MLWFs Maximally localized Wannier functions

CPA   Coherent potential approximation

LIST OF PUBLICATIONS

»Interplay between chemical order and magnetic properties in $L1_0$ FeNi (tetrataenite): A first-principles study«[1]
Ankit Izardar and Claude Ederer
Physical Review M **4**, 054418 (2020)
DOI: 10.1103/PhysRevMaterials.4.054418

»Effect of chemical disorder on the magnetic anisotropy in $L1_0$ FeNi from first principles calculations«[2]
Mayan Si, Ankit Izardar and Claude Ederer
arXiv:2111.12492 (2021)
DOI: https://doi.org/10.48550/arXiv.2111.12492

»Impact of chemical disorder on magnetic exchange interactions in $L1_0$-FeNi (tetrataenite)«[3]
Ankit Izardar and Claude Ederer
arXiv:2203.00640 (2022)
DOI: https://doi.org/10.48550/arXiv.2203.00640

»Effect of introducing $+U$ on the magneto-crystalline anisotropy energy in $L1_0$-FeNi«(*in preparation*)
Ankit Izardar and Claude Ederer

BACKGROUND AND MOTIVATION

1.1 INTRODUCTION

Magnetic materials are playing an ever-increasing role in our fight against climate change. In particular, permanent magnets, which form a crucial component in devices used in generating electric power from renewable energy sources such as wind, hydro, tidal, etc. play a pivotal role in this quest.

Magnets can be divided into two categories, namely, *hard* and *soft* magnets, depending on the ease with which they can be magnetized and demagnetized rather than on their mechanical properties. The key figure of merit of a magnet is the magnetic energy product, *(BH)*$_{max}$ which is equal to the area of the biggest rectangle (optimal product of the remanence (B_r) and the coercivity (H_r)) that can be fitted in the second quadrant of the $B(H)$ loop and provides an estimation of the energy that can be stored in a magnet (see black shaded region in Fig. 1). The magnetic properties (e.g. coercivity (H_c)) derived from the $B(H)$ hysteresis loop are extrinsic in nature, since they depend on the microstructure of the material while magnetic properties obtained from $M(H)$ hysteresis loop are intrinsic in nature (e.g. intrinsic coercivity (H_{ci})) as they depend on the crystal structure and the composition of the material.

Soft magnets generally exhibit high permeability and minimal hysteresis, i.e., their hysteresis loop is ideally narrow and, therefore, can be easily magnetized and demagnetized. They are mainly used to guide and concentrate the magnetic flux produced by electric currents in for example transformers, electric motors, and generators. Si steels, permalloy (Ni-Fe), soft iron, and permendur (Fe-Co) are few of the examples of soft magnets that are more commonly used in the electromagnetic machinery.

Hard magnets, on the other hand, are capable of providing magnetic flux in a particular volume of space without any expenditure of energy. As a result, they are used to make permanent magnets. They are characterized by their maximum energy product *(BH)*$_{max}$ and high coercivity which provides the resistance towards any external demagnetizing field. Their hysteresis curve is generally broad and square in shape for the ideal case. They find their use in a wide variety of applications, for example, electric motors, robotics, power generators, automobiles, loudspeakers, etc.

Currently, high performance permanent magnets are composed of rare-earth elements (Sm, Nd, Dy, etc.), which provide high resistance
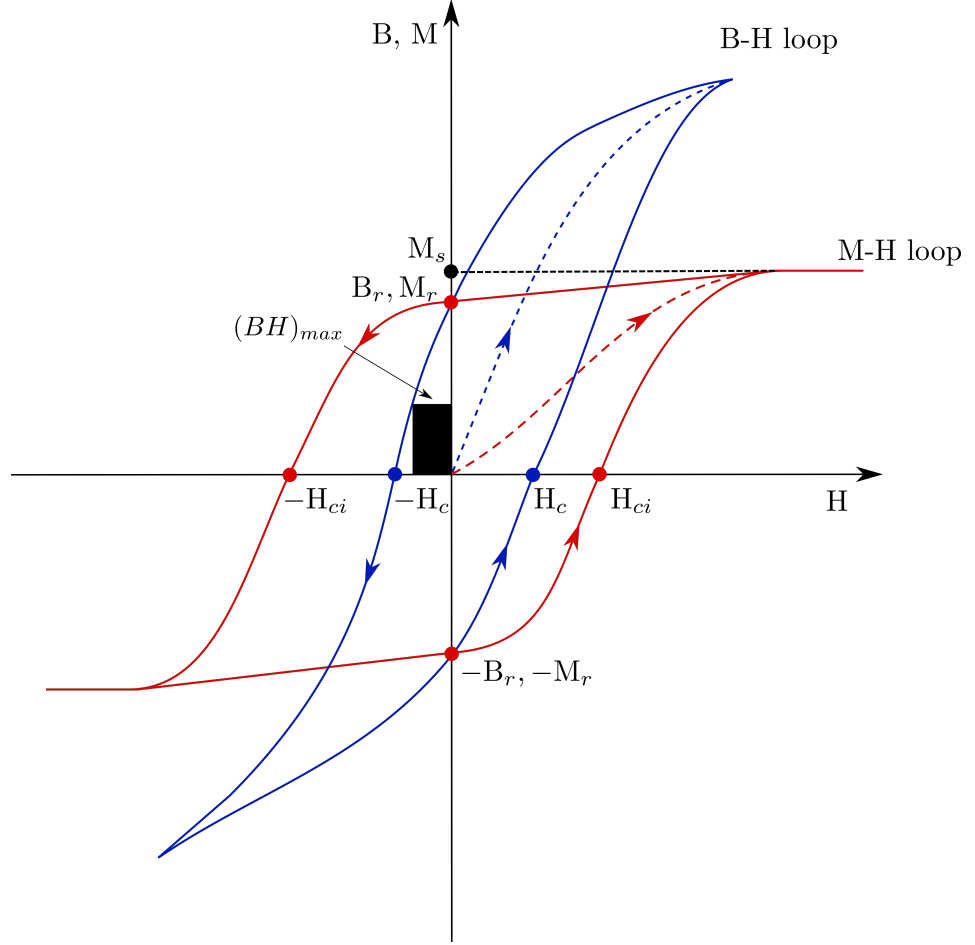
Figure 1: Typical hysteresis curve of a ferromagnetic material. B-H and M-H loops are denoted by blue and red lines, respectively. Both plots contain the same information since $\vec{B} = \mu_0(\vec{M} + \vec{H})$. They look different since $B(H)$ curve does not saturate as B continues to rise with increasing H. Dashed lines correspond to the magnetization process starting from the demagnetized state. The maximal energy product $(BH)_{\max}$ is denoted by the black shaded region and the key quantities, for example, saturation magnetization (M_s), remanent magnetization (M_r), residual magnetic induction (B_r), coercivity (H_c), and the intrinsic coercivity (H_{ci}) are denoted by different dots.

to demagnetization, and transition-metals (Fe, Co, etc.), which provide high saturation magnetization. At present, magnets containing rare-earth elements especially those belonging to the SmCo family (e.g., $SmCo_5$ and Sm_2Co_{17}) with energy products in the range of 5-20 MG Oe (40 - 160 kJ/m^3) [4–7] and the NdFeB family (e.g. $Nd_2Fe_{14}B$) with energy products in the range 5-50 MG Oe (40-400 kJ/m^3) [8–10] are in very high demand globally due to an increase in the production of wind-turbines, hybrid-electric vehicles, electric appliances, etc. [11] For instance, a hybrid motor in an electric vehicle requires around 1.3 kg of Nd-Dy-Fe-B magnets while a permanent magnet generator would require around 2918 kg of Nd-Fe-B [11].
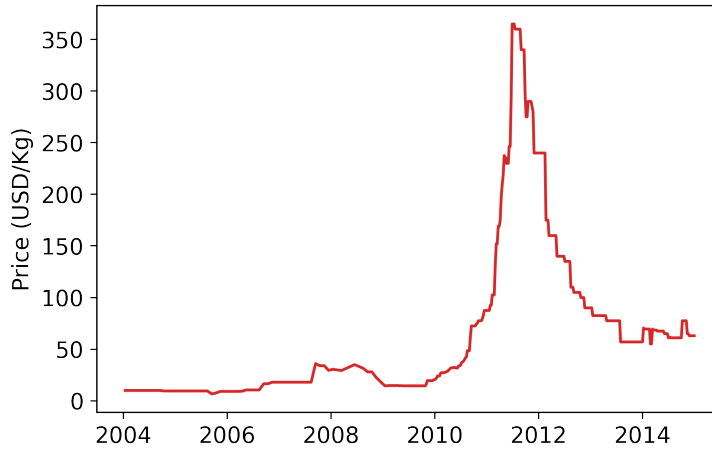
Figure 2: Annual average price of Nd in USD/kg from 2004 to 2015. Reproduced from Ref. [19].

While there is no doubt about the performance of these rare-earth based *supermagnets*, the volatility in prices [12, 13], and uncertainty in the supply of the raw materials [14, 15] required for manufacturing them, make these magnets unsustainable for future use. For instance, the price of Nd increased by around 3500% between 2010 and 2012 followed by a subsequent reduction in the price in 2014 (see Fig. 2), indicating the price volatility of this vital element [16, 17]. This price volatility and the uncertain supply is due to certain economic geopolitical constraint. The rare-earth elements are not really rare, but are scattered and are extracted mainly in China, which fulfills around 97% of global rare-earth demand. The strict control on the export of rare-earth elements by China lead to an increase in the price of rare-earth elements which consequently lead to the so-called "rare-earth-crisis" [12]. The European Commission has since then listed rare earth elements as "Critical Raw Materials" given their high economic importance and high supply risk [18].

Thus, in order to meet the global increasing demand and to find an alternative to rare-earth based magnets, new inexpensive permanent magnets containing low or zero rare-earth elements must be developed. It is important to note that developing a rare-earth free permanent magnet with the performance comparable to those of high-performing rare-earth based magnets is very challenging as removing the rare-earth elements causes a significant loss of the magneto-crystalline anisotropy, which is due to the interplay between enhanced spin-orbit coupling and strongly correlated nature of the $4f$-orbitals [20]. In this context, it is of interest to develop magnets with performance in between magnets like transition-metal-based ferrite, AlNiCo, etc., and the high performance rare-earth-based magnets such as $Nd_2Fe_{14}B$ and $SmCo_5$. Such "midrange magnets" can be used in applications where the high performance of the rare-earth-based magnets is not necessarily required but are used

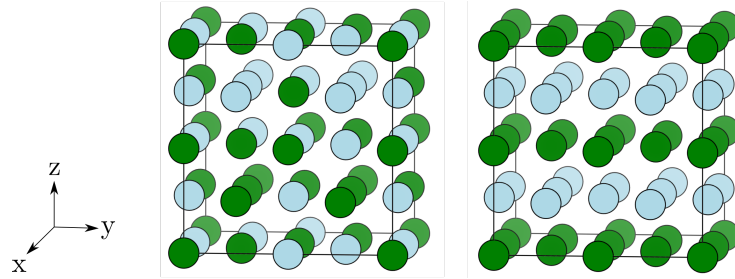Figure 3: Schematic representation of the face-centered cubic A1-type (left) and the tetragonal $L1_0$-type (right) crystal structures. Green and blue colored spheres represents two different atomic species.

anyways due to the absence of any magnet with moderate performance and, thus, leading to high costs [21].

In the rest of this chapter, I briefly discuss a few potential candidates for $L1_0$-structured rare-earth free permanent magnets. In Sec. 1.3, I introduce and discuss the properties of $L1_0$-FeNi which is the main focus of this thesis. Finally, in Sec. 1.4, I provide an overview of the structure and scope of this thesis.

1.2 $L1_0$-STRUCTURED RARE-EARTH FREE PERMANENT MAGNET CANDIDATES

When pursuing the quest to find a new material for a rare-earth free permanent magnet, the goal is to design a material with (1) a strong magneto-crystalline anisotropy energy (MAE), (2) a large saturation magnetization (M_s), and (3) a high Curie temperature (T_c). While the materials with large M_s and high T_c exists - e.g., $Fe_{0.65}Co_{0.35}$, also known as permendur, with $T_c \sim 1250\,K$ and $M_s \sim 2.5\,T$ [22], it is the MAE that represents a real challenge.

The strength of the MAE is dictated by the symmetry of the atomic environment and the magnitude of the spin–orbit coupling. The greatest potential for a large intrinsic MAE is known to be found in materials with uniaxial environments such as FeNi, FePt, CoNi, MnBi, MnAl, MnGa, etc. These compounds form in the tetragonal $L1_0$ structure[1] consisting of alternating layers of the constituent elements which are stacked parallel to the tetragonal c-axis (see Fig. 3). In contrast, a chemically disordered phase has a cubic symmetry where each site on an fcc lattice can be occupied by either of the constituent elements (see Fig. 3). A chemically ordered $L1_0$ structure forms through the disorder-order transformation from a chemically disordered fcc structure which happens by the nucleation and growth of the chemically ordered $L1_0$ regions in the chemically disordered fcc matrix.

Mn-based ferromagnetic alloys such as MnAl and Mn_2Ga are known promising candidates for the rare-earth-free permanent magnets due

---

1 structure type - AuCu I, space group - *P4/mmm*

to their high coercivity and low cost [23–31]. In particular, the magnetic properties of ferromagnetic L1$_0$ structured τ-MnAl which forms at 51-58 at.%Mn have been extensively reported [26, 32–34]. For example, recent studies of the (001) oriented MnAl thin films on the GaAs substrates have reported a saturation magnetization of 361 emu/cm^3 (361 kA/m), anisotropy constant of 13.65 Merg/cm^3 (1.365 MJ/m^3), and the magnetic energy product of about 4 MGOe (31.82 kJ/m^3) [26]. Another Mn-based candidate with good coercivity and modest magnetization is Mn$_2$Ga [31], but it suffers from high cost of Ga which makes it unfeasible as a permanent magnet unless a low-cost substitute of Ga is found.

Fe-based rare-earth-free permanent magnet candidates such as FePt, FeCo, FeNi, etc., are actively pursued due to the large saturation magnetization of Fe and its high abundance in the earth crust. FePt has attracted a lot of attention in recent years due to the high anisotropy resulting from the large spin-orbit coupling of the 5d element, Pt [35–44]. L1$_0$-FePt can be generated by annealing the face-centered-cubic FePt. Chemical synthesis routes have been widely employed for this purpose [36, 38, 39, 44]. For example, in a recent study, L1$_0$-ordered FePt nanostructures were successfully synthesized by employing a chemical approach where bismuth additives were used to achieve the enhanced ordering. Resultant maximum room temperature coercivity of 15.2 kOe (1.21 MA/m) was measured [44].

Face-centered-cubic FeCo is a soft magnetic material with a very small MAE. However, Burkert et $al.$ [45] showed by employing first-principles calculations of the tetragonal FeCo alloys that it is possible to achieve a saturation magnetization which is about 50% larger than FePt and a uniaxial MAE that is also about 50% larger than that of FePt. Experimental realization of the tetragonal FeCo magnets was reported by Andersson et $al.$ [46], who created tetragonally distorted FeCo alloys by epitaxial growth in conjucture with Pt in a superlattice. They reported the MAE reaching to about 210 μeV/atom and a saturation magnetization of 2.5 μ_B/atom at 40 K, which is in qualitative agreement with theoretical predictions. However, synthesis of the bulk L1$_0$-FeCo phase has not been successful so far.

This concludes the review of some of the important rare-earth-free permanent magnet candidates. For further reading on the progress and the future challenges in rare-earth-free permanent magnets, I suggest the interested reader to refer to the review articles by Cui et $al.$ [47], Skokov et $al.$ [48], Ronning et $al.$ [49], Shao et $al.$ [50], and Lewis et $al.$ [16].

1.3 L1$_0$-FE$_{50}$NI$_{50}$ ALLOY (TETRATAENITE)

The L1$_0$-structured Fe$_{50}$Ni$_{50}$ alloy (tetrataenite) is a promising candidate for the development of rare-earth-free permanent magnets. It was

first discovered in 1962 in laboratory by Néel *et al.* during the study of single crystal ordered by neutron bombardment under the magnetic field at a temperature below 320°C (593 K) [51]. Few years later, it was also identified in iron meteorites by Peterson *et al.* using Mössbauer spectroscopy and X-ray diffraction techniques [52–56].

The $L1_0$ structure imparts tetrataenite [2], a strong magneto-crystalline anisotropy energy (MAE), large saturation magnetization, and a high Curie temperature ($T_C > 800$ K) [57–60]. In contrast, the disordered phase of FeNi has an fcc structure (A1-type fcc) where Fe and Ni atoms occupy sites over the fcc lattice randomly and has very weak MAE due to its cubic symmetry.

Several past studies have revealed an order-disorder transition temperature ($T_{o\text{-}d}$) of $\sim 320°$ C (593 K) [51, 61, 62]. However, recent experimental studies on meteorites samples showed the onset of disordering only above $500°$ C (793 K) [57, 60]. Santos *et al.* [63] pointed out the importance of kinetics in the disordering of tetrataenite. They carried out annealing experiments at different temperatures on two different meteorite samples and measured the hysteresis properties such as coercivity and the saturation remanent magnetization for the disordering process. They showed that disordering in tetrataenite does not start immediately upon heating but is a kinetically limited process.

So far, it has not been possible to achieve a fully ordered FeNi phase in laboratories similar to that found in iron meteorites, due to its low $T_{o\text{-}d}$. Around $T_{o\text{-}d}$, diffusion coefficients of Fe and Ni are very low (one atomic jump per 10^4 years [64]), so it takes millions of years for the ordered phase to form. Therefore, it is only found in meteorites. However, in several recent experimental studies, researchers were successful in preparing samples with a high degree of chemical order. For example, Goto *et al.* [65] synthesized $L1_0$-FeNi powder with a high degree of chemical order using nitrogen insertion and topotactic extraction (NITE). They nitrided the A1-FeNi powder with ammonia gas in an electric furnace which resulted in the formation of a stable intermediate material, FeNiN, which has the same arrangement of atoms as in $L1_0$-FeNi. FeNiN was then denitrided by topotactic reaction to obtain the single-phase $L1_0$-FeNi with an order parameter [3] of 0.71 and a coercivity of 142 kA/m. In a more recent study by Nishio *et al.* [66], they reported that the island structures of $L1_0$-FeNi formed by employing sputter deposition of FeNi alloy and successive use of NITE method can result in improved coercivity (188 kA/m at 10 K).

Makino *et al.* [67] also reported the $L1_0$-FeNi phase with a chemical degree of order of about 0.8 upon crystallization of the amorphous phase of $Fe_{42}Ni_{41.3}Si_8B_4P_4Cu_{0.7}$ alloy. In their analysis, they found

---

2 The name tetrataenite is derived from its tetragonal structure and the mineral "taenite" consisting of Fe and Ni alloys.

3 Note that the degree of long-range order in this study was determined by the intensity of the superlattice deflection lines corresponding to the layering in the $L1_0$ structure.

that the formation of the ordered phase of FeNi was favoured due to (1) a high diffusion rate of the elements in the alloy at low temperature during the crystallization from an amorphous phase, (2) a large driving force of the precipitation of the ordered FeNi from the amorphous phase, and (3) the presence of clusters of the ordered phase of FeNi.

In a study by Shito *et al.* [68], they demonstrated that the L1$_0$-FeNi phase can be fabricated by using pulsed laser deposition where alternating monoatomic layers of Fe and Ni were deposited on a Cu (001) substrate by using stabilized laser ablation technique. A similar approach was also employed by Kojima *et al.* [69] where they fabricated L1$_0$-FeNi films by alternate deposition of Fe and Ni monoatomic layers on the non-ferromagnetic Au–Cu–Ni buffer layer with a flat surface by employing molecular beam epitaxy technique in an ultrahigh vacuum chamber. Moreover, they found that the uniaxial magneto-crystalline anisotropy energy (MAE) monotonically increased with the long-range order parameter of the L1$_0$ phase and the highest value of the MAE ($0.93\,\mathrm{MJ/m^{-3}}$) and the saturation magnetization ($1470\,\mathrm{kA/m}$) was achieved for Fe$_{60}$Ni$_{40}$, indicating Fe-rich stoichiometry to be favorable for enhanced MAE.

Alongside the promising experimental studies, several researchers have also investigated the magnetic properties of L1$_0$-FeNi by employing various electronic structure calculations and Monte-Carlo simulations. For example, both Dang *et al.* [70] and Lavrentiev *et al.* [71], found a strong coupling between magnetic and chemical orders in L1$_0$-FeNi by employing different models and approximations. Ref. [71] showed that the Curie temperature of the fully ordered phase is enhanced by about $550\,\mathrm{K}$ as compared to the Curie temperature of the chemically disordered phase. In a more recent study, Tian *et al.* [72] also showed by employing exact muffin-tin orbitals method based on DFT that the Curie temperature is enhanced for the chemically ordered phase ($T_c = 780\,\mathrm{K}$) relative to the Curie temperature of the chemically disordered phase ($T_c = 630\,\mathrm{K}$). Note that the differences in the Curie temperature between the chemically ordered and disordered phase reported by Lavrentiev *et al.* ($550\,\mathrm{K}$) and by Tian *et al.* ($150\,\mathrm{K}$) can be attributed to the different methods and approximations employed in their studies.

The origin of the MAE in L1$_0$-FeNi was investigated by Miura *et al.* [73], using first-principles density-functional calculations, where authors showed that the dominant contribution to the MAE in L1$_0$-FeNi comes from constituent Fe atoms. Moreover, they showed that the MAE increases by almost two times when orbital polarization energy is taken into account in the electronic structure calculations. Note that orbital polarization energy is related to Hund's second rule and is proportional to the square of the angular momentum expectation value. When added to the exchange and correlation energy, it effectively enhances the spin

orbit coupling parameter which results in improved values of orbital moments and anisotropy energies.

Edström *et al.* [74] studied using first-principles based calculations, effects of substitutional disorder on the MAE in L1$_0$-FeNi by employing the coherent potential approximation (CPA) [75, 76] method, which is based on mean-field framework where an averaged out effect due to chemical disorder is considered to treat the chemical disorder. They found that both the MAE and T_c decreases with increasing substitutional disorder. Furthermore, they found a reduction in the MAE by about 10% when Fe-content was increased by 20% in L1$_0$-FeNi which is in contrast to the experiments where a 30% increase in the MAE was observed for Fe$_{1.2}$Ni$_{0.8}$ [77].

1.4 STRUCTURE AND AIM OF THIS THESIS

In this thesis, I perform a detailed investigation of the key magnetic properties such as saturation magnetization, MAE, and the Curie temperature, taking into account the effect of chemical disorder in L1$_0$-FeNi. To accomplish this, I employ first-principles-based density functional theory calculations in combination with Monte-Carlo simulations.

Chapter 3 is devoted to the understanding of the coupling between chemical and magnetic orders in L1$_0$-FeNi. To model chemical disorder, we employ supercell approach where Fe and Ni atoms are distributed in a manner so as to mimic the real disordered alloys used in experiments. We then answer following questions:

- Is it possible to demonstrate the coupling between chemical and magnetic degrees of freedom in L1$_0$-FeNi using a supercell approach, as shown by previous studies employing mean-field type approaches to model the chemical disorder?

- How do the favorable magnetic properties, in particular, the MAE depend on the degree of chemical order in L1$_0$-FeNi?

- Is there a correlation between the MAE and the (global) orbital moment anisotropy in L1$_0$-FeNi?

In Chapter 4, we perform a detailed analysis of the impact of chemical disorder on the MAE by analyzing the distribution of the local orbital moment anisotropy for Fe and Ni atoms in partially disordered structures. This project was performed in collaboration with Mayan Si, a master student I supervised. We then answer following questions:

- How does the MAE in L1$_0$-FeNi depend on the specific local chemical environment and stoichiometry?

- Is there a correlation between the local atomic environment of an Fe atom and its local orbital moment anisotropy in L1$_0$-FeNi?

- If such a correlation exists, can we further increase the MAE by optimizing the composition and distribution of constituent elements?

In chapter 5, we employ DFT+U calculations and answer following question:

- How does the $+U$ incorporating second Hund's rule affect the magnetic properties, in particular, the MAE in L1$_0$-FeNi?

Finally, in chapter 6, we investigate the effect of chemical disorder on the magnetic exchange couplings and consequently the Curie temperature in partially chemically ordered L1$_0$-FeNi. We answer following questions:

- To what extent does the pairwise Heisenberg interaction depend on the local chemical environment in L1$_0$-FeNi and can this dependency be incorporated into a simple model for Monte Carlo simulations?

- If such a dependency exists, then to what extent does the variation in the magnetic exchange couplings will affect the Curie temperature in chemically disordered FeNi?

This thesis is structured as follows. In chapter 2, I introduce the methods such as DFT and Monte-Carlo simulations used in this thesis to perform the calculations. Furthermore, I also introduce in detail the magnetic properties relevant to this thesis and how one can obtain them using DFT calculations. This is then followed by the results in chapter 3, 4, 5, and 6 that I have obtained during my research. In each chapter, I first motivate the study related to the thesis, which is then followed by the review of the relevant literature and the project summary. This is then followed by the implications and further work, which is followed by the preprint of the research article itself.

METHODS AND THEORETICAL BACKGROUND

In this chapter, I will introduce the fundamentals of the computational methods used in this thesis which are widely employed to study the properties of magnetic materials. First, I will introduce the Density functional theory (DFT) - a quantum mechanical method to investigate the electronic properties of many-body systems. Then, I will discuss the basic concepts of DFT+U which takes into account strong electron-electron interactions between electrons in localized d or f orbitals. Furthermore, I will introduce and discuss the computation of MAE and the magnetic exchange couplings using DFT. Next, I will discuss in detail the approach I have employed in this thesis to treat the chemical disorder in L1$_0$-FeNi. This is then followed by the introduction to the smooth overlap of atomic positions method and the t-stochastic neighbor embedding, where former encodes the local chemical environment into a rotationally invariant vector and the latter is used to reduce the dimension of this vector for visualization. Finally, I will explain the Monte Carlo simulations which are used in this thesis to (a) obtain the temperature dependence of the chemical order parameter, and (b) calculate the magnetic transition temperature in the ordered and disordered phase in L1$_0$-FeNi. This chapter mainly follows the textbook of Giustino [78], Stöhr and Siegmann [79], Spaldin [80], and the review article by Himmetoglu *et al.* [81].

2.1 DENSITY FUNCTIONAL THEORY

For several decades, density functional theory has remained a powerful approach to calculate the electronic ground state properties of wide variety of materials from first principles. DFT is based on solving Schrödinger equation for many-body systems which includes interacting electrons and nuclei using certain set of reasonable physical approximations which do not take into account any empirical parameters. These set of approximations then allow one to transform many-body interacting problem into an effective single-particle problem.

All matter e.g., crystals, molecules, etc., consists of large number of interacting ions and electrons. One can describe the properties of all forms of materials by virtue of one single powerful equation: the many-body Schrödinger equation,

$$H\Psi(\mathbf{r},\ \mathbf{R}) = E\Psi(\mathbf{r},\mathbf{R}) \tag{1}$$

where $\Psi(\mathbf{r},\ \mathbf{R})$ corresponds to the many-body wavefunction which depends on the positions of all N_e electrons ($\boldsymbol{r} = \boldsymbol{r_1}, ..., \boldsymbol{r_{N_e}}$) and all N_n nu-

clei ($\boldsymbol{R} = \boldsymbol{R_1}, ..., \boldsymbol{R_{N_n}}$) in the material, the eigenvalue E corresponds to the total energy of the system in the quantum state given by the many-body wavefunction $\Psi(\mathbf{r}, \mathbf{R})$, and H is a full non-relativistic Hamiltonian given as:

$$H = T_\text{e} + T_\text{n} + V_\text{e-e} + V_\text{e-n} + V_\text{n-n}. \tag{2}$$

The first term, T_e, represents the kinetic energy of electrons and is given as:

$$T_\text{e} = \sum_{i=1}^{N_\text{e}} \frac{-\hbar^2}{2m_\text{e}} \nabla_{\mathbf{r}_i}^2, \tag{3}$$

where N_e represents the number of electrons at position $\mathbf{r}_i$ and m_e corresponds to the mass of the electron. Note that the ∇^2 is the scalar Laplace operator and the derivatives in the Laplace operators $\nabla_{\mathbf{r}_i}^2$ are taken with respect to the Cartesian coordinates of each electron.

The second term, T_n, the kinetic energy of the nuclei is given as:

$$T_\text{n} = \sum_{j=1}^{N_\text{n}} \frac{-\hbar^2}{2m_\text{j}} \nabla_{\mathbf{R}_j}^2, \tag{4}$$

where N_n represents the number of nuclei at position $\mathbf{R}_j$ and m_j is the mass of j nucleus.

The third term, V_{e-e}, is the electron-electron Coulomb repulsion given as:

$$V_\text{e-e} = \sum_{i \neq i'}^{N_\text{e}} \frac{\frac{e^2}{2}}{|\mathbf{r}_i - \mathbf{r}_{i'}|}, \tag{5}$$

where i and i' varies from 1 to N_e.

The fourth term, V_{e-n}, is the electron-nucleus Coulomb attraction given as:

$$V_\text{e-n} = \sum_{i=1}^{N_\text{e}} \sum_{j=1}^{N_\text{n}} \frac{-e^2 Z_j}{|\mathbf{r}_i - \mathbf{R}_j|}, \tag{6}$$

where Z_j is the j atomic number.

Finally, fifth term, V_{n-n}, is the nucleus-nucleus Coulomb repulsion given as:

$$V_\text{n-n} = \sum_{j \neq j'}^{N_\text{n}} \frac{\frac{e^2}{2} Z_j Z_{j'}}{|\mathbf{R}_j - \mathbf{R}_{j'}|}, \tag{7}$$

where Z_j and $Z_{j'}$ are the atomic number, and j and j' varies from 1 to N_n.

One can now solve Eq. 1 to get the ground state wavefuction $\Psi(\mathbf{r}, \mathbf{R})$ which would allow to determine all equilibrium properties of the material under investigation. However, due to extreme complexity of many-body wavefunction with $3(N_e + N_n)$ variables, it is impractical to solve

for a system with large number of electrons and nuclei. Thus, certain physical approximations were introduced in order to obtain good description of the many-body wavefunction with sufficient accuracy.

BORN-OPPENHEIMER APPROXIMATION   The first approximation known as Born-Oppenheimer or adiabatic approximation [82], states that the nuclei are heavier as compared to the electrons and thus they move "slower" relative to the electrons, especially in solids and molecules. In other words, on the time-scale of the movement of electrons, nuclei can be considered static. This approximation allows to neglect the kinetic energy of the nuclei and decouple the motion of the nuclei from that of the electrons, which makes the Coulomb repulsion between the nuclei constant, i.e. $V_{n-n} =$ constant. Thus, one can rewrite the time-independent Schrödinger equation for a collection of N_e electrons experiencing the potential created by fixed nuclei as:

$$(T_{\mathrm{e}} + V_{\text{e-e}} + V_{\text{ext}})\Psi_{\mathbf{R}}(\mathbf{r}) = E_o\Psi_{\mathbf{R}}(\mathbf{r}) \tag{8}$$

where V_{ext} is the external potential which is a sum of nucleus-nucleus Coulomb repulsion and electron-nucleus Coulomb attraction ($V_{\text{ext}} = V_{\text{e-n}} + V_{\text{n-n}}$), and nuclear coordinates in $\Psi_{\mathbf{R}}(\mathbf{r})$ appear only as an external parameter and thus, $\Psi_{\mathbf{R}}(\mathbf{r})$ is a function of only electron coordinates. Despite this simplification, solving Eq. 8 for N_e electrons is still a daunting task and requires further simplifications.

2.1.1   *Hohenberg-Kohn theorems*

In 1964, Hohenberg and Kohn [83] showed that for a system of interacting electrons present in an external potential:

1   The external potential V_{ext} can be uniquely determined by the ground-state electronic density $n(\mathbf{r})$.

2   The total energy E of any system is a functional of the electron density $n(\mathbf{r})$ and the total energy functional $E[n(\mathbf{r})]$ has a global minimum at the ground-state electron density $n_0(\mathbf{r})$.

The total energy functional is given as:

$$E[n(\mathbf{r})] = F[n(\mathbf{r})] + \int d^3r\, n(\mathbf{r})V_{ext}(\mathbf{r}) \tag{9}$$

The unknown internal-energy functional $F[n(\vec{r})]$ which only depends on the type of particles describes the kinetic and interaction energy of the system under study and is given as:

$$F[n(\mathbf{r})] = \langle \psi_{\mathrm{GS}}[n(\mathbf{r})] \,|\, T_{\mathrm{e}} + V_{e-e} \,|\, \psi_{\mathrm{GS}}[n(\mathbf{r})]\rangle \tag{10}$$

where $\psi_{\mathrm{GS}}[n(\mathbf{r})]$ is ground-state wavefunction. On substituting Eq. 10 in Eq. 9, the total energy functional can be written as

$$E[n(\mathbf{r})] = \langle \psi_{\mathrm{GS}}[n(\mathbf{r})] \, | \, T_{\mathrm{e}} + V_{e-e} \, | \, \psi_{\mathrm{GS}}[n(\mathbf{r})] \rangle$$
$$+ \int d^3 r n(\mathbf{r}) V_{ext}(\mathbf{r}) \quad (11)$$

An important observation from the above equation is that all we need is the electron density $n(\mathbf{r})$ to be able to calculate the ground state energy.

The Hohenberg and Kohn theorem neither tells us the exact functional form and nor does it tell us how to construct such functional. Therefore, additional range of physical approximations are necessary in order to obtain such functional.

2.1.2 *Kohn-Sham equations*

In 1965, Kohn and Sham [84], showed how the unknown universal functional can be approached. One can see in Eq. 11, that the second term has an explicit dependence on the electron density $n(\mathbf{r})$, while the first term (kinetic energy + Coulomb energy) has only implicit dependence on the electron density. An explicit expression for the kinetic energy is unknown for the interacting system. Kohn and Sham therefore mapped the system of interacting electrons in its real potential onto a system of non-interacting electrons with the same density. The Eq. 11 in the Kohn-Sham system can be written as

$$E_{KS}[n(\mathbf{r})] = \overbrace{\int d^3 r n(\mathbf{r}) V_{ext}(\mathbf{r})}^{\text{External potential}} - \overbrace{\sum_i \int d^3 r \phi_i^*(\mathbf{r}) \frac{\nabla_2}{2} \phi_i(\mathbf{r})}^{\text{Kinetic energy}}$$
$$+ \underbrace{\frac{1}{2} \int \int d^3 r d^3 r' \frac{n(\mathbf{r}) n(\mathbf{r'})}{|\mathbf{r} - \mathbf{r'}|}}_{\text{Hartree energy}} + \underbrace{E_{xc}(n(\mathbf{r}))}_{\text{Exchange-correlation energy}} \quad (12)$$

where $\phi_i(\mathbf{r})$ is the single electron wavefunction and the first three terms (external potential, kinetic energy, and Hartree energy) constitutes the total energy in the non-interacting system. The last term, so-called exchange-correlation energy, $E_{xc}(n(\mathbf{r}))$, is unknown and accounts for all the differences which occur as a result of mapping the interacting electron system onto a non-interacting electrons system. If $E_{xc}(n(\mathbf{r}))$ can be determined, then using the electron density, one can determine the ground state energy of the system. Furthermore, according to "Hohenberg–Kohn variational principle", ground state density $n_o(\mathbf{r})$ can be determined by minimizing the total energy $E(n(\mathbf{r}))$:

$$\frac{\delta E(n(\mathbf{r}))}{\delta n} \bigg|_{n_o(\mathbf{r})} = 0 \quad (13)$$

For wavefunctions $\phi_i(\mathbf{r})$, the Hohenberg–Kohn variational principle then leads to

$$\left(\frac{-\hbar^2}{2m}\nabla^2 + V_{\text{ext}}(\mathbf{r}) + V_{\text{H}}(\mathbf{r}) + V_{\text{xc}}(\mathbf{r})\right)\phi_i(\mathbf{r}) = \varepsilon_i\phi_i(\mathbf{r}) \qquad (14)$$

where $V_{\text{H}}(\mathbf{r})$ and $V_{\text{xc}}(\mathbf{r})$ represents the Hartree potential and the exchange-correlation potential, respectively. The Kohn-Sham potential $V_{\text{KS}}(\mathbf{r})$ is given by

$$V_{\text{KS}}(\mathbf{r}) = V_{\text{H}}(\mathbf{r}) + V_{\text{xc}}(\mathbf{r}) + V_{\text{ext}}(\mathbf{r}), \qquad (15)$$

where the exchange-correlation potential is given by

$$V_{\text{xc}}(\mathbf{r}) = \frac{\delta \text{E}_{\text{xc}}[n(\mathbf{r})]}{\delta n(\mathbf{r})}\bigg|_{n(\mathbf{r})} \qquad (16)$$

Once the effective single-particle wavefunctions ($\phi_i(\mathbf{r})$) are found, the electron density can be calculated as:

$$n(\mathbf{r}) = \sum_{i=occ} |\phi_i(\mathbf{r})|^2 \qquad (17)$$

The above set of equations are called Kohn-Sham equations and Eq. 14 forms the basis of Kohn-Sham theory. Note that this equation is a standard eigenvalue problem where one needs to determine eigenfunctions, $\phi_i(\mathbf{r})$ and eigenvalues ε_i. However, to determine them, one needs to know the total Kohn-Sham potential $V_{\text{KS}}(\mathbf{r}) = V_{\text{H}}(\mathbf{r}) + V_{\text{xc}}(\mathbf{r}) + V_{\text{ext}}(\mathbf{r})$. $V_{\text{ext}}(\mathbf{r})$ can be determined by specifying the nuclear coordinates of the materials under consideration but the main difficulty lies in determining $V_{\text{H}}(\mathbf{r})$ and $V_{\text{xc}}(\mathbf{r})$ which depends on the electron density $n(\mathbf{r})$ which in turn depends on the unknown eigenfunctions $\phi_i(\mathbf{r})$. Therefore, Kohn-Sham equations have to be solved self-consistently. Fig. 4 outlines this approach.

To calculate properties of magnetic materials, one needs to consider electron spin where electron density becomes spin-dependent. Spin-DFT calculations can be classified into two broad categories, *collinear* and *non-collinear* calculations. The collinear spin approximation is widely used to describe the basic properties of a vast variety of standard ferro-magnetic materials. To perform collinear spin-DFT calculations, one need to make approximations that spin density can be aligned along only one direction. The electron density is split into two

$$n_\uparrow(\mathbf{r}) = \sum_{i\uparrow} |\phi_{i\uparrow}(\mathbf{r})|^2, \quad n_\downarrow(\mathbf{r}) = \sum_{i\downarrow} |\phi_{i\downarrow}(\mathbf{r})|^2 \qquad (18)$$

where $n_\uparrow(\mathbf{r})$ is "spin-up" and $n_\downarrow(\mathbf{r})$ is "spin-down". The total energy functional then depends on the total electron charge density $n(\mathbf{r}) = n_\uparrow(\mathbf{r}) + n_\downarrow(\mathbf{r})$ and electron spin density which is simply given as the
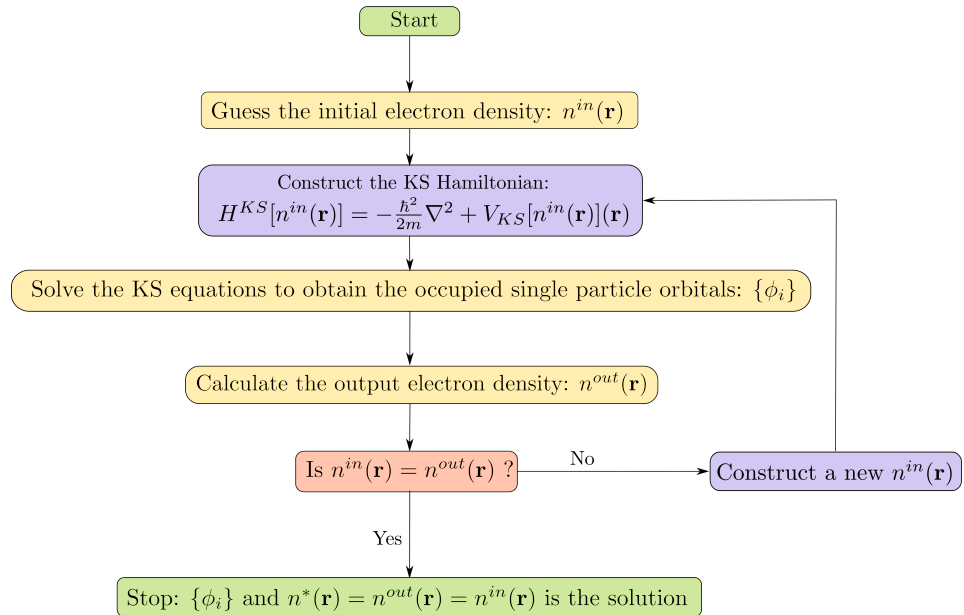
Figure 4: DFT algorithm representing the self-consistent solution to the Kohn-Sham equations.

difference in spin-up and spin-down, i.e., $m(\mathbf{r}) = n_\uparrow(\mathbf{r}) - n_\downarrow(\mathbf{r})$. On the other hand, non-collinear spin DFT calculations are necessary to study the properties of more exotic phases such as spin spirals, spin glasses, etc. A detailed overview can be found in Ref. [78].

Note that in order to solve Kohn-Sham equations, one has to make a few more approximations. For example, choice of exchange-correlation functional, the basis set to expand the Kohn-Sham orbitals, and in the case of a plane-wave basis set, one generally has to use appropriate pseudopotentials. In the following, I will now summarize various approximations for exchange-correlation energy and pseudopotentials.

2.1.3 *Approximations to the exchange-correlation functional*

Since the advent of Kohn-Sham theory, several efforts were made to construct accurate exchange-correlation functional to solve Kohn-Sham equations. In the following, I will discuss two of the most simplest and widely employed functional, namely, local density approximation (LDA) and generalized gradient approximation (GGA).

LOCAL DENSITY APPROXIMATION   Kohn and Sham first proposed the LDA in 1965 [84], where one considers the inhomogeneous electron density present in real materials as locally homogeneous. This makes it possible to calculate the exchange and correlation energy for

the regions with slow varying density. The total exchange-correlation energy within LDA is given as:

$$E_{xc}^{LDA}[n(\mathbf{r})] = \int d^3r\, n(\mathbf{r})\, \varepsilon_{xc}^{homo}[n(\mathbf{r})], \tag{19}$$

where $\varepsilon_{xc}^{homo}[n(\mathbf{r})]$ is the exchange-correlation energy density of a homogeneous electron gas and is given by

$$\varepsilon_{xc}^{homo}[n(\mathbf{r})] = \varepsilon_{x}[n(\mathbf{r})] + \varepsilon_{c}[n(\mathbf{r})] \tag{20}$$

The $\varepsilon_{x}[n(\mathbf{r})]$ is the exchange energy of the electron in the homogeneous electron gas and is known exactly [85, 86], while no simple analytical expression of the $\varepsilon_{c}[n(\mathbf{r})]$ exists. However, it is possible to calculate the correlation energy for the homogeneous electron gas by solving many-body Schrödinger equation numerically using quantum Monte Carlo simulations [87, 88]. The LDA can be easily extended for magnetic materials to local spin-density approximation (LSDA). The total exchange-correlation energy for spin-polarized system depends on the spin-up $(n_\uparrow(\mathbf{r}))$ and spin-down $(n_\downarrow(\mathbf{r}))$ electron densities and is given as:

$$E_{xc}^{LDA}[n_\uparrow(\mathbf{r}), n_\downarrow(\mathbf{r})] = \int d^3r\, n(\mathbf{r})\, \varepsilon_{xc}^{homo}[n_\uparrow(\mathbf{r}), n_\downarrow(\mathbf{r})], \tag{21}$$

where $\varepsilon_{xc}^{homo}[n_\uparrow(\mathbf{r}), n_\downarrow(\mathbf{r})]$ is the exchange-correlation energy of the homogeneous spin-polarized electron gas.

Due to its simplicity, LDA remains a useful functional and gives accurate material properties in, for example, simple metallic systems where electron density is often homogeneous. However, there are certain limitations, for example, LDA tends to predict lattice constants that are slightly smaller than the ones measured in experiments. For spin-polarized systems, LDA incorrectly predicts nonmagnetic face-centered-cubic (fcc) Fe to be lower in energy than the ferromagnetic body-centered-cubic (bcc) Fe [89].

GENERALIZED GRADIENT APPROXIMATION   To account for the inhomogeneity in the electron gas, i.e., the local variation of the electron density, another approximation known as generalized gradient approximation (GGA) was proposed [90]. Within the GGA, the gradient of the electron density is considered and the total exchange-correlation energy functional is given as:

$$E_{xc}^{LDA}[n(\mathbf{r})] = \int d^3r\, n(\mathbf{r})\, \varepsilon_{xc}^{homo}[n(\mathbf{r})] F_{xc}[n(\mathbf{r}), \nabla n(\mathbf{r}), \nabla^2 n(\mathbf{r}), ...], \tag{22}$$

where $F_{xc}[n(\mathbf{r}), \nabla n(\mathbf{r}), \nabla^2 n(\mathbf{r}), ...]$ is the enhancement factor that incorporates the changes in local electron density. Although there are many different flavors of GGA, one of the most widely used was introduced by Perdew, Burke and Ernzerhof, known as PBE [91].

Compared to LDA, GGA tends to give more accurate values of binding energies and bond lengths, but sometimes overestimates lattice constants in solids [92]. More importantly, GGA correctly predicts the ferromagnetic bcc Fe to be lower in energy than the nonmagnetic fcc Fe [89]. Throughout this work, I have employed GGA-PBE as the exchange-correlation functional in all DFT calculations.

2.1.4   *Approximations to the external potential*

In the last section, I discussed possible approximations to the exchange-correlation functional to solve Kohn-Sham equations. In this section, I discuss the remaining methodologies that are required to get a practical solution of the Kohn-Sham equations. First, I will discuss the mathematical representation of the single-particle orbitals in the Kohn-Sham equations, and then finally, the way to treat electron-nucleus interaction.

BASIS SETS   To solve Kohn-Sham equations, one need to choose a set of basis functions $\varphi_\alpha(\mathbf{r})$ to represent the Kohn-Sham orbitals:

$$\phi_{\mathrm{KS}}(\mathbf{r}) = \sum_{\alpha=1}^{N} c_{\mathrm{KS},\alpha} \varphi_\alpha(\mathbf{r}), \tag{23}$$

where $c_{\mathrm{KS},\alpha}$ are the expansion coefficients and the summation is over all basis functions in the N-dimensional basis set. For periodic systems such as solids, Bloch theorem states that the electronic wavefunctions must compose of a phase factor, $\mathrm{e}^{i(\mathbf{k})\cdot\mathbf{r}}$ and a periodic part $u(\mathbf{r}) = u(\mathbf{r} + \mathbf{R})$ where $\mathbf{R}$ is a lattice vector. For condensed phases, this introduces naturally the plane-waves with basis function:

$$\phi_{\mathrm{KS}}^{\mathbf{k}}(\mathbf{r}) = \sum_{\mathbf{G}=0}^{\infty} c_{\mathbf{k}}(\mathbf{G}) \mathrm{e}^{i(\mathbf{k}+\mathbf{G})\cdot\mathbf{r}}, \tag{24}$$

where $\mathbf{G}$ is a reciprocal lattice vector and $\mathbf{k}$ is a wave vector. Theoretically, the sum contains infinite number of $\mathbf{G}$ to represent the wavefunctions. But in practice, the fourier coefficients $c_{\mathbf{k}}(\mathbf{G})$ of the wavefunctions decreases with increasing lattice vectors $|\mathbf{k} + \mathbf{G}|$ so that the sum is truncated at a finite number of $\mathbf{G}$. This results in plane waves that are lower in kinetic energy than a certain cut-off energy E_{cut}:

$$\frac{-\hbar^2}{2m_{\mathrm{e}}}|\mathbf{k} + \mathbf{G}|^2 < E_{\mathrm{cut}}. \tag{25}$$

Note that the truncation to finite number of $\mathbf{G}$ leads to an error in the computed electronic property which can be controlled by increasing the cut-off which in turn can lead to higher computational cost. Therefore, the choice of E_{cut} should be such that the required accuracy should be reached within a reasonable computational effort.

PSEUDOPOTENTIALS   The nucleus of an atom interacts with its electrons by a Coulomb interaction given by Eq. 6. The electrons tightly bound to the nuclei, called *core electrons*, do not participate in chemical bonding and account for the largest part of the total energy due to their high binding energies. On the other hand, the *valence electrons* participate in the chemical bonding and are more delocalized. There is another class of electrons called, *semi-core electrons*, which are close in energy to the valence states and feel the presence of the chemical environment. However, they do not participate in the bonding process. One requires huge number of plane waves basis set to describe the electrons in the core region and thus leading to calculations that are computationally very demanding. To avoid high computational cost, pseudopotential method are often employed, where core electrons and the nucleus are treated as an effective nucleus, or *ionic core.* As a result, the real potential felt by the valence electrons due to the core electrons and the nucleus is replaced by an effective core potential. This leads to a small number of electrons that are treated explicitly and reduce the number of basis set. As a result, computational cost is effectively reduced. In this thesis, I have employed projector augmented wave (PAW) pseudopotential introduced by Blöchl [93] as implemented in the DFT code "Vienna Ab initio Simulation Package (VASP)" [94, 95].

DFT has remained a powerful method to describe the properties of matter. It is important to note that DFT is a ground state formalism describing the properties of materials at $0\,\mathrm{K}$ and, therefore, is not used in its basic form for calculating the properties of excited states.

2.2   DFT+U

In some cases, DFT fails to capture the ground state properties of systems where the electron-electron interactions in rather localized d or f valence states play a major role. Few examples of such systems include transition metals and rare-earth metal ions with partially filled d or f shells. This failure of DFT to describe the physics of correlated systems can be attributed to the approximate exchange-correlation functionals that tend to over-delocalize the valence electrons. This excessive delocalization of the electrons is due to the fact that the exchange and correlation interactions in the exchange-correlation functional fails to cancel out the electronic self-interactions. To incorporate the strong electron interactions within the localized valence states, several methods were proposed [96–102].

One of the simplest approach is the so-called LDA+U method[1] [99–102]. In this method, the strongly correlated electronic states are described using the Hubbard-like hamiltonian [103–106]. It consists of two

---

1 $+U$ correction when applied to the LDA functional is called as LDA+U. In this thesis, I apply $+U$ correction to the PBE functional and simply refer to it as DFT+U.

terms, a kinetic term taking into account the "hopping" of the electrons from one atomic site to its neighbors, and the potential term that considers the Coulomb repulsion between electrons that are present on the same atom. The total energy within the LDA+U formalism can be written as:

$$E_{\text{LDA}+U} = E_{\text{LDA}} + E_{\text{Hub}} - E_{\text{dc}} \tag{26}$$

where E_{LDA} represents the total energy functional being corrected in the DFT and E_{Hub} contains the interaction part of the Hubbard Hamiltonian. The E_{dc} is the double-counting term that needs to be subtracted from the DFT energy functional E_{LDA} as it is already contained in the E_{Hub}. Since, E_{dc} functional is not uniquely defined, there are different formulations of E_{dc} that have been implemented and used in different conditions. Two most popular formulations of E_{dc} used in the implementation of DFT+U are the so-called "around-mean-field" (AMF) [99, 107–109], and "fully localized limit" (FLL) [100, 102, 110, 111]. As the name implies, AMF is suited for materials with delocalized electrons (such as metals) while the FLL is more applicable for materials with well localized electrons. For an extended overview on both approaches, interested reader can refer to Ref. [109]. In this thesis, I employ a rotationaly invariant formulation of DFT+U introduced by Liechtenstein *et al.* [101]. Within this formulation, the screened on-site electron-electron interactions (U), and exchange interactions (J), can be calculated by taking atomic averages of the corresponding Coulomb integrals over the localized states.

In practice, $+U$ terms lead to the occupation dependent potential shifts on the d or f orbitals, which, in certain cases, allows the opening of a gap between the spin up and spin down channels of the corresponding orbitals and, thus, effectively leads to the delocalization of the over-localized electrons in the exchange-correlation functionals. Note that the value of U is difficult to know *a priori*. Therefore, in practice, U is tuned in a semiempirical way so as to seek agreement with the available experimental measurement of certain material property.

In this thesis, I employ DFT+U method to incorporate the atomic-like interactions which introduces the second Hund's rule and, thus, increases the orbital magnetic moments, which is known to affect the MAE [112, 113].

2.3 MAGNETO-CRYSTALLINE ANISOTROPY ENERGY

The magnetization curves generally look different when the magnetic field is applied to a magnetic material in different crystallographic directions. For some directions, it is easier to reach the saturation magnetization upon the application of the magnetic field, while for other directions, it is hard to saturate a magnet (e.g., see Fig. 5.27 of Ref. [114]). Depending on the magnitude of the applied magnetic field necessary to

reach the saturation magnetization in a magnetic material, the corresponding axes can be defined as easy or hard. For example, in the the single crystal of body-centered cubic Fe, the easy axes are the edges of the cube i.e., $\langle 100 \rangle$ directions, while diagonals of the cube i.e., $\langle 111 \rangle$ directions are hard axes. For face-centered cubic nickel, the situation is just the opposite. Nevertheless, the final value of the saturation magnetization is same regardless of the direction in which the magnetic field is applied. It's the magnitude of the magnetic field that vary along different directions to reach the saturation magnetization. The origin of this anisotropy can either be intrinsic which can be a result of the symmetry of the crystal structure or the crystal's shape or it can be extrinsic induced by using some processing techniques. In this work, I will limit the discussion to the intrinsic anisotropy known as magneto-crystalline anisotropy which can be defined as "the tendency of the magnetization to align itself along a preferred crystallographic direction" [80]. One can also define the magneto-crystalline anisotropy energy (MAE), which is the energy required to rotate the magnetization of a material from the easy to the hard axis. A high MAE is one of the critical requirements for a permanent magnet. If a strong MAE is present, a large magnetic field need to be applied to overcome the anisotropy and reverse the magnetization. This results in a large coercive field.

Magneto-crystalline anisotropy follows the symmetry of the crystal structure. For tetragonal systems, energy as a function of the magnetization direction can be written as:

$$E = K_1 \sin^2\theta + K_2 \sin^4\theta + ... \tag{27}$$

where K_1, K_2, etc. are known as the anisotropy constants and θ is the angle between the magnetization vector and the tetragonal axis. In experiments, quantity that is typically reported is the MAE constant, which is the sum of anisotropy constants. For uniaxial systems, MAE is given as:

$$\text{MAE} = E_{M\perp c} - E_{M||c} \tag{28}$$

where $E_{M\perp c}$ and $E_{M||c}$ are the total energies with the magnetization direction perpendicular and parallel to the c-axis, respectively.

As shown by Van Vleck [115], the origin of the magneto-crystalline anisotropy is related to the presence of spin-orbit coupling (SOC) in the magnetic materials. SOC is the coupling of the atomic spin to the orbital momentum. Therefore, an attempt to change the direction of the electron spin upon the application of the magnetic field also results in the reorientation of the orbital magnetic moment which itself is strongly coupled to the lattice. For rare-earth materials, the SOC is strong since the magnitude of the SOC depends on the charge on the nucleus which

itself depends on the atomic number. Hence, rare-earth elements are often used in permanent magnets where a large MAE is required.

In 1989, Bruno [116] showed that under certain assumptions, the MAE can be directly related to the anisotropy in the orbital magnetic moments in such a way that:

$$\text{MAE} = \frac{\zeta}{4\mu_B}(m_o^{easy} - m_o^{hard}) > 0 \qquad (29)$$

where ζ is the spin-orbit coupling parameter and m_o^{easy} and m_o^{hard} are the orbital magnetic moments when the magnetization direction lies along easy and hard directions, respectively. The difference $m_o^{easy} - m_o^{hard}$ is known as the orbital moment anisotropy (OMA) which represents the change in the magnitude of the orbital magnetic moments when the magnetization vector is rotated from the hard axis to easy axis or vice-versa. Eq. 29 also predicts that the orbital magnetic moments are larger along the easy axis than the hard axis. Note that this may not be valid under certain circumstances. For example, Andersson *et al.* [117] studied both the spin and the orbital magnetic moments of Au/Co/Au trilayers grown on a W(110) single crystal substrate by means of x-ray magnetic circular dichroism and found that the orbital magnetic moment of Co is not maximum along the easy axis. They showed that this is due to the presence of large spin-orbit coupling at the Au sites, and when off-site spin orbit coupling for example at the Co/Au interface becomes important, then the relationship between OMA and the MAE is no longer valid.

CALCULATION OF MAE   Since MAE is an energy difference between two different magnetization directions, i.e., easy and hard axis, it can be calculated by performing total energy calculations where the difference in the total energy is taken for two different magnetization directions with SOC included. However, it is difficult to determine the easy and the hard axis in materials when there are almost infinite possible directions. Fortunately, for uniaxial crystals, it is well known that the easy axis lies along the tetragonal *z*-axis while the hard axis is along the *xy*-plane. Once the magnetization directions are determined, the MAE can be calculated by employing first-principles based DFT calculations. Note that total energy needs to be calculated with extremely high accuracy to obtain the MAE using DFT since it is a very small energy difference between two large quantities. For example, in FeNi alloys which is the main topic of this thesis, the MAE is of the order of μeV/f.u. Highly accurate value of the MAE is achieved by using a very dense **k**-point sampling which is used in the integration over the Brillouin zone in reciprocal space, making the calculations computationally very expensive. Due to the huge computational challenge involved in the calculation of the MAE using a self-consistent (SC) calculations

with SOC included, MAE is often calculated by using approximation methods. One such method employed in this thesis is based on the so-called magnetic force theorem (MFT) [118, 119]. Within the MFT, first a self-consistent spin-polarized calculation is performed, without including the spin-orbital coupling to obtain the ground state charge density. In the next step, a non-self consistent calculation, i.e. without updating the charge density is performed for each magnetization direction with spin-orbit coupling included as a perturbation and using the ground state charge density obtained in the previous step. The MAE then can be calculated as:

$$\text{MAE} = E_{tot}^{\hat{\mathbf{n}}_1} - E_{tot}^{\hat{\mathbf{n}}_2} \simeq E(\hat{\mathbf{n}}_1) - E(\hat{\mathbf{n}}_2) \tag{30}$$

where $E_{tot}^{\hat{\mathbf{n}}_1}$ and $E_{tot}^{\hat{\mathbf{n}}_1}$ are the total energies along $\hat{\mathbf{n}}_1$ and $\hat{\mathbf{n}}_1$ direction, respectively and $E(\hat{\mathbf{n}}_1)$ and $E(\hat{\mathbf{n}}_2)$ represents energies that are sum over the occupied single particle Kohn-Sham energy eigenvalues for two different magnetization directions calculated with SOC and non-self consistent charge density. From Eq. 30, one can see that the calculation of the MAE within the MFT is based on the approximation that the change in the single-particle eigenvalue sums for two different magnetization directions is equivalent to the change in the total energy. MFT provides a good approximation to the MAE value for a given material if the variation in the charge and spin-density caused by the spin-orbit coupling vanish to first order in the SOC strength.

Daalderop *et al.* [119] employed the MFT in 1990 to calculate the MAE of the transition metals Co, Fe, and Ni within the framework of local-spin-density approximation (LSDA). They found that the magnitude of the MAE strongly depends on the electronic structure of the materials under consideration, in particular, on the shape of the Fermi surface, where even a small change in the Fermi energy can make a substantial contribution. Although their calculations did not predict the correct easy axis in Co and Ni at that time, later total energy calculations by Trygg *et al.* [120] based on the LDA functional in combination with an orbital polarization correction correctly predicted the easy axis for Co but wrong easy axis for fcc Ni. For the latter case, they concluded that this failure is due to the limitation of the LDA since in their calculations, the number of approximations were reduced to a minimum. Nevertheless, the validity of MFT has been extensively investigated by several researchers [121, 122] and it was shown that the MFT remains a very useful approximation and, therefore, is widely employed to calculate the MAE for magnetic materials containing $3d$ transition elements.

Since SC calculations to obtain the MAE are computationally very demanding, I have employed MFT throughout my thesis (except for the $+U$ calculations) to calculate the MAE in ordered and chemically disordered FeNi alloy.

2.4 MAGNETIC EXCHANGE INTERACTIONS AND HEISENBERG HAMILTONIAN

Often, magnetic properties of materials can be well described by the interaction between the localized atomic magnetic moments. This *exchange interaction* can give rise to parallel i.e., ferromagnetic, and antiparallel i.e., anti-ferromagnetism, spin alignment. The exchange interactions arises due to the Coulomb interaction between the electrons and the requirement of a total antisymmetric electronic wavefunction where the latter expresses the Pauli exclusion principle which states that the two electrons cannot enter into the same quantum state. Heisenberg in 1928 explained the origin of ferromagnetism by addressing the microscopic origin of exchanges in solids and formulated a model popularly known as *Heisenberg Hamiltonian* [123].

$$H_{Heisenberg} = -\frac{1}{2} \sum_{i \neq j} J_{ij} \mathbf{S}_i . \mathbf{S}_j \tag{31}$$

where S_i and S_j are the localized atomic magnetic moments on site i and site j, respectively and J_{ij} are the exchange coupling parameter between these spins. Note that Eq. 31 represents the classical Heisenberg model where the localized atomic magnetic moments are assumed to have fixed length and the vector variables entering in the equation are unit vectors i.e., they only describes the direction of the atomic magnetic moments. In this thesis, we have taken a convention so that J_{ij} is positive for a ferromagnetic coupling and negative for an antiferromagnetic coupling. For a magnetic system which can be described by the *Heisenberg Hamiltonian*, one can use exchange coupling parameters as an input into the Monte Carlo simulations to calculate the magnetic ordering and the Curie temperature (see Sec. 2.8.1).

COMPUTING MAGNETIC EXCHANGE INTERACTIONS   Magnetic exchange couplings, J_{ij}, can be calculated by calculating the total energy differences of different magnetic configurations using DFT, where one flips either spin i or j or even both i and j, relative to a chosen reference magnetic configuration [124]. The exchange couplings are then obtained from

$$J_{ij} = \frac{E_{\uparrow\downarrow} + E_{\downarrow\uparrow} - E_{\uparrow\uparrow} - E_{\downarrow\downarrow}}{4n}, \tag{32}$$

where arrows indicate spin direction on site i and site j in the corresponding configuration relative to the other spin which are fixed on the reference configuration, E is the corresponding total energy, and n represents the number of equivalent bonds between sites i and j within the supercell. This approach works well with large supercells as using a sufficiently large supercells avoids the interaction of spin i with a

periodic image of spin j but also makes the calculation computationally challenging. Note that this method is only applicable to very good Heisenberg systems and is valid for arbitrary angles between the atomic magnetic moments.

For itinerant metallic magnets, the Heisenberg model is not necessarily a good approximation [125]. Thus, to calculate magnetic exchange couplings in FeNi, we use another approach, where energy variations with respect to infinitesimal rotations of the spins are considered [126]. This method can also be used for materials where the Heisenberg model applies only to small variations around the ground state. The magnetic exchange couplings within this method are given as:

$$
J_{ij} = \frac{1}{2\pi} \text{Im} \int_{-\infty}^{\varepsilon_\text{F}} \text{d}\varepsilon \sum_{mm'm''m'''} \Delta_i^{mm'} G_{ij,\downarrow}^{m'm''}(\varepsilon) \Delta_j^{m''m'''} G_{ji,\uparrow}^{m'''m}(\varepsilon) \quad (33)
$$

where, $G_{ji,\uparrow}^{m'''m}$ and $G_{ij,\downarrow}^{m'm''}$ are the spin-up and spin-down intersite Green's function, respectively and the local exchange splitting is given by $\Delta_i^{mm'}$ for site i and $\Delta_j^{m''m'''}$ for site j where m, m', m'', and m''' represents different orbital character. The local exchange splitting on site i and j can be expressed as:

$$
\Delta_i^{mm'} = H_{ii,\uparrow}^{mm'} - H_{ii,\downarrow}^{mm'}, \quad (34)
$$
$$
\Delta_j^{mm'} = H_{jj,\uparrow}^{mm'} - H_{jj,\downarrow}^{mm'} \quad (35)
$$

where H represents the Hamiltonian in the tight-binding-like basis. The quantities in Eq. 33 can be obtained using DFT calculations and requires a formulation in terms of a localized tight-binding-like basis set. This can be acheived by transforming the corresponding Kohn-Sham Hamiltonian into Wannier functions [127–130] (see Sec. 2.5). Next, the Green's function matrix in the reciprocal space ($G_\sigma(\varepsilon, \mathbf{k})$) can be obtained by Fourier transforming the Kohn-Sham Hamiltonian ($H_\sigma(\mathbf{R})$) in the Wannier basis and is given as:

$$
G_\sigma(\varepsilon, \mathbf{k}) = [\varepsilon - H_\sigma(\mathbf{k})]^{-1}, \quad (36)
$$

where $H_\sigma(\mathbf{k})$ is the reciprocal-space Hamiltonian matrix. Note that the Kohn-Sham Hamiltonian $H_\sigma(\mathbf{R})$ is diagonal in the spin subspace since spin-orbit coupling is not taken into account and only collinear reference configurations are considered.

Finally, the real-space Green's function is obtained by integrating over the Brillouin zone using the following expression:

$$
G_{ij,\sigma}^{mm'}(\varepsilon, \mathbf{R}) = \int_{\mathbf{BZ}} G_{ij,\sigma}^{mm'}(\varepsilon, \mathbf{k}) e^{i\mathbf{k}.\mathbf{R}} d\mathbf{k}, \quad (37)
$$

where $\mathbf{R}$ is the lattice vector that connects two unit cells in the real space where the corresponding Wannier functions are located.

Note that Eq. 33 allows one to decompose magnetic exchange interactions into different orbital contributions if the exchange-splitting matrix $\Delta_{i,j}$ is diagonal. The magnetic exchange coupling between the orbital m on site i and orbital m' on site j can be calculated as [128]:

$$J_{ij}^{mm'} = \pm \frac{1}{2\pi} Im \int_{-\infty}^{\varepsilon_F} d\varepsilon \Delta_i^{mm} G_{ij,\downarrow}^{mm'} \Delta_j^{m'm'} G_{ji,\uparrow}^{m'm}. \tag{38}$$

To obtain the total orbital resolved magnetic exchange coupling between site i and j, one can then sum over all the orbital contributions between m and m'. The code used to calculate the magnetic exchange couplings in $L1_0$-FeNi using the method described above is available on Materials Theory Github [131].

2.5 WANNIER FUNCTIONS

The electronic ground state of a system with periodic potential within the independent-particle approximation can be determined by specifying one-particle orbitals and their occupation. These one-particle orbitals are the Bloch waves $\psi_{n\mathbf{k}}(\vec{r})$ where, according to Bloch's theorem, $\mathbf{k}$ is the crystal momentum lying inside the Brillouin zone (BZ) and n is the band index.

The Bloch orbitals $\psi_{n\mathbf{k}}(\vec{r})$ in a perfect periodic solid is given by

$$\psi_{n\mathbf{k}}(\vec{r}) = u_{n\mathbf{k}}(\vec{r})e^{i\mathbf{k}.\vec{r}} \tag{39}$$

where $u_{n\mathbf{k}}$ has the same periodicity as the solid. However, Bloch functions are delocalized in real space and, therefore, cannot be used as a basis in Eq. 33 to obtain the magnetic exchange couplings. One requires an atom-centered basis set that contains localized set of orbitals for this purpose. Wannier functions which are obtained by performing Fourier transformation of the original Bloch states fulfills this condition. In the following, I introduce Wannier functions that are used as a basis in Eq. 33 to obtain the magnetic exchange couplings for ordered and disordered FeNi alloys in Paper [3].

For a disentangled set of N Bloch orbitals $\psi_{n\mathbf{k}}(\vec{r})$, a set of N Wannier functions can be constructed as

$$|w_{n\mathbf{R}}\rangle = \frac{V}{(2\pi)^3} \int_{BZ} \left[\sum_{m=1}^{N} U_{mn}^{(\mathbf{k})} |\psi_{m\mathbf{k}}\rangle \right] e^{-i\mathbf{k}.\mathbf{R}} d\mathbf{k}, \tag{40}$$

where V is the volume of real-space primitive cell, $\mathbf{R}$ is the real-space lattice vector, and $U_{mn}^{(\mathbf{k})}$ is an arbitrary unitary matrix of dimension N that mixes the bands at wave-vector $\mathbf{k}$. The integration is done over

the BZ. Note that different $U_{mn}^{(\mathbf{k})}$ results in different Wannier functions with different spatial spreads, shape, centre, etc., and therefore, WFs are not uniquely defined.

One can obtain the maximally localized Wannier Functions (ML-WFs) [132] by determining the $U_{mn}^{(\mathbf{k})}$ in such a way so as to minimize the quadratic spread of the resulting Wannier functions in real space. Marzari and Vanderbilt [132] introduced a technique where $U_{mn}^{(\mathbf{k})}$ can be obtained by minimizing the quadratic spread

$$\Omega[U_{mn}^{(\mathbf{k})}] = \sum_n [\langle r^2 \rangle_n - \bar{\mathbf{r}}_n^2], \tag{41}$$

measuring the sum of the quadratic spreads of the WFs in real space. Once Ω is expressed in terms of the Bloch functions, one can obtain the MLWFs by minimizing Ω with respect to the $U_{mn}^{(\mathbf{k})}$ in Eq. 40. Note that while the maximum localization is one of the possible and widely employed approach to uniquely define WFs for a system under investigation, one can also describe the WFs via specific orbital projections method.

Within the projection approach, WFs are generated by projecting a set of N trial basis functions $g_n(\mathbf{R})$ centered at the site $\mathbf{R}$, which corresponds to some rough guess for the WFs, onto a chosen subset of Bloch bands at wave vector $\mathbf{k}$ to obtain

$$|\phi_{n\mathbf{k}}\rangle = \sum_{m=1}^{N} |\psi_{m\mathbf{k}}\rangle \langle \psi_{m\mathbf{k}}|g_n(\mathbf{R})\rangle. \tag{42}$$

Note that since the projection of $g_n(\mathbf{R})$ is performed for a subset of bands, the $|\phi_{n\mathbf{k}}\rangle$ do not form an orthonormal basis set. Orthonormalized Bloch-like states can be constructed by computing the overlap matrix $(S_{\mathbf{k}})_{mn} = \langle \phi_{m\mathbf{k}}|\phi_{n\mathbf{k}}\rangle_V$ (where V denotes an integral over one cell) and are given as:

$$|\tilde{\psi}_{n\mathbf{k}}\rangle = \sum_{m=1}^{N} |\phi_{m\mathbf{k}}\rangle (S_{\mathbf{k}}^{-1/2})_{mn}. \tag{43}$$

One can now perform the Fourier transformation of $|\tilde{\psi}_{n\mathbf{k}}\rangle$ to obtain a set of well-localized Wannier functions.

For a more profound overview of the Wannier functions, I suggest the interested reader to refer to Ref. [132, 133].

2.6 TREATMENT OF CHEMICAL DISORDER

To describe chemically disordered and partially ordered FeNi, we employ supercell approach with different arrangements of Fe and Ni

atoms over the available sites in an fcc lattice. Then, to quantify the degree of chemical order, we define a long-range order parameter, which I describe in the following.
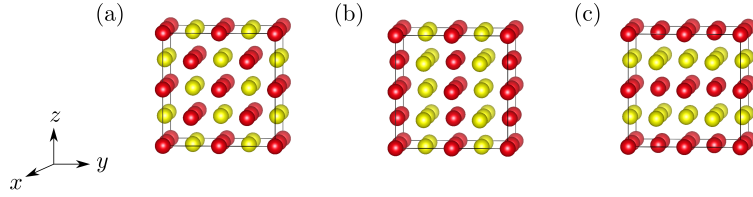

Figure 5: Three variants of $L1_0$ ordered FeNi with Fe (red spheres) and Ni (yellow spheres) arranged in alternating planes perpendicular to (a) [100], (b) [010], and (c) [001].

In the $L1_0$ structure of FeNi alloy, the tetragonal axis can lie along any of the original cubic $\langle 100 \rangle$ axes (see Fig. 5) and, therefore, we define three long range order parameters P_x, P_y and P_z in x, y and z directions, respectively. We consider a face centered cubic unit cell with four sublattice sites α, β, γ and δ as shown in Fig. 6.
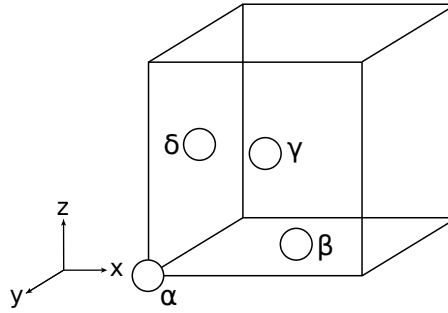

Figure 6: Conventional fcc cell with four sublattices α, β, γ, and δ.

A fully ordered $L1_0$ structure can be achieved in three ways, (i) when α and β sites are occupied by one type of atomic species and γ and δ by the other type, (ii) when α and γ sites occupied by one type of atomic species and β and δ by the other type, and (iii) when α and δ sites occupied by one type of atomic species and γ and β by the other type. Keeping this in mind, we define a probability that a site on a particular sublattice i is occupied by Fe atom as

$$p_i^{Fe} = \frac{N_i^{Fe}}{N_i} \tag{44}$$

where, N_i^{Fe} and N_i are the number of sites on sublattice i occupied by Fe atoms and the total number of sites on sublattice i, respectively. Using Eq. 44, one can define a generalized long range order parameter for arbitrary compositions P_z as

$$P_z = \tfrac{1}{2}\left(p_\alpha + p_\beta - p_\gamma - p_\delta\right) \tag{45}$$

For a completely ordered FeNi alloy as shown in Fig. 5(c), all the sites on the α and β sublattices will be occupied by Fe atoms ($p_\alpha^{Fe} = p_\beta^{Fe} = 1$) while the sites on the γ and δ sublattices will be occupied by Ni atoms ($p_\gamma^{Fe} = p_\delta^{Fe} = 0$) resulting in $P_z = 1$. On the other hand, in a completely disordered FeNi alloy, the probability that a site on a particular sublattice i is occupied by Fe atom are all equal i.e., $p_\alpha^{Fe} = p_\beta^{Fe} = p_\gamma^{Fe} = p_\delta^{Fe}$, resulting in $P_z = 0$. One can also define long range order parameters along x and y directions in a similar way and are given as:

$$P_x = \tfrac{1}{2}\left(p_\alpha - p_\beta + p_\gamma - p_\delta\right), \tag{46}$$

$$P_y = \tfrac{1}{2}\left(p_\alpha - p_\beta - p_\gamma + p_\delta\right), \tag{47}$$

The long range order parameters defined above reduces to the order parameters defined in Paper [1] for equiatomic stoichiometry (50% Fe and 50% Ni), where $\sum_i p_i = 2$. Note that any deviation from the equiatomic stoichiometry will automatically lead to a reduction in the order parameter.

The total bond energy (considering only nearest neighbour interactions) for our system can be written as:

$$E = N_{\mathrm{FeFe}}U_{\mathrm{FeFe}} + N_{\mathrm{FeNi}}U_{\mathrm{FeNi}} + N_{\mathrm{NiNi}}U_{\mathrm{NiNi}} \tag{48}$$

where, N_{ij} is the number of nearest-neighbour bonds between atoms of type i and j, and U_{ij} is the energy of an ij bond. By writing N_{ij}'s in terms of long range order parameters (analogous to that shown in [134] for a bcc structure), the Eq. 48 can be written as

$$E = E_0 - N\Delta E P^2 \tag{49}$$

where, E_0 and ΔE are functions of U_{FeFe}, U_{FeNi} and U_{NiNi}, N is the number of conventional unit cells in the system and $P^2 = P_x^2 + P_y^2 + P_z^2$ is the long range order parameter of the system. It is to be noted that Eq. 48 has been defined for a very simple model, where only nearest neighbour interactions are considered.

Finally, for fixed stoichiometry, Eqs. (45)-(47) can be inverted and the probabilities p_i^{Fe} are defined by specifying the long range order parameter P_x, P_y, and P_z within the allowed range. One can then generate configurations corresponding to a specified value of long range order parameter. In this thesis, I generate configurations with equiatomic

stoichiometry corresponding to the $2 \times 2 \times 2$ supercell of the conventional cubic fcc cell where for each configuration 16 Fe and 16 Ni atoms are randomly distributed over the 32 available sites, according to the probability defined in Eq. 44 corresponding to a fixed value of P_z with $P_x = P_y = 0$. Configurations with Fe-rich stoichiometries are generated by randomly replacing Ni atoms in the structures with equiatomic stoichiometry.

The python code used to generate configurations for a given value of P_z is publicly available on Materials Theory Github [135].

2.7   REPRESENTING LOCAL CHEMICAL ENVIRONMENTS

In Paper [2], to investigate the correlation between the local chemical environment and the orbital moment anisotropy, we employ smooth overlap of atomic positions (SOAP) [136] method to characterize the local atomic environment around an atom.

Within the SOAP approach, the atomic neighborhood of an atom is represented, inside a cutoff sphere $A_i(r_{cut})$, by an atomic density field centered on the atom i and is given by

$$\rho_i(\mathbf{r}) = \sum_{j \epsilon A_i(r_{cut})} \exp\left(-\frac{|\mathbf{r} - \mathbf{r}_j|^2}{2\sigma^2}\right), \tag{50}$$

where the atomic density is represented by using 3D Gaussians centered on each neighboring atom and the sum is taken over all the density of atoms j within the cutoff sphere. The neighbour density around each atom is then expanded using a combination of radial basis and spherical harmonics. The products of the expansion coefficients then results in the rotationally invariant descriptor in the form of a SOAP vector.

Since the SOAP approach typically results in a high-dimensional vector, one needs to reduce the high-dimensional SOAP vector to 2- or 3-dimensions for visualization and analysis. While a large number of dimensionality reduction methods exist [137–144], in Paper [2], we employ t-stochastic neighbour embedding (t-SNE) [145] as implemented in scikit-learn [146]. The underlying idea behind the t-SNE is to map high-dimensional data points to low dimensions in such a way so as to preserve the pairwise distances as much as possible. This way, t-SNE not only captures the local structure of the high-dimensional data points but also preserves the global structure of the data set e.g., the presence of clusters. Note that the cluster of data points i.e., a cluster of SOAP vectors that are all close to each other, will represent similar chemical environments. The algorithm first calculates the Euclidean distances between the data points in high-dimension and then converts these distances into joint probabilities which represents the similarities. The similarity of datapoint y to datapoint x is given by the conditional probability

$$p_{y|x} = \frac{G_{xy}}{\sum_{k \neq i} G_{xk}}, \tag{51}$$

where G_{xy} is a Gaussian kernel centered on datapoint x. Note that $p_{y|x}$ will be relatively high for points nearby to x while it will be very small for widely separated datapoints. Next, a similar joint probability distribution is constructed in the low dimension by means of heavy-tailed Student t-distribution with one degree of freedom. Using a heavy-tailed Student t-distribution avoids the superimposition of data points on projecting high-dimensional data points to lower dimension, also known as the "crowding problem". The t-SNE then tries to find a set of low-dimensional data points that minimizes the mismatch between the two probability distributions. Note that the distances between the clusters in the low-dimension may not be meaningful since dissimilar data points that are modeled by large pairwise distances are strongly repelled by the t-SNE. Moreover, while constructing the joint probabilities in the high-dimension, a free parameter known as "perplexity" which can be roughly defined as the number of nearest neighbors, needs to be manually set and controls the size of the clusters in the low-dimensional map.

For an extensive overview on the SOAP method and the t-SNE algorithm, I suggest the interested reader to refer to Ref. [136, 147, 148] and Ref. [145, 149], respectively.

2.8 MONTE CARLO SIMULATIONS

Monte Carlo (MC) methods are a powerful approach to solve problems in statistical physics and chemistry. MC methods are based on statistical sampling and were first employed in 1940s to solve multi-dimensional integrals and other intractable numerical problems [150]. The basic idea behind Monte Carlo methods is to allow the calculation of the physical properties of a system by repeated random sampling. For example, one can employ these methods to investigate phase transitions in magnetic materials, study of growth phenomena, etc. In the following, I summarize the main idea underlying the MC methods and briefly introduce the Metropolis algorithm. A good overview of MC methods can be found in the books by Landau and Binder [151], Lesar [152], and Frenkel and Smit [153] which were used for writing this section.

In the canonical ensemble (constant temperature T, constant number of particles N, and a constant volume V), the thermodynamic average is given by

$$\langle A \rangle = \frac{\sum_\alpha e^{-\frac{E_\alpha}{k_B T}} A_\alpha}{\sum_\alpha e^{-\frac{E_\alpha}{k_B T}}} = \sum_\alpha A_\alpha \rho_\alpha, \tag{52}$$

where k_B is Boltzmann constant, E_α is the energy of the system in configuration α, A_α is some observable, and ρ_α is the probability of being in a specific configuration given as:

$$\rho_\alpha = \frac{e^{-\frac{E_\alpha}{k_B T}}}{\sum_\alpha e^{-\frac{E_\alpha}{k_B T}}} = \frac{e^{-\frac{E_\alpha}{k_B T}}}{Z}. \tag{53}$$

Here the partition function Z is

$$Z = \sum_\alpha e^{-\frac{E_\alpha}{k_B T}}, \tag{54}$$

and the sum is over all possible configurations of the system. Estimating the average in Eq. 52 is a challenging task as there are infinite number of possible configurations. However, by employing certain approximations, this can be overcome. For example, one can employ *importance sampling* where only those configurations are considered that are probable according to a certain probability distribution (e.g. Boltzmann distribution). This sampling can be obtained by using a Markov process. Markov processes generates a new configuration ν, of the system given its current state, μ. The transition from μ to ν is governed by the transition probability $P(\mu \rightarrow \nu)$ and should fulfill the constraint

$$\sum_\nu P(\mu \rightarrow \nu) = 1, \tag{55}$$

as the Markov process must generate some configuration ν given a system in the configuration μ. To ensure that the configurations generated using a Markov process are according to the Boltzmann distribution, two more conditions needs to be fulfilled: *ergodicity* and *detailed balance*. The ergodicity ensures that if the Markov process is run long enough, then it should be able to reach any configuration of the system from any initial configuration. The second condition of detailed balance ensures that the Boltzmann distribution is reached when the system acquires equilibrium.

2.8.1   *Metropolis algorithm*

The Metropolis Monte Carlo algorithm introduced by Metropolis *et al.* [154] in 1953, is one of the most famous and widely used MC algorithm. The key idea is to sample a phase space in such a way that a particular configuration, α occurs in the sampling according to a probability ρ_α. The sampling mainly focuses on the relative probabilities of the configurations and the average quantities can be determined from the outcome which is a set of configurations with the correct probability. In its simplest form, one starts a system at a configuration μ with energy E_μ and a trial move is made to a new configuration ν and the

energy in the new configuration E_ν is calculated. The trial move to the new configuration is accepted or rejected according to

$$
P_{\mu\to\nu} = \begin{cases} e^{-\frac{E_\nu - E_\mu}{k_B T}}, & \text{if } E_\nu - E_\mu > 0 \\ 1, & \text{else.} \end{cases}
\tag{56}
$$

If the energy of the new configuration ν is lower or equal to that of the initial configuration μ, then the trial move to the new configuration is always accepted. On the other hand, if the energy E_ν is higher than energy E_μ, then the trial move is accepted according to the probability given in Eq. 56. Fig. 7 show the implementation of the Metropolis algorithm.

In this thesis, I have employed MC simulations to (1) investigate the temperature dependence of the chemical long-range order parameter for the ferromagnetic and paramagnetic phase in $L1_0$-FeNi and, (2) estimate the Curie temperature in the ordered and disordered phase of $L1_0$-FeNi.
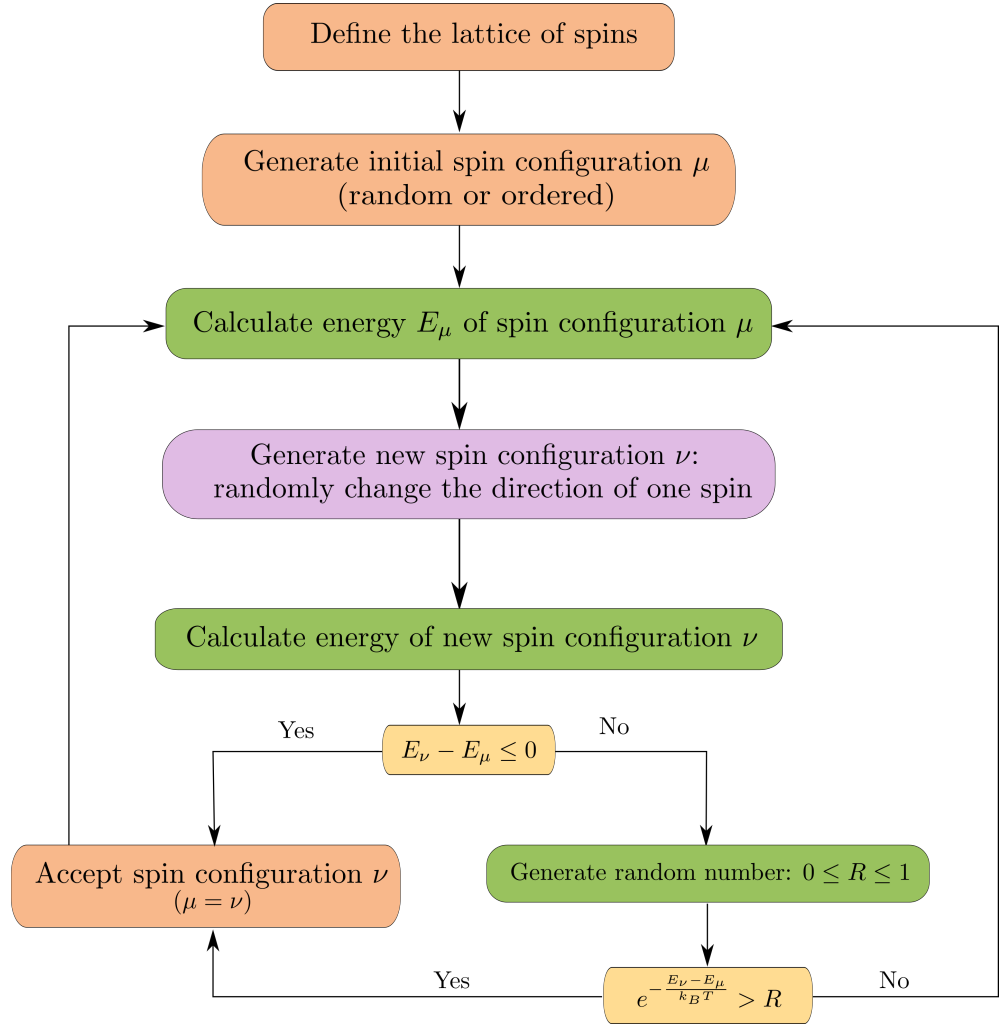
Figure 7: Implementation of Metropolis Monte Carlo method to calculate the magnetic transition temperature in the ordered and disordered phase in $L1_0$-FeNi.

COUPLING BETWEEN CHEMICAL AND MAGNETIC PROPERTIES IN L1$_0$-FENI

In this chapter, I present our work on the DFT calculations to establish the coupling between magnetic and chemical orders in L1$_0$-FeNi. Most importantly, I show the effect of chemical disorder on the MAE and the orbital moment anisotropy (OMA) and further discuss how OMA can be used as a substitute to optimize the MAE in L1$_0$-FeNi. I start with the motivation and discuss about the work that has already been done before, which is then followed by the project summary. Finally, I discuss the implications of the project.

3.1 MOTIVATION

As already discussed in Sec. 1.3, the laboratory synthesis of the fully ordered phase from the disordered one is extremely challenging and, therefore, it is hard to measure the magnetic properties of the ordered phase. Thus, it is vital to understand how magnetic properties depend on the degree of chemical order. In the following, I provide more detailed discussion of previous theoretical studies where a strong coupling between chemical and magnetic order was found in L1$_0$-FeNi.

In Ref. [70], a Monte-Carlo study based on Ising approximation was performed to estimate the magnetic and chemical order-disorder transition temperatures for various stoichiometries of FeNi. Calculations were performed for three different cases. First, by considering only magnetic interactions for fixed chemical order, second, by considering only chemical interactions, and finally, when both magnetic and chemical interactions are considered simultaneously. Authors found that not only the degree of chemical order has large effect on the magnetic transitions but the effect of magnetism on the chemical ordering process is also rather large. Moreover, they showed that above the magnetic and chemical ordering temperatures, both the magnetic and chemical short-range interactions continue to be important simultaneously in estimating the magnetic and chemical properties.

In Ref. [71], Lavrentiev *et al.* investigated the magnetic and thermodynamic properties of fcc FeNi alloys by developing a model based on magnetic cluster expansion simulations. They employed the Heisenberg-Landau Hamiltonian in these simulations which was parameterized using *ab initio* density functional theory calculations. To investigate the temperature dependence of magnetism, they used Monte-Carlo simulations and showed that the Curie temperature of the chemically ordered

phase is enhanced by about 550 K relative to the Curie temperature of the chemically disordered phase.

In a more recent study, which was performed in parallel to our work, Tian *et al.* [72], investigated the order-disorder transition temperature in Fe-Ni by employing the exact muffin-tin orbitals method based on DFT in combination with the coherent-potential approximation (CPA) to treat the chemical disorder. From their Monte-Carlo calculations based on the calculated Heisenberg exchange parameters, they showed an increase in the Curie temperature from 630 K for the chemically disordered phase to about 780 K for the fully ordered phase.

From these findings it becomes clear that there is a strong interaction between magnetic and chemical degrees of freedom. Taking these results as the starting point, we first investigate using first-principles-based DFT calculations, the effect of magnetic state on the chemical properties and vice-versa, by employing a supercell approach to model the chemical disorder. Note that our study provides complementary insights to the previous studies employing effective medium type approaches to model the chemical disorder and also aim to show how well can PBE functional describe the properties in L1$_0$-FeNi. With these insights, we then investigate the effect of chemical disorder on the MAE which is the main aspect of this work. Following this, we then discuss how OMA can be utilized to further optimize the MAE in L1$_0$-FeNi.

3.2 SUMMARY OF RESULTS

In order to determine the energetics of both chemical and magnetic order-disorder transitions, we first determine the total energy as a function of long-range chemical order parameter, P_z, (as defined in Sec. 2.6) in L1$_0$-FeNi. For each of the order parameter $P_z < 1$, we sample over fifty $2 \times 2 \times 2$ supercells of the conventional 4-atom cubic cell (see Fig. 1 of Paper [1]). Note that for the conventional 4-atom cubic cell, we keep the lattice parameters fixed to $a = 3.560$ Å so that $c/a = 1$. Therefore, we neglect the small tetragonal strain in the conventional cell which according to our test calculations lead to a negligible change in the total energy of the fully ordered system.

From the total energy calculations, we find that fully ordered configuration ($P_z = 1$) is the one with the lowest energy while (partially) disordered configurations are higher in energy (see Fig. 3 of Paper [1]). Note that we simply take the average of the total energies of all 50 configurations for each P_z as we did not find any correlation between the MAE and the total energy of various configurations, that would indicate an energetic preference for either larger or smaller MAE. Our results agree well with those by Tian *et al.* [72] where they employ *ab initio* calculations within the exact muffin-tin orbitals method for total energy calculations and use CPA to model the compositional disorder. This shows that the local chemical environment effects often neglected

in the CPA approach are not really essential for the total energy calculations in this system.

We then perform Monte-Carlo simulations to estimate the order-disorder transformation temperature with ferromagnetic and paramagnetic order. To model the paramagnetic state, we employ disordered local moment (DLM) method [155]. Within the DLM method, paramagnetic state is modeled by randomly initializing the directions of magnetic moments in the supercell. The energy of the paramagnetic phase is obtained by averaging over the energy of a sufficient amount of randomly generated configurations. For the fully ordered case, we generate 100 collinear DLM configurations, while for the chemically disordered case, we generate 10 DLM configurations for each of the 10 different chemically disordered configurations. Note that we randomly initialize the direction of the magnetic moments only for Fe atoms and not explicitly for Ni atoms. Ni magnetic moments tend to disappear when the neighboring Fe magnetic moments are antiparallel to each other or in other cases, reorient themselves to either up or down, depending on the direction of the neighboring Fe magnetic moment. Moreover, we only consider collinear configurations i.e., magnetic moment directions as either up or down.

Fig. 6 in Paper [1] reveal that the chemical order-disorder transition temperature for the ferromagnetic state is significantly higher than that for the paramagnetic state, indicating a strong impact of the magnetic state on the chemical order-disorder transition temperature. Furthermore, we note that the difference in the average total energies between the chemically ordered and chemically disordered case is significantly larger for the paramagnetic case as compared to the ferromagnetic case. This indicates that the magnetic state also affects the chemical order-disorder transition temperature in $L1_0$-FeNi.

Next, we calculate the MAE as a function of the chemical long-range order parameter using the magnetic force theorem as described in Sec. 2.3. We first perform convergence tests of the MAE with respect to the **k**-points. Fig. 8 shows the convergence of the MAE as a function of the **k**-points for the fully ordered structure. One can see that at least a $14 \times 14 \times 14$ **k**-mesh (corresponding to 2744 **k**-points) is required to achieve a well converged value of the MAE.

For each $P_z < 1$, we again sample over 50 ferromagnetic $2 \times 2 \times 2$ supercells relative to the conventional 4-atom cubic cell. For $P_z = 0$, we obtain an average MAE of around $0\,\mu\mathrm{eV/f.u.}$ This indicates that we sample over a sufficient amount of configurations since for a chemically disordered system with cubic symmetry, the magnetization has no preference for any of the orthogonal crystallographic axis. Our MAE calculations in Fig. 7 of Paper [1] reveal an increase in the MAE with increasing order parameter and one can see that the MAE already reached its maximal value at $P_z = 0.75$. This shows that a partial chemical disorder by around 25% in the $L1_0$ structured FeNi does not
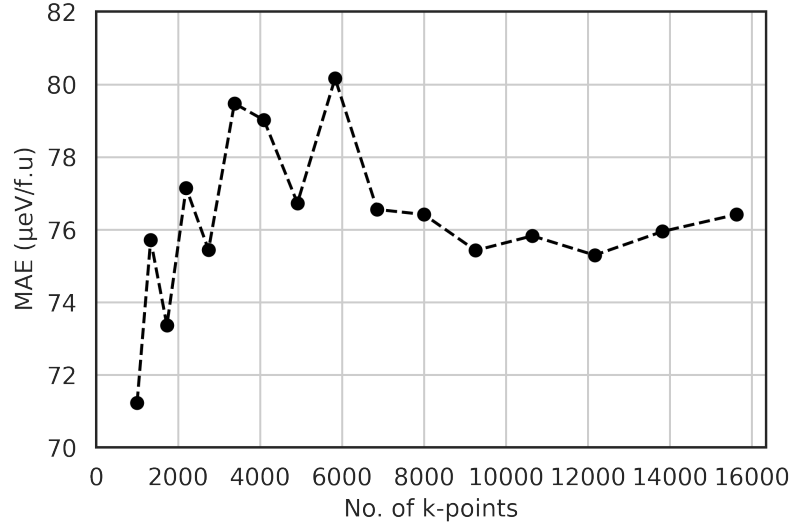
Figure 8: Convergence of the MAE with respect to the **k**-points for a fully ordered $2 \times 2 \times 2$ supercell of the conventional 4-atom cubic cell. The MAE is given per formula unit which corresponds to 1 Fe and 1 Ni atom in a primitive unit cell.

lead to a significant decrease in the MAE. Most importantly, we find that for long-range order parameters $P_z = 0.75$ and 0.5, some configurations have higher MAE than the fully ordered case. To investigate this further, we calculate orbital magnetic moment anisotropy which can provide insights into which local chemical environment contribute to an overall higher value of MAE.

According to Bruno's model [116, 156], under certain limitations and approximations, the orbital magnetic moment anisotropy is proportional to the MAE. In Fig. 8 of Paper [1], one can see total as well as atom-resolved OMA as a function of chemical long-range order parameter. It is clear that the main contribution to the total OMA for $P_z < 1$ comes from the anisotropy of Fe orbital moment, while the OMA from Ni atoms is rather very small. For the perfectly ordered case ($P_z = 1$), Ni orbital moments are larger along [100] than [001], which results in the negative OMA and, thus, leading to a small decrease in the total OMA as one goes from $P_z = 0.75$ to 1. Furthermore, we note that both OMA and the MAE follows a similar behaviour as a function of increasing long-range order parameter. This leads to a question of whether OMA and the MAE are correlated. Fig. 9 of Paper [1] illustrates this where the MAE is plotted as a function of the average Fe OMA for all individual configurations with different values of P_z. One can see a linear correlation between both quantities which is indicated by a least mean square fit to all data points.

3.3 IMPLICATIONS AND FURTHER WORK

In this project, we demonstrate that there exists a strong interaction between the magnetic and chemical degrees of freedom in $L1_0$-FeNi by employing supercell approach to model the chemical disorder. In particular, we show that the chemical order-disorder transition temperature obtained from the Monte-Carlo simulations is strongly reduced when one goes from ferromagnetic to paramagnetic state. Thus, this indicates the effect of magnetic state on the chemical order-disorder transition temperature. On the other hand, we also note the lower average total energy difference between the ferromagnetic and paramagnetic states for chemically disordered alloy as compared to the chemically ordered FeNi. This as a result leads to the lower Curie temperature of the chemically disordered phase than that of the chemically ordered phase consistent with previous studies [71, 72]. Thus, this indicates the effect of chemical state on the magnetic transition temperature. Our results are consistent with previous studies employing effective medium approaches to model the chemical disorder and shows that PBE functional correctly describes the underlying energetics in the FeNi system.

Most importantly, from our MAE calculations as a function of long-range order parameter, we show that a decrease in the order parameter by about 25% does not lead to a significant decrease in the MAE as compared to that of the fully ordered FeNi. Since, synthesizing fully ordered sample in the laboratories is extremely challenging, our results are rather encouraging indicating that fully ordered samples are not required to obtain a full MAE.

Furthermore, our calculations show partially disordered configurations with the MAE higher than that of the fully ordered structure which indicates the possibility of further increasing the MAE in this alloy. Moreover, we demonstrate a linear correlation between the MAE and the OMA of Fe atoms which suggests that one can use OMA as a proxy for a local atomic contribution to the MAE. Hence, one can optimize the MAE in $L1_0$-FeNi by carefully designing configurations containing the local atomic environment that leads to high OMA. This is further discussed in the next chapter.

We also note that our calculated MAE ($0.54\,\mathrm{MJ/m^3}$) for fully ordered structure ($P_z = 1$) is slightly smaller than the value obtained experimentally for samples with a chemical long-range order parameter of about 0.5 ($\approx 0.7\,\mathrm{MJ/m^3}$) in Ref. [69]. This indicates that we underestimate the true MAE for our system. In a study by Ravindran *et al.* [157] and Miura *et al.* [73], they showed that by including the so-called *orbital polarization correction*, the MAE of the fully ordered system is enhanced by a factor 2. Without the orbital polarization correction, one usually underestimates the calculated orbital magnetic moments e.g., in Fe and Co phases [158] as the effects responsible for the Hund's second rule are absent. Therefore, to incorporate the Hund's second

rule in our calculations, we employ DFT+U which is described later in Chapter 5.

3.4 PUBLICATION

This work is published as *»Interplay between chemical order and magnetic properties in L1$_0$-FeNi (tetrataenite): A first-principles study«* in Physical Review Materials, see Reference [1]. Copyright (2020) by the American Physical Society.

Interplay between chemical order and magnetic properties in L1$_0$ FeNi (tetrataenite): A First-Principles Study

Ankit Izardar and Claude Ederer

Materials Theory, ETH Zürich, Wolfgang-Pauli-Strasse 27, 8093 Zürich, Switzerland

(Dated: June 13, 2022)

We use first-principles-based calculations to investigate the interplay between chemical order and the magnetic properties of $L1_0$ FeNi. In particular, we investigate how deviations from perfect chemical order affect the energy difference between the paramagnetic and ferromagnetic states as well as the important magneto-crystalline anisotropy energy. Our calculations demonstrate a strong effect of the magnetic order on the chemical order-disorder transition temperature, and conversely, a strong enhancement of the magnetic transition temperature by the chemical order. Most interestingly, our results indicate that the magnetic anisotropy does not decrease significantly as long as the deviations from perfect order are not too large. Moreover, we find that in certain cases a slight disorder can result in a higher anisotropy than for the fully ordered structure. We further analyze the correlation between the magneto-crystalline anisotropy and the orbital magnetic moment anisotropy, which allows to study the effect of the local chemical environment on both quantities, potentially enabling further optimization of the magneto-crystalline anisotropy with respect to chemical order and stoichiometric composition.

I. INTRODUCTION

Magnetic materials are ubiquitous and play a pivotal role in many technological applications ranging from consumer electronic devices to electric power production and conversion. In particular, high performance permanent magnets form crucial components in the devices used for generating electric power from renewable energy sources such as wind, hydro, tidal, etc. The strength of a permanent magnet is quantified by the maximum magnetic energy product $(BH)_{max}$, i.e, the product of the remanence B_r and the coercivity H_c. Thus, high performance permanent magnets are typically composed of rare-earth elements (Sm, Nd, Dy, etc.), which provide high resistance to demagnetization, in combination with transition-metals (Fe, Co, etc.), which provide high saturation magnetization. Specifically, magnets belonging to the SmCo family (e.g. SmCo$_5$ and Sm$_2$Co$_{17}$), with energy products in the range of 5-20 MGOe (40-160 kJ/m^3) [1, 2], and the NdFeB family (e.g. Nd$_2$Fe$_{14}$B), with energy products in the range 5-50 MGOe (40-400 kJ/m^3) [3], are currently the best-performing *supermagnets*. However, the volatility in price and uncertainty of supply of the required rare earth elements, makes it highly desirable to find alternatives to these rare-earth based magnets, in order to meet the increasing global demand for permanent magnets [4, 5].

An interesting candidate in this respect is the chemically-ordered L1$_0$ phase of Fe$_{50}$Ni$_{50}$ (tetrataenite), which has been found in iron meteorites [6–10]. The Fe and Ni atoms in tetrataenite occupy alternating planes of the underlying fcc lattice oriented perpendicular to the c axis (see rightmost graph in Fig. 1), resulting in a structure with tetragonal symmetry and a high magneto-crystalline anisotropy energy (MAE) ($> 7 \cdot 10^6$ erg cm^{-3}), large saturation magnetization (~ 1270 emu cm^{-3}), and a projected energy product of 42 MGOe (335 KJ/m^3) [11–14]. In contrast, the disordered phase, where Fe and Ni

atoms are randomly distributed over the sites of the fcc lattice (see leftmost graph in Fig. 1), exhibits only a very small MAE.

Unfortunately, the laboratory synthesis of the ordered phase is extremely challenging due its rather low order-disorder transition temperature, $T_{od} \sim 593$ K [15], and the slow diffusion of atoms at this temperature, which is of the order of one atomic jump per 10^4 years at 573 K [16]. Since its discovery, several attempts have been made to achieve a high degree of chemical order in this alloy [17–20]. Nevertheless, synthesis of a fully ordered system remains challenging.

The low order-disorder temperature and the difficulties in synthesizing fully ordered samples make it also very challenging to fully characterize the magnetic properties of tetrataenite, as the disordering occurs below the predicted Curie temperature. It also raises the question of how the favorable magnetic properties depend on the degree of chemical order.

Several previous studies have found a strong coupling between the magnetic and chemical orders in this system. For example, both Dang *et al.* [21] and Lavrentiev *et al.* [22] found, using different models and approximations, that the ferromagnetic Curie temperature is drastically enhanced in the chemically ordered case compared to the random alloy (from ~ 450 K to over 1000 K in Ref. 22) and that also the magnetic interactions strongly increase the chemical order-disorder transition temperature (by ~ 100 K in Ref. 21). This suggests that it is necessary to include both chemical and magnetic degrees of freedom to accurately describe this system.

In this work, we present additional complementary insights on the interplay between chemical order and magnetic properties in tetrataenite by means of first-principles-based density functional theory (DFT) and Monte Carlo simulations. In particular, we study how the MAE depends on the degree of chemical order in the system. We find that small deviations from perfect or-
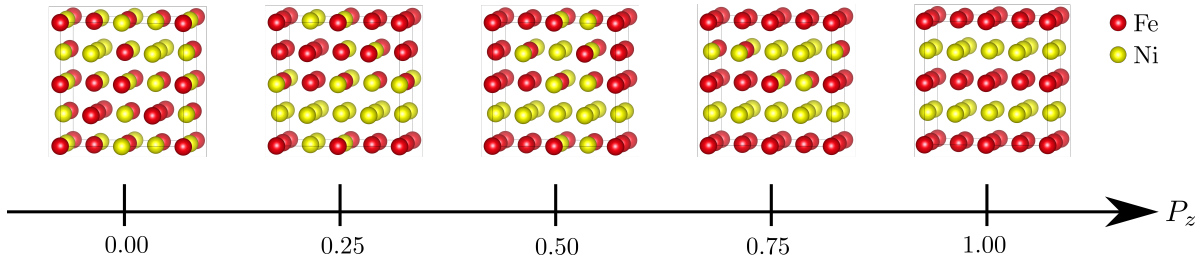
FIG. 1. Examples of atomic configurations corresponding to different values of the long range order parameter P_z, depicted in a $2 \times 2 \times 2$ supercell relative to the conventional 4-atom cubic cell. Fe and Ni atoms are represented by red and yellow spheres, respectively. In the chemically ordered $L1_0$-FeNi phase (tetrataenite) with $P_z = 1$, Fe and Ni atoms occupy alternate layers perpendicular to c. In the fully disordered A1 phase ($P_z = 0$), they randomly occupy sites of the underlying fcc lattice.

der do not lead to a significant reduction of the magnetic anisotropy, and that in some cases a small amount of disorder can even enhance the MAE. We then discuss the anisotropy of the local orbital moments as an indicator that allows to further optimize the magnetic anisotropy with respect to the local atomic environment.

The remainder of the paper is structured as follows. In Sec. II we first define the long range order parameter, then describe how we model the partially disordered as well as the paramagnetic state in FeNi, and introduce the computational methods used throughout this work. In Sec. III, we then discuss our results regarding the energetics of the order-disorder transition, the effect of chemical disorder on the MAE, and the correlation between orbital magnetic moment anisotropy and the MAE. Finally, in Sec. IV, we conclude by summarizing our main findings.

II. MODELS AND METHODS

A. Modeling of chemical disorder

To define the long range order parameter for the $L1_0$ chemical order, we divide the fcc lattice into four individual sublattices, α, β, γ, and δ, according to the four different sites in the conventional 4-atom cubic unit cell (see Fig. 2). The fully ordered $L1_0$ structure can then be described in three different ways, corresponding to arrangements of different atomic species in alternating planes perpendicular to the three Cartesian axes. Thereby, always two sublattices are fully occupied by one type of atom, while the other two sublattices are occupied by the other type. For example, alternating atomic planes perpendicular to z correspond to occupation of sublattice α and β by one type of atom and occupation of sublattices γ and δ by the other type, whereas for alternating planes perpendicular to x, sublattices α and δ are occupied by one type of atom and sublattices β and γ by the other type.

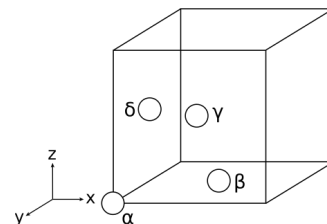We can now define long range order parameters for the

FIG. 2. Depiction of the four sites of the fcc lattice within the conventional cubic unit cell, defining the four sublattices α, β, γ, and δ.

three different orientations of the $L1_0$ order as follows:

$$P_x = p_\alpha^{\text{Fe}} + p_\gamma^{\text{Fe}} - 1 \quad , \tag{1}$$

$$P_y = p_\alpha^{\text{Fe}} + p_\delta^{\text{Fe}} - 1 \quad , \tag{2}$$

$$P_z = p_\alpha^{\text{Fe}} + p_\beta^{\text{Fe}} - 1 \quad , \tag{3}$$

where p_i^{Fe} is the probability that a site on sublattice i is occupied by an Fe atom. These probabilities have to fulfill the condition $\sum_i p_i^{\text{Fe}} = 2$ (on average 2 Fe atoms per 4-atom unit cell), and thus only three can be chosen independently. Furthermore, each p_i^{Fe} can only vary between 0 and 1, imposing an additional constraint on the p_i^{Fe}. Nevertheless, Eqs. (1)-(3) can be inverted and the probabilities p_i^{Fe} are then uniquely defined by specifying the three components of the long range order parameter within the allowed range.

To model the system with a given value for the long-range order parameter, we generate 50 configurations, using a $2 \times 2 \times 2$ supercell of the conventional cubic cell. For each configuration, we randomly distribute 16 Fe and 16 Ni atoms over the 32 available sites, according to the probabilities p_i^{Fe} corresponding to a fixed value of P_z and $P_x = P_y = 0$. The chosen supercell size allows to obtain five different values for the long range order parameter, $P_z \in \{0, 0.25, 0.5, 0.75, 1\}$. We then calculate the total energy for each configurations using density functional theory (DFT), as described in Sec. II C. The total energy

for a given order parameter is then obtained by averaging over the corresponding configurations.

We note that most previous first-principles-based studies, e.g., Ref. 23, have employed effective medium/mean-field type approaches to model the compositional disorder. While our complementary approach is computationally more demanding, since it requires sampling over many configurations, it also incorporates effects of disorder within the local environment, which turns out to be especially important in the case of the MAE.

B. Modeling of the paramagnetic state

It is well known that in most magnetic materials local magnetic moments still exist above the Curie temperature, even though the material does not exhibit any macroscopic (long-range) magnetic order. The incorporation of such local moments is very important to correctly describe the electronic structure of these materials, and thus the paramagnetic phase cannot simply be treated as a non-magnetic state in DFT-based first-principles calculations.

In order to model the paramagnetic state, we therefore employ the disordered local moment (DLM) method [24], where the directions of magnetic moments are constrained to random directions. Analogously to our treatment of chemical disorder, we use a supercell approach and sample over a sufficient amount of randomly generated configurations [25]. The average of the energy over all configurations then represents the energy of the paramagnetic phase (in the limit of very high temperature).

For the chemically ordered case, we generate 100 collinear DLM configurations by randomly initializing the magnetic moments of the Fe atoms in a $2 \times 2 \times 2$ supercell as either up or down. For the chemically disordered case, we create 10 different chemically disordered configurations (as described in Sec. II A) and then generate 10 DLM configurations for each of these configurations. We do not explicitly initialize the Ni magnetic moments, since the Ni moments tend to vanish if the surrounding Fe magnetic moments are oriented anti-parallel to each other. In other cases, the Ni moments will converge to either up or down, depending on the orientation of moments on the surrounding Fe atoms. Therefore, we do not take into account the directions of the Ni moments as independent variables. We also do not consider any noncollinear configurations. These are not expected to alter the results if the basic assumptions of the DLM method are valid, but would significantly increase the required computational effort.

To verify our sampling of the paramagnetic state, we evaluate the nearest-neighbor spin-correlation function for the magnetic moments of the Fe atoms [26]:

$$\Phi = \frac{1}{N_{\text{Fe}}} \sum_i \frac{1}{N_i} \sum_j \hat{e}_i \cdot \hat{e}_j \quad , \tag{4}$$

where the sum over i goes over all N_{Fe} Fe atoms in the supercell ($N_{\text{Fe}} = 16$ in the present case), the sum over j goes over all Fe nearest neighbors for each i (with N_i being the number of Fe nearest neighbors of atom i, which is different for each individual configuration), and $\hat{e}_i$ is the direction of the magnetic moment of Fe atom i.

C. Computational methods

All DFT calculations are performed using the Vienna *ab initio* Simulation package (VASP) [27], the projector-augmented wave method (PAW) [28, 29], and the generalized gradient approximation according to Perdew, Burke, and Ernzerhof [30]. Brillouin zone integrations are performed using the tetrahedron method with Blöchl corrections and a Γ-centered $14 \times 14 \times 14$ **k**-point mesh. The plane wave energy cut-off is set to $350\,\text{eV}$, and the total energy is converged to an accuracy of $10^{-8}\,\text{eV}$. Our PAW potentials include $3p$, $4s$, and $3d$ states in the valence for both Fe and Ni .

The MAE is calculated using the magnetic force theorem [31, 32], i.e., by including the spin-orbit coupling in a non-self-consistent calculation, using the charge density converged without spin-orbit coupling, and then taking the difference in energies between two different orientations of the magnetization direction.

We define the MAE as the energy difference $E^{[100]} - E^{[001]}$, where $E^{[100]}$ and $E^{[001]}$ are the total energies obtained with magnetization aligned along the [100] and [001] directions, respectively. Thus, the MAE is defined as positive when the magnetic easy axis lies along the [001] direction, which is the reported easy axis for $L1_0$ FeNi [14, 15]. To check the convergence of the MAE with respect to the **k**-point sampling, we perform calculations using up to $25 \times 25 \times 25$ **k**-points and find that the MAE is sufficiently converged (to about $\pm 1\,\mu\text{eV/f.u.}$) for our purposes using a $14 \times 14 \times 14$ **k**-point mesh.

The temperature dependence of the chemical long-range order parameter is obtained from simple Monte Carlo simulations, considering an fcc lattice using a $\sqrt[3]{N} \times \sqrt[3]{N} \times \sqrt[3]{N}$ supercell of the conventional cubic cell, containing $4N$ sites over which we distribute Fe and Ni atoms in equal proportion. For a given temperature, we perform Monte Carlo sweeps using the Metropolis algorithm, where in each trial step the configuration is varied by exchanging the positions of an arbitrarily chosen pair of Fe and Ni atoms, then calculating the long range order parameter $\mathbf{P} = (P_x, P_y, P_z)$, and evaluating the corresponding total energy as described in Sec. III A.

III. RESULTS AND DISCUSSION

A. Energetics of the order-disorder transition

We first determine equilibrium lattice parameters for perfectly ordered $L1_0$ FeNi in the ferromagnetic state.
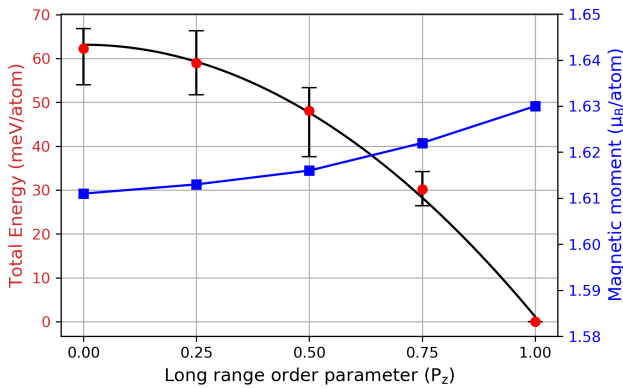
FIG. 3. Total energy (per atom) and average magnetic moment (per atom) as function of the long range order parameter P_z (with $P_x = P_y = 0$), calculated for perfect ferromagnetic order. Red dots represent the mean over 50 configurations for each $P_z < 1$. Error bars indicate the highest and lowest energies of the individual configurations. The black curve shows a quadratic fit to the data. Energies are defined relative to the fully ordered state ($P_z = 1$). Filled squares represent the mean of magnetic moments over 50 configurations for each $P_z < 1$. The blue line is a guide to the eye.

We obtain lattice parameters $a = 3.560\,\text{Å}$ and $c = 3.577\,\text{Å}$ ($c/a = 1.0048$). Our calculated lattice parameters agree well with the values measured in experiments ($a = 3.560\,\text{Å}$ to $3.582\,\text{Å}$ and $c = 3.589\,\text{Å}$ to $3.615\,\text{Å}$) [19, 33], and obtained in previous calculations ($a = 3.557\,\text{Å}$ to $3.560\,\text{Å}$ and $c = 3.570\,\text{Å}$ to $3.584\,\text{Å}$) [13, 34, 35].

Next, we determine the dependence of the total energy on the long range chemical order parameter, while keeping the perfect ferromagnetic order. For this, we calculate the total energy of 50 configurations for each value of P_z, generated as described in Sec. II A.

For simplicity, we keep the lattice parameters fixed corresponding to a metrically cubic unit cell with $a = 3.560$ Å and $c/a = 1$, i.e., we neglect the small tetragonal strain on the unit cell (which will also depend on the degree of long range order). Our test calculations for perfect chemical order ($P_z = 1$) show that these simplifications change the total energy by less than 5 meV/atom, which is negligible compared to the energy changes related to the different distributions of atoms. Furthermore, we do not perform any further optimization of atomic coordinates for the disordered configurations.

The corresponding total energies (averages as well as total spread over different configurations) are shown in Fig. 3 as function of the long range order parameter P_z, together with the average magnetic moment per atom. It can be seen that the averaged total energies are well fitted by a quadratic dependence on P_z, $E = E_0 - \Delta E P_z^2$, where $\Delta E = 62$ meV is the energy difference (per atom) between the perfectly ordered and completely disordered structure. We note that a quadratic dependence on P_z, or

more generally on $P = \sqrt{P_x^2 + P_y^2 + P_z^2}$ also corresponds to the leading order term allowed by symmetry for small fluctuations around the disordered state, $P = 0$, and also follows from a simple energetic model with only nearest neighbor interactions. The good quality of the quadratic fit thus also indicates that rather accurate (sufficient for our purposes) mean energies can be obtained by using 50 different configurations for each $P_z < 1$.

One can also see that the average total magnetic moment depends only weakly on P_z, increasing slightly from 1.611 μ_B to 1.630 μ_B between zero and full chemical order. We note that the increase in the total magnetic moment is mainly due to the average magnetic moment of the Fe atoms, while the average Ni magnetic moment remains fairly constant until $P_z = 0.75$, after which it slightly decreases for the perfectly ordered structure.

These results agree very well, both qualitatively and quantitatively, with recent calculations by Tian $et\ al.$ employing the coherent potential approximation (CPA) to treat the compositional disorder [23]. The good agreement between this complementary approach and our configurational sampling technique confirms on one side the good convergence of our data and on the other side also indicates that effects of the local environment, not included in the CPA approach, are not too relevant for the total energy and average magnetic moment.

In order to estimate the order-disorder temperature from the calculated $E(P_z)$, we perform simple Monte Carlo simulations, as outlined in Sec. II C. The total energy for each Monte Carlo configuration is evaluated from the quadratic fit in Fig. 3, i.e., $E = -4N\Delta E P^2$, with $\Delta E = 62$ meV. The resulting temperature dependence of the long range order parameter is shown in Fig. 6 using a system size of $N = 10^3$ (see Sec. II C). Using larger system sizes does not lead to any noticeable changes.

It can be seen that the order parameter vanishes around 1400 K, which is significantly higher than the reported experimental value for the order-disorder transition temperature of 593 K [15]. It is also significantly above the predicted ferromagnetic Curie temperature for L1$_0$ FeNi [22, 34]. Thus, assuming perfect ferromagnetic order when obtaining ΔE is probably not justified. In the following, we re-calculate the energy difference between chemically ordered and disordered states for the paramagnetic case, using the DLM approach [24], as described in Sec. II B).

To confirm that our sampling over a sufficient amount of randomly chosen DLM configurations converges as expected, Fig. 4 shows the nearest-neighbour spin correlation function (see Eq. (4)) for different chemically ordered and disordered magnetic configurations, evaluated from the converged magnetic moment directions, together with their cumulated averages, obtained by averaging over an increasing number of configurations. One can see that the cumulated average of the spin correlation function approaches zero both for the chemically ordered and the chemically disordered magnetic configurations, which shows that the amount of configurations we av-
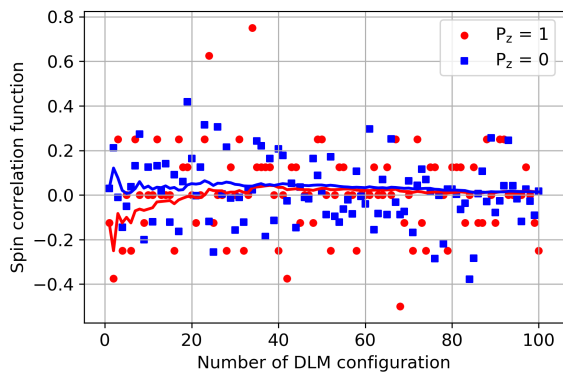
FIG. 4. Calculated spin correlation functions for 100 DLM configurations for both chemically ordered ($P_z = 1$) and chemically disordered ($P_z = 0$) configurations. Solid red and blue lines represent the cumulative averages for $P_z = 1$ and $P_z = 0$, respectively.
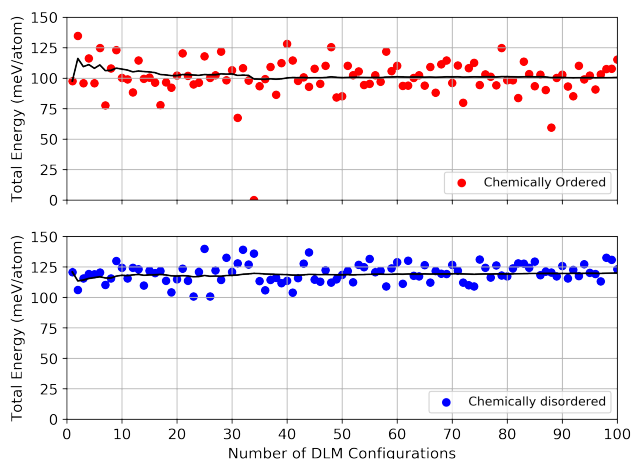

FIG. 5. Calculated total energies (per atom) for 100 DLM configurations generated for the chemically ordered ($P_z = 1$, top) and the chemically disordered ($P_z = 0$, bottom) case, using a $2 \times 2 \times 2$ supercell. The cumulative averages are shown as solid black lines.

TABLE I. Average total energies (in meV/atom) of the ferromagnetic and the paramagnetic states for chemically ordered and chemically disordered FeNi (relative to the ferromagnetic chemically ordered case).

	$L1_0$-FeNi (chemically ordered)	A1-FeNi (chemically disordered)
Ferromagnetic	0	62
Paramagnetic	101	120

case. It can be seen that the energy difference between the chemically ordered and the chemically disordered case is drastically reduced in the paramagnetic state compared to the ferromagnetic case (from 62 meV to about 20 meV per atom), indicating a strong coupling between chemical and magnetic order. Furthermore, the energy difference between the ferromagnetic and the paramagnetic state is also significantly reduced in the chemically disordered alloy compared to the case with perfect $L1_0$ order (from about 100 meV per atom to 58 meV per atom). This indicates that the magnetic Curie temperature of the chemically disordered phase is expected to be significantly lower than the (hypothetical) Curie temperature of the chemically ordered phase, which appears to be consistent with other theoretical studies [22, 23].

For $L1_0$-ordered FeNi, a magnetic Curie temperature of $T_C = 916$ K has been suggested, based on first principles DFT calculations [34]. This is more or less consistent with the value of ~ 1000 K obtained from simulations using a first-principles-based Heisenberg-Landau magnetic cluster expansion [22]. However, on heating the $L1_0$ order starts to disappear at temperatures around 700-800 K, depending somewhat on the heating rate [36]. Note that the actual reported chemical-order disorder temperature is much lower ($T_{od} = 593$ K [15]), but that the chemical order is kinetically stable up to temperatures where atomic diffusion becomes thermally activated. Therefore, it is clear that the predicted T_C for the ordered system is only a hypothetical Curie temperature, as the ordered phase is unstable at such high temperatures.

If we simply scale the predicted values for T_C of the chemically ordered case according to our obtained reduction of the ferromagnetic-paramagnetic energy difference, we obtain an estimate for the Curie temperature of chemically disordered FeNi of around 550 K, which however appears too low compared to experimental values of around 785-789 K [37, 38].

Interestingly, one should note that the temperature range where the chemical order effectively disappears ($\sim$ 700-800 K [36]) is quite similar to the Curie temperature of the disordered system. This means that once the system disorders, the magnetic order also disappears rather abruptly (see, e.g., Refs. 14 and 39).

As seen in Fig. 6, the reduced ΔE obtained for the paramagnetic state also leads to a strong reduction of the order-disorder temperature, obtained in our simple Monte Carlo simulations, to about 450 K. Note that these

erage over is sufficient, and that the magnetic moments indeed converge to the directions that were initialized.

Fig. 5 shows the total energies (per atom) obtained for the 100 DLM configurations corresponding to the chemically ordered ($P_z = 1$) and the chemically disordered ($P_z = 0$) case. The cumulative averages are indicated by the solid black lines. All energies are taken relative to the chemically ordered ferromagnetic case. Again one can see that, in spite of the large variations in the energies of the individual configurations, the averages converge rather well, and appear to be accurate to a few meV already after averaging over about 50 configurations.

Table I summarizes the average total energies obtained for the ferromagnetic and paramagnetic state, both for the chemically ordered and the chemically disordered
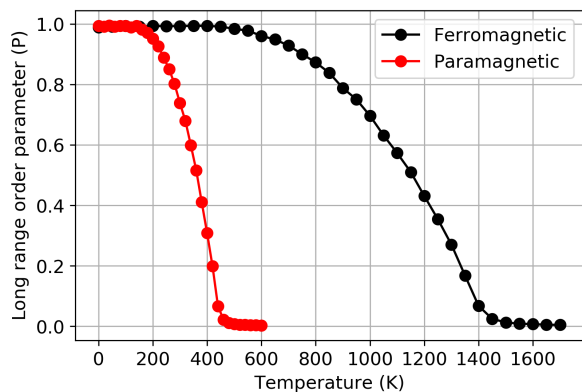
FIG. 6. Long range order parameter P as a function of temperature for the ferromagnetic (black) and paramagnetic (red) case, obtained from Monte Carlo simulations. The temperature at which the long range order parameter vanishes, indicates the corresponding order-disorder transition temperature.

FIG. 7. Calculated MAE, defined as $E_{[100]} - E_{[001]}$, as a function of the long range order parameter in FeNi, obtained for 50 different ferromagnetic configurations for each $P_z < 1$. Black dots represent the value for each configuration. Red dots correspond to the mean MAE for a particular P_z.

calculations are in principle expected to strongly underestimate the true order-disorder temperature, since the system is still magnetically ordered in that temperature range. On the other hand our simple approach neglects several other effects, e.g., lattice vibrations, which tend to reduce the order-disorder temperature [23, 40, 41]. Without considering such factors as well as kinetic effects, the temperature dependence of the order parameter is expected to follow the ferromagnetic curve for low temperatures and then move towards the paramagnetic curve once the magnetic order vanishes. Note, however, that the fully PM case considered here, with no short range correlations, is in principle only reached for $T \to \infty$. Thus, while our simplified model is not expected to quantitatively predict the order-disorder transition temperature, it can provide order of magnitude estimates and clearly indicates the strong coupling between the chemical order-disorder transition and the magnetic state in $L1_0$-FeNi.

B. Magneto-crystalline anisotropy

Several studies in the past have investigated the MAE in $L1_0$ FeNi by means of first-principles calculations [14, 34, 35, 42]. In addition, several experimentally measured values of MAE were also reported. However, very few investigations exists on the dependence of the MAE on the degree of chemical order in $L1_0$ FeNi. Kota and Sakuma [43] theoretically estimated the variation of MAE as a function of long-range order parameter for several $L1_0$ alloys including FeNi. They employed the tight-binding linear muffin-tin orbital method in conjunction with the CPA. They found that for FeNi, among other $L1_0$ alloys, the MAE is proportional to the power of the order parameter where the power varies from 1.6 to 2.4.
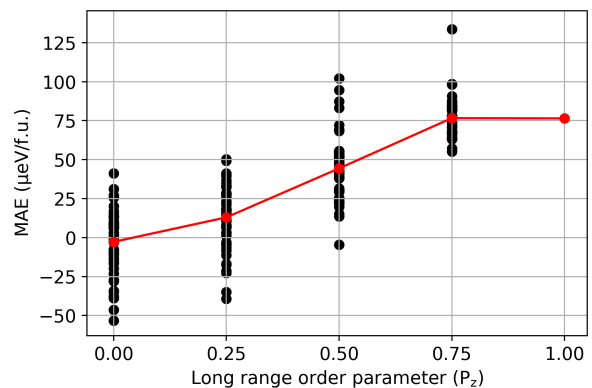
We calculate the dependence of the MAE on the long range order parameter by sampling over 50 ferromagnetic configurations for each value $P_z < 1$, as described in Sec. II C. Note that we also use the $2 \times 2 \times 2$ supercell to calculate the MAE for $P_z = 1$ to obtain consistent data. The results are plotted in Fig. 7, which shows the data for each individual configuration as well as the average value for each P_z. It can be seen that for $P_z = 0$, even though the MAE for the individual configurations shows a large spread of $\pm 50 \mu$eV/f.u., the obtained average is very close to the expected value of 0μeV/f.u. This indicates that we sample a sufficient amount of configurations to obtain reliable averages.

The MAE increases with increasing degree of chemical order, but, strikingly, reaches its maximal value already for $P_z = 0.75$. This means that the MAE does not decrease significantly if the deviations from perfect order are not too large. In view of the fact that perfectly ordered samples are very difficult to synthesize, this is an important result. We also note that our results do not follow the power-law behavior suggested by Kota and Sakuma (MAE $\propto P^{1.6\text{-}2.4}$) [43]. This is most likely due to their use of the CPA approximation to describe compositional disorder and shows that for a quantity such as the MAE, effects of the local environment can be very important. This is different from the total energy, shown in Fig. 3, which agrees well with previous CPA calculations [23]. Furthermore, for both $P_z = 0.75$ and $P_z = 0.5$, we find some configurations with even higher MAE than the fully ordered alloy. This indicates, that it might be possible to further increase the anisotropy of this system, beyond the value obtained for the stoichiometric 50:50 composition with perfect chemical order.

The MAE we obtain for the fully ordered case ($P_z = 1$) is 76μeV/f.u. corresponding to 0.54MJ/m^3, which agrees well with previous calculations using similar methods (0.56MJ/m^3 [35], 0.48MJ/m^3 [34], and
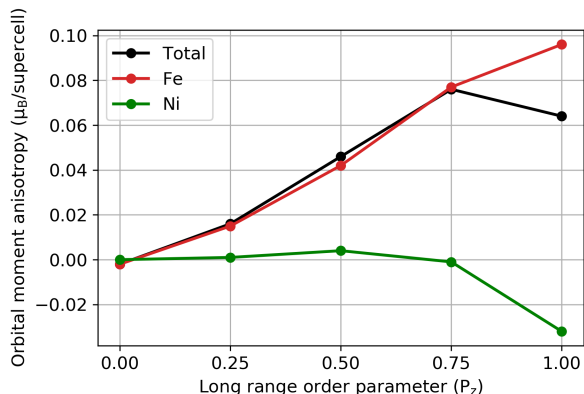
FIG. 8. Calculated total orbital moment anisotropy, $\Delta L = L_{[001]} - L_{[100]}$, averaged over all configurations with the same long range order parameter P_z, as a function of P_z Separate contributions of all Fe and all Ni atoms in the system are also shown.
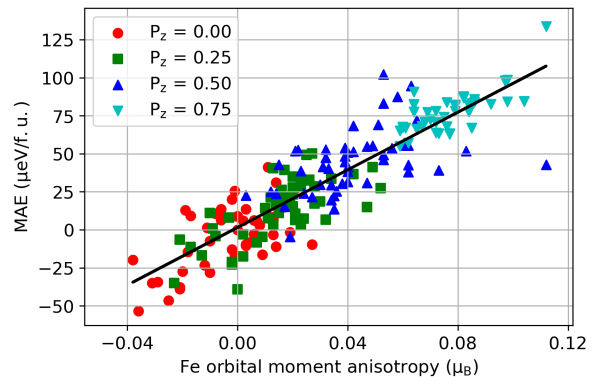

FIG. 9. MAE versus orbital moment anisotropy of the Fe atoms for each individual configuration. Configurations corresponding to different values of P_z are indicated by different markers. The solid black line corresponds to a least square fit to the data.

$0.47 \, \text{MJ/m}^3$ [44]). We note that this value is quite comparable, albeit slightly smaller, than what has been reported experimentally in Ref. [45] for samples with a long-range order parameter around 0.5 ($\approx 0.7 \, \text{MJ/m}^3$). On the other hand, for $P_z = 0.5$, we obtain a value that is clearly smaller than the experimentally reported MAE. This suggests that we are underestimating the true MAE of the system. Indeed, it has been shown, that including a so-called *orbital polarization correction* can enhance the MAE of the fully ordered system roughly by a factor of two [35, 46].

C. Orbital magnetic moment anisotropy

In order to obtain further insights into the origin of the MAE, we now analyze the orbital magnetic moment anisotropy as a function of long range order parameter. The orbital magnetic moment and its anisotropy is often closely connected to the MAE [47, 48]. In the present case it can potentially provide insights as to which local chemical environments are particularly favorable for obtaining a large MAE. We define the orbital moment anisotropy as $\Delta L = L_{[001]} - L_{[100]}$, where $L_{[001]}$ and $L_{[100]}$ are the total orbital magnetic moments (summed over all atoms in the $2 \times 2 \times 2$ supercell) when the magnetization lies along the [001] and [100] directions, respectively. Here, the sign is chosen such that the orbital anisotropy is positive if the orbital magnetic moments are larger along the [001] direction (which is the easy magnetic axis for L1$_0$ FeNi).

Fig. 8 shows the total as well as the atom-resolved orbital moment anisotropy as a function of the long range order parameter (i.e., averaged over all configurations corresponding to the same P_z). One can clearly see that the main contribution to the total orbital moment anisotropy for $P_z < 1$ comes from the anisotropy of the

Fe orbital magnetic moment, while the contribution from the Ni moments is almost negligible. For the perfectly ordered structure, we observe that the orbital magnetic moments of the Ni atoms are larger along the [100] direction, which results in a small decrease of the total orbital moment anisotropy as we go from $P_z = 0.75$ to $P_z = 1$ (see solid black curve in the Fig 8).

Note that both the MAE and the total orbital moment anisotropy show similar behaviour as one increases the long range order in the system. This suggests a possible explanation for the somewhat unexpected behavior of the MAE, provided that the MAE can be understood in terms of local contributions of the Fe and Ni atoms that correlate with the corresponding orbital moment anisotropies. Thereby, the (small) contribution to the MAE from the Ni atoms would be opposite to that of the Fe atoms and also be much more sensitive to deviations from perfect chemical order, such that it essentially vanishes already for $P_z \leq 0.75$, while the contribution from the Fe is still rather strong.

To further demonstrate the correlation between the MAE and the orbital moment anisotropy, we show in Fig. 9, the MAE as a function of orbital moment anisotropy for all individual configurations with different values of the chemical order parameter. Only the orbital moment anisotropy obtained from the Fe atoms is shown, here. There is a clear linear correlation between the two quantities, indicated also by the least mean square fit to all data points (solid black line). On the other hand, there can also be a noticeable spread in the linear relationship between the MAE and the orbital moment anisotropy on the level of the individual configurations. Nevertheless, our results suggest that the orbital moment anisotropy can in principle be used as proxy for the MAE, which then allows to analyze how the local environment affects both quantities.

IV. SUMMARY AND CONCLUSIONS

In summary, we have demonstrated a strong coupling between chemical and magnetic orders in $L1_0$ FeNi, consistent with previous studies employing effective medium/mean-field type approaches to describe the compositional disorder. Specifically, our results show that chemical disorder reduces the energy difference between the ferromagnetic and paramagnetic state by about 40 %. Consequently, the magnetic Curie temperature of the disordered system is much lower than the rather high (hypothetical) Curie temperature of the ordered phase. As a result, the magnetic order vanishes once the system starts to disorder under heating, as has been observed in various experiments [14, 39]. On the other hand, perfect ferromagnetic order increases the energy gain due to chemical order by nearly a factor of three compared to the paramagnetic case. In principle, this implies, that if it would somehow be possible to stabilize the ferromagnetic state at higher temperatures, one could artificially increase the order-disorder transition temperature, which could then ease the synthesis of the ordered material. While our simple energetic model is obviously too crude to obtain very accurate values for the order-disorder transition temperature, the estimates we obtain from our Monte Carlo simulations give the correct order of magnitude, indicating that our DFT calculations correctly describe the underlying energetics.

Most importantly, our calculations of the magneto-crystalline anisotropy (MAE) as function of the chemical long-range order parameter P_z reveal that a reduction of P_z by 25 % does not decrease the MAE within the accuracy of our method. This is rather encouraging, since it shows that full chemical order is not required to obtain full anisotropy. However, it also indicates that previous estimates of the full anisotropy, based on the extrapolation of results obtained for partially ordered samples, are probably too high. We note that in order to obtain this result, the use of our configurational sampling method is crucial. Effective medium approaches, such as CPA, do not take into account the specific local chemical environment and thus will always predict a gradual decrease of the MAE for reduced chemical order.

Interestingly, we obtain the highest MAE for certain configurations with partial disorder, which suggests that the MAE can potentially be increased beyond the value obtained for the perfectly ordered $L1_0$ structure. We also demonstrate a clear correlation between the orbital magnetic moment anisotropy and the MAE, which suggests that chemical environments resulting in a large local orbital moment anisotropy will also be favorable for obtaining a high MAE. While it might be highly non-trivial to engineer a specific partially disordered configuration, it provides an exciting avenue to optimize the MAE in tetrataenite with respect to the local chemical environment, by considering small deviations from perfect $L1_0$ order as well as from the ideal equiatomic stoichiometry.

ACKNOWLEDGMENTS

[1] K. Strnat, G. Hoffer, J. Olson, W. Ostertag, and J. J. Becker, Journal of Applied Physics **38**, 1001 (1967).

[2] G. Hoffer and K. Strnat, Journal of Applied Physics **38**, 1377 (1967).

[3] J. F. Herbst, Reviews of Modern Physics **63**, 819 (1991).

[4] K. S. Stegen, Energy Policy **79**, 1 (2015).

[5] R. McCallum, L. Lewis, R. Skomski, M. Kramer, and I. Anderson, Annual Review of Materials Research **44**, 451 (2014).

[6] J. F. Albertsen, J. M. Knudsen, and G. B. Jensen, Nature **273**, 453 (1978).

[7] J. Petersen, M. Aydin, and J. Knudsen, Physics Letters A **62**, 192 (1977).

[8] J. Danon, R. B. Scorzelli, I. S. Azevedo, and M. Christophe-Michel-Lévy, Nature **281**, 469 (1979).

[9] J. Danon, R. B. Scorzelli, I. Souza-Azevedo, J. Laugier, and A. Chamberod, Nature **284**, 537 (1980).

[10] R. S. Clarke and E. R. D. Scott, American Mineralogist **65**, 624 (1980).

[11] J. Paulevé, A. Chamberod, K. Krebs, and A. Bourret, Journal of Applied Physics **39**, 989 (1968).

[12] T. Kojima, M. Ogiwara, M. Mizuguchi, M. Kotsugi, T. Koganezawa, T. Ohtsuki, T.-Y. Tashiro, and K. Takanashi, Journal of Physics: Condensed Matter **26**, 064207 (2014).

[13] L. H. Lewis, A. Mubarok, E. Poirier, N. Bordeaux, P. Manchanda, A. Kashyap, R. Skomski, J. Goldstein, F. E. Pinkerton, R. K. Mishra, R. C. K. Jr, and K. Barmak, Journal of Physics: Condensed Matter **26**, 064213 (2014).

[14] L. H. Lewis, F. E. Pinkerton, N. Bordeaux, A. Mubarok, E. Poirier, J. I. Goldstein, R. Skomski, and K. Barmak, IEEE Magnetics Letters **5**, 1 (2014).

[15] L. Néel, J. Pauleve, R. Pauthenet, J. Laugier, and D. Dautreppe, Journal of Applied Physics **35**, 873 (1964).

[16] R. B. Scorzelli, Hyperfine Interact. **110**, 143 (1997).

[17] F. Takata, K. Ito, and T. Suemasu, Japanese Journal of Applied Physics **57**, 058004 (2018).

[18] T. Shima, M. Okamura, S. Mitani, and K. Takanashi, Journal of Magnetism and Magnetic Materials **310**, 2213 (2007).

[19] A. Makino, P. Sharma, K. Sato, A. Takeuchi, Y. Zhang, and K. Takenaka, Scientific Reports **5**, 16627 (2015).

[20] S. Goto, H. Kura, E. Watanabe, Y. Hayashi, H. Yanagihara, Y. Shimada, M. Mizuguchi, K. Takanashi, and E. Kita, Scientific Reports **7**, 13216 (2017).

[21] M.-Z. Dang and D. G. Rancourt, Physical Review B **53**, 2291 (1996).

MAGNETO-CRYSTALLINE ANISOTROPY ENERGY IN L1$_0$-FENI

In the previous chapter, we demonstrated that in L1$_0$-FeNi, both magnetic and chemical orders are strongly coupled to each other. We also showed that the MAE for a few randomly created partially disordered configurations is higher than the MAE for the fully ordered configuration. This indicates the possibility of further optimizing the MAE in this system by optimizing the distribution and the composition of the constituent elements. In this chapter, we present our analysis on the correlation between the orbital moment anisotropy and the MAE, in order to find ways to further increase the MAE in FeNi beyond that of the fully ordered equiatomic structure.

4.1 MOTIVATION

As discussed in the previous chapter, our MAE calculations as a function of chemical long-range order parameter in L1$_0$-FeNi reveal that the MAE of some of the partially disordered configuration is higher than that of the fully ordered structure. This naturally leads to the question of how the MAE in L1$_0$-FeNi depends on specific local chemical environment and stoichiometry and whether it is possible to further increase the MAE by optimizing the composition and distribution of the constituent elements.

In an experimental study by Kojima *et al.* [77], they investigated the Fe-Ni composition dependence of the MAE in ordered Fe-Ni thin films grown by alternate deposition of Fe and Ni monoatomic layers and found large MAE and saturation magnetization for Fe-rich stoichiometries, in particular, for Fe$_{60}$Ni$_{40}$. Note that, however, the electronic structure calculations employing CPA to model the chemical disorder were not able to confirm this observation of the increase in the MAE for Fe-rich stoichiometries relative to the equiatomic case [74].

In this chapter, we therefore employ supercell technique as described in Sec. 2.6, to model the chemical disorder and analyze how local chemical environment is related to the MAE by using local orbital moment anisotropy as a proxy for the local atomic contribution to the MAE. Based on our analysis, we then optimize the composition and distribution of Fe and Ni to increase the MAE beyond that of the fully ordered FeNi.

4.2 SUMMARY OF RESULTS

As a first step, we analyze the distribution of local OMA for Fe and Ni atoms present in 50 equiatomic configurations with long-range order parameter of 0.75. Fig. 2 of Paper [2] shows the distribution of individual Fe and Ni OMA values. One can see from the figure that the majority of the Fe OMA values are positive and the distribution of the Fe OMA values is rather asymmetric around zero value. On the other hand, the distribution of the OMA values for Ni atoms is symmetric around zero with majority of the values lying close to zero. This shows that the Fe atoms are the majority contributors to the total OMA. Our analysis agrees well with an experimental study by Kotsugi *et al.* [159], where they showed a strong angular dependence for Fe orbital magnetic moments from their magnetic circular dichroism measurements and not for Ni.

We also find that a few of the Fe atoms have OMA values that are as high as $0.015\,\mu_B$. We then analyze the local atomic environment of these Fe atoms and find that they all exhibit an equivalent first-nearest neighbour environment as shown in Fig. 1c of Paper [2]. Within this "favorable environment", each central Fe atom is surrounded by 6 Fe (4 in the same plane and 2 with nearest neighbors to each other either in the plane above or below the central Fe atom) and 6 Ni atoms. We also note that this favorable environment not always leads to high OMA but can also exhibit an OMA values in between $0.006\,\mu_B$ and $0.015\,\mu_B$.

In the next step, we design a new $2 \times 2 \times 2$ supercell of the conventional cubic cell by taking favorable environment as a guide. This leads to a configuration with 20 Fe and 12 Ni atoms with a calculated MAE of 141 μeV/2-atoms which is almost 2 times higher than the MAE of a fully ordered structure. We then create several additional configurations with Fe content varying from 53% to 59%. Fig. 3 of Paper [2] reveals a MAE that is higher for all the configurations where the Fe content is greater than 50%. Note that this already indicates that higher Fe content might be favorable to achieve higher MAE in this system, but before exploring this in more detail, we first perform a systematic "measure" for the chemical environments and a possible correlation with high local OMA.

To investigate the correlation between the local atomic environment of an Fe atom and its OMA, we perform a more detailed analysis by employing the SOAP descriptor as described in Sec. 2.7 which encodes the specified local atomic environment into a rotationally invariant representation. To visualize this correlation, we employ a dimensionality reduction technique, t-SNE, to reduce the high-dimensional SOAP vectors to two dimensions (see Sec. 2.7). In Fig. 4 of Paper [2], we show the reduced SOAP vectors corresponding to different local atomic environments of Fe atoms present in equiatomic configurations with different values of long-range order parameter. We note that a clear correlation

between the OMA and the local chemical environment in such a plot is indicated by the clustering of the data points with the same color. We observe that for configurations with $P_z \geq 0.75$, the correlation between the OMA and the local atomic environments becomes more clear when further neighbors e.g., 2NN and 3NN are included in the analysis. However, for configurations with $P_z = 0.5$, the correlation between the local atomic environment and the OMA becomes less clear and vanishes completely for fully disordered configurations and does not improve even on including second and third-nearest neighbors.

In the next step, we create several configurations with different Fe content by randomly replacing Ni atoms with Fe atoms in a fully ordered configuration. This step is motivated by the observation that the favorable environment contains an Fe-rich stoichiometry relative to the local environment present in a fully ordered configuration. In addition, we also note that such configurations are possible to obtain experimentally e.g., using a layer-by-layer growth methods. From the DFT calculations, we find that the average MAE increases with the increasing Fe content upto the highest considered Fe content of 62.5%. Our results agree well with the experimental study by Kojima *et al.* [77] discussed in previous section. From their analysis, they found that the MAE increases monotonically with long-range order parameter and further showed that increasing Fe content is an effective way to further increase the MAE in L1$_0$-FeNi. Finally, note that we do not increase the Fe-content beyond 62.5% as this will not only lead to a decrease in the degree of order parameter in the system but will also destabilize the ferromagnetic ground state [71, 160].

4.3   IMPLICATIONS AND FURTHER WORK

In conclusion, we present a study on the effects of chemical disorder on the MAE in L1$_0$-FeNi. Our calculations clearly show that the MAE in this system can be increased beyond the MAE of a fully ordered equiatomic structure. The identification of the favorable environment indicating an Fe-rich stoichiometry, allowed us to design an optimized structure with an increased MAE.

Our SOAP analysis indicates that it is unlikely to understand the MAE in FeNi as a sum of local atomic contributions determined by the local chemical environment of the Fe atoms. Thus, a simple model relating the local atomic environment to the MAE might not be applicable. This is consistent with a study by Ke *et al.* [161] where they decomposed the MAE by employing *ab initio* tight-binding framework constructed using Wannier functions, into inter- (two-ion model) and intra-atomic (single-ion model) contributions. They demonstrated that the inter-atomic term is dominant in FeNi which indicates that one needs to go beyond the single-ion model. Therefore, we note that although we are able to successfully design the structures with high MAE

using favorable environment as a guide, Fig. 4 of Paper [2] indicates only a partial correlation between the local orbital moment anisotropy of Fe atoms and its first nearest neighbors.

By performing DFT calculations for structures with varying Fe content, we show that the MAE increases by about 25% for an Fe content of 62.5% relative to the case of a fully ordered equiatomic structure. The study allow to corroborate the experimental study of the compositional dependence of the MAE by Kojima *et al.*. We note that this was not verified by a previous study employing the effective medium approach such as CPA to model the compositional disorder [74]. The authors instead observed the decrease in the MAE by about 10% for a 20% increase in the Fe-content relative to the fully ordered equiatomic structure. Thus, our calculations show that it is important to include the effects beyond CPA present in disordered alloys to understand how chemical disorder affects the key magnetic properties such as the MAE.

4.4   PUBLICATION

This work is available as a preprint as *»Effect of chemical disorder on the magnetic anisotropy in L1$_0$ FeNi from first principles calculations«* on arXiv [2]. I performed initial analysis on the configurations created in the previous chapter and wrote the SOAP and t-SNE analysis described in section III C. All DFT calculations and their evaluation are performed by Mayan Si who worked on this project as a master student under my supervision. I revised the first draft written by Mayan Si, and discussed and corrected together with C. Ederer.

Effect of chemical disorder on the magnetic anisotropy in L1$_0$ FeNi from first principles calculations

Mayan Si, Ankit Izardar, and Claude Ederer[*]

Materials Theory, ETH Zürich, Wolfgang-Pauli-Strasse 27, 8093 Zürich, Switzerland

(Dated: March 25, 2022)

We use first principles calculations to investigate how deviations from perfect chemical order affect the magneto-crystalline anisotropy energy (MAE) in L1$_0$ FeNi. We first analyze the local chemical environment of the Fe atoms in various partially ordered configurations, using the orbital magnetic moment anisotropy (OMA) as proxy for a local contribution to the MAE. We are able to identify a specific nearest neighbor configuration and use this "favorable environment" to successfully design various structures with MAE higher than the perfectly ordered system. However, a systematic analysis of the correlation between local environment and OMA using smooth overlap of atomic positions (SOAP), indicates only a partial correlation, which exists only if the deviation from full chemical order is not too large, whereas in general no such correlation can be identified even using up to third nearest neighbors. Guided by the observation that the identified "favorable environment" implies an Fe-rich composition, we investigate the effect of randomly inserting additional Fe into the nominal Ni planes of the perfectly ordered structure. We find that the MAE increases with Fe content, at least up to 62.5% Fe. Thus, our study shows that the perfectly ordered case is not the one with highest MAE and that an increased MAE can be obtained for slightly Fe-rich compositions.

I. INTRODUCTION

Due to the huge and strongly increasing demand of permanent magnets for, e.g., applications in electrical power generation and conversion, there is great interest in new magnetic materials, in particular those containing cheap and abundant elements with no or only small amounts of rare earth elements [1, 2]. L1$_0$-ordered FeNi is an attractive candidate as *gap magnet*, i.e., a magnet with an expected energy product in between that of cheap ferrite magnets and that of the rather expensive high-performance magnets of the Nd-Fe-B family [3].

The L1$_0$-ordered phase of FeNi was first reported by Néel and coworkers, who irradiated disordered Fe$_{50}$Ni$_{50}$ specimens with neutrons in the presence of magnetic field [4, 5]. Later it was naturally observed in iron meteorite samples [6–10]. The laboratory synthesis of the ordered phase is, however, very challenging because of the rather low order-disorder transition temperature, which is around 320°C [4, 5, 11]. At such temperatures, atomic diffusion is extremely slow, which prevents the formation of the ordered state by conventional annealing techniques on realistic time-scales. Even though the synthesis of fully ordered L1$_0$ FeNi is very challenging, samples with a high degree of chemical order have been prepared in experiments using methods such as, e.g., nitrogen insertion and topotactic extraction [12], the transformation from an amorphous state to a stable crystalline state [13], pulsed laser deposition [14], and molecular beam epitaxy [15].

Due to the difficulty in obtaining fully ordered samples, it is important to understand the effect of partial chemical disorder on the magnetic properties of FeNi, in particular how deviations from equiatomic stoichiometry and perfect chemical order affect the magneto-crystalline anisotropy energy (MAE). Note that deviations from equiatomic stoichiometry will automatically result in a decrease of chemical order. The compositional dependence of the MAE has been studied experimentally in partially ordered Fe-Ni thin films grown by molecular beam epitaxy, and a maximum of the MAE has been found for a composition of 60% Fe [15]. However, an increase of the MAE with increasing Fe content relative to the fully ordered equiatomic case could not be confirmed by electronic structure calculations using the coherent potential approximation [16].

In previous work, we have used first principles calculations within density functional theory (DFT) to investigate the effect of partial chemical disorder on the MAE of equiatomic L1$_0$ FeNi [17]. By considering supercells with different distributions of Fe and Ni atoms over the available lattice sites, we have shown that the average MAE remains nearly constant if deviations from the perfect chemical order are not too large. Even a reduction in the degree of chemical order by about 25% does not lead to a significant reduction of the MAE. This is very promising for the experimental synthesis of L1$_0$ FeNi with high MAE. Furthermore, several (randomly created) configurations with only partial chemical order exhibited a larger MAE than the perfectly ordered case. This raises the question of what factors determine the MAE in L1$_0$ FeNi, how it depends on the specific atomic distribution and composition, and whether the MAE can be further increased by optimizing the distribution of Fe and Ni atoms.

In this article, we analyze the relation between the MAE and the local atomic environment, in order to identify ways to increase the MAE of FeNi beyond that of the perfectly L1$_0$-ordered equiatomic case. Thereby, we use the orbital magnetic moment anisotropy (OMA) as a proxy for a potential local contribution to the MAE. We first analyze 50 equiatomic configurations with 75% chemical order, and identify a local nearest neighbor environment for the Fe atoms that appears to be particularly

favorable for obtaining a high OMA. Using this favorable environment as a guide, we manually construct several new configurations with potentially high MAE and Fe contents between 50% and 62.5%. DFT calculations are then used to confirm the high MAE of these structures.

We then perform a more systematic analysis using *smooth overlap of atomic positions* (SOAP) as descriptors for the local atomic environment [18]. This analysis indicates only a weak correlation between the local OMA and the local environment. Furthermore, this correlation exists only if the underlying structure does not deviate too much from perfect chemical order. This suggest that it is unlikely that the MAE in L1$_0$ FeNi can be understood fully as a sum of local contributions determined by the local environment. We thus refrain from further analyzing the physical origin of the enhanced anisotropy in our specifically designed configurations. Instead, we explore the effect of randomly inserting excess Fe atoms into the Ni planes of the perfectly ordered structure (shown in Fig. 1b). This is motivated by the fact that the previously identified "favorable environment" implies a certain degree of Fe overstoichiometry. We find that, even though the excess Fe decreases the degree of chemical order, the MAE nevertheless increases, at least up to an Fe content of 62.5 %, consistent with previous experimental reports [15]. Our results thus identify a very promising route for optimizing the MAE using experimental layer-by-layer deposition techniques.

In the remainder of this article, we first describe our computational methods and how we model the partial chemical order (Sec. II), before we present the identification of the favorable environment (Sec. III A) and the specifically designed configurations with high MAE (Sec. III B). Sec. III C contains the SOAP analysis and Sec. III D the results for the structures with excess Fe atoms inserted into the Ni planes. Finally, our conclusions are summarized in Sec. IV.

II. COMPUTATIONAL METHOD

A. Modeling of partially ordered structures

To study different configurations with varying composition Fe$_x$Ni$_{1-x}$ with $0.5 \leq x \leq 0.625$, we use a $2 \times 2 \times 2$ supercell of the conventional cubic cell (with lattice constant $a = 3.56$ Å), containing 32 sites of the underlying fcc lattice (see also Ref. 17). We then occupy the lattice sites with Fe and Ni atoms in different ways to create structures with a certain Fe content and degree of order. To characterize the degree of order of a given configuration, we define the three-component long range order parameter P_x, P_y and P_z as follows:

$$
\begin{aligned}
P_x &= \tfrac{1}{2}\left(p_\alpha - p_\beta + p_\gamma - p_\delta\right) \\
P_y &= \tfrac{1}{2}\left(p_\alpha - p_\beta - p_\gamma + p_\delta\right) \\
P_z &= \tfrac{1}{2}\left(p_\alpha + p_\beta - p_\gamma - p_\delta\right)
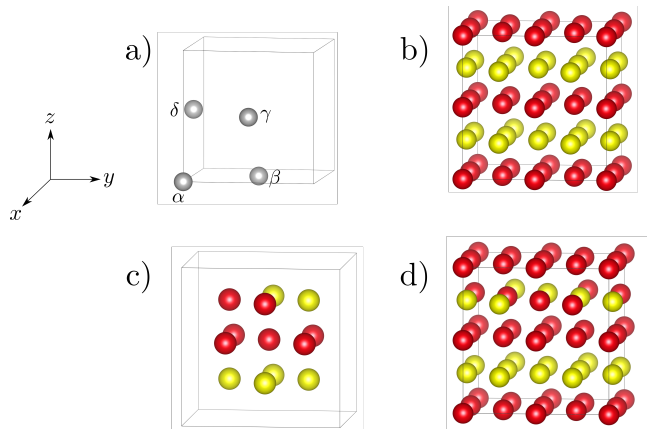\end{aligned}
\tag{1}
$$

FIG. 1. a) Depiction of the four sites of the fcc lattice within the conventional cubic unit cell, defining the four sublattices α, β, γ, and δ used in Eq. (1). b) Perfectly L1$_0$-ordered structure, depicted in a $2 \times 2 \times 2$ supercell relative to the conventional four-atom cubic cell. c) Schematic representation of the "favorable" nearest neighbor environment of Fe atoms with the largest OMA of $0.015\,\mu_{\mathrm{B}}$. d) Specifically designed structure (with composition Fe$_{0.625}$Ni$_{0.375}$) based on this favorable environment. Red and yellow spheres in all subfigures represent Fe and Ni atoms, respectively.

Here, p_i, $i \in \{\alpha, \beta, \gamma, \delta\}$, denote the fraction of sites (or the occupation probabilities in the thermodynamic limit) for each sublattice i that are occupied with Fe, and the different sublattices correspond to the four sites defining the fcc lattice within the conventional cubic cell (see Fig. 1a). The definition in Eq. (1) is consistent with the definition used in our previous work for equiatomic composition [17], where $\sum_i p_i = 2$, but is also applicable to different Fe contents. As can be seen in Fig. 1b, perfect L1$_0$ order consists of (001)-type planes that are alternatingly occupied with either Fe or Ni. Depending on whether these planes are stacked along the x, y, or z direction, the corresponding component of the order parameter becomes non-zero. In the following, we will, without loss of generality, always consider structures where the main component of the order parameter is oriented along the z direction, i.e., $|P_z| \geq 0$, whereas P_x and P_y are either kept to zero or they average out over different configurations with the same P_z.

The MAE is defined as the energy difference for orientation of the magnetization along the order parameter direction (z axis) and perpendicular to it (along either the x or the y direction). Note that for an arbitrary individual configuration, the x and y directions are in general not equivalent. In cases where we are interested in the MAE of an individual configuration, we therefore evaluate the MAE with respect to both x and y directions and then take the average, i.e., MAE $= (\mathrm{MAE}_x + \mathrm{MAE}_y)/2$ with $\mathrm{MAE}_x = E^{[100]} - E^{[001]}$ and $\mathrm{MAE}_y = E^{[010]} - E^{[001]}$. Here, $E^{[100]}$, $E^{[001]}$, and $E^{[010]}$ are the total energies obtained for magnetization aligned along the [100], [001]

and [010] directions, respectively. In cases where we average the MAE over different randomly created structures with the same P_z, we only calculate MAE_x, since the difference between the x and y directions will average out over many configurations. In our definition, a positive MAE indicates that the easy axis is oriented along the order parameter direction, i.e., the [001] direction, which is known to be the case for L1_0 FeNi.

Note that for all configurations considered in this work, we keep the lattice constant and atomic positions fixed to those of an ideal fcc lattice with a c/a ratio of 1.0. This allows to focus on the purely chemical effect related to the distribution of atoms over the available sites, and also significantly reduces the computational effort. Note that small changes in lattice parameters, e.g., resulting from a varying Fe content, are not expected to have a significant effect on the MAE. For example, we have verified that relaxing the c/a ratio for the fully ordered configuration, changes the MAE by only $\sim 2\mu\text{eV}/(2 \text{ atoms})$.

B. Computational details

We calculate the MAE from DFT calculations including spin-orbit coupling, using the Vienna *ab initio* Simulation package (VASP) [19], the projector-augmented wave method (PAW) [20, 21], and the generalized gradient approximation according to Perdew, Burke, and Ernzerhof [22]. To obtain the MAE, we use the magnetic force theorem [23, 24], i.e., we perform non-self-consistent calculations with spin-orbit coupling included, using the charge density converged without spin-orbit coupling, and then take the difference in band energies between the two different orientations of the magnetization direction. Our PAW potentials include $3p$, $4s$, and $3d$ states in the valence for both Fe and Ni. Brillouin zone integrations are performed using the tetrahedron method with Blöchl corrections and a Γ-centered $14 \times 14 \times 14$ **k**-point mesh. The plane wave energy cut-off is set to $350\,\text{eV}$, and the total energy is converged to an accuracy of $10^{-8}\,\text{eV}$. The convergence of the MAE with respect to the **k**-point sampling was tested by performing calculations using up to $25 \times 25 \times 25$ **k**-points. Thereby, the MAE was found to be sufficiently converged for our purposes, to about $\pm 1\,\mu\text{eV}$ per 2 atoms, using a $14 \times 14 \times 14$ **k**-point mesh.

To parametrize the atomic distribution within the local environment around each Fe atom, we use the SOAP descriptor [18] implemented in the DScribe software package [25]. We employ cutoff radii of $2.6\,\text{Å}$, $3.6\,\text{Å}$, and $4.4\,\text{Å}$, corresponding to first nearest neighbor (1NN), second nearest neighbor (2NN), and third nearest neigbor (3NN) environments, respectively. We use a basis of $n_{\max} = 8$ radial and $l_{\max} = 6$ angular functions, and a Gaussian width of $0.5\,\text{Å}$.

We then use t-distributed stochastic neighbor embedding (t-SNE) [26], as implemented in scikit-learn [27], to reduce the high-dimensional SOAP vectors to two dimensions for easier visualization and analysis. This technique generates a low-dimensional map of the original data points in such a way that similar data points are mapped onto points that are close to each other, potentially forming clusters in the low dimensional representation, while dissimilar data points are preferentially mapped onto more distant points. The size of the clusters in the low-dimensional map is strongly influenced by the "perplexity", which can roughly be viewed as a measure for the effective number of nearest neighbor points. We set the perplexity to 6; larger values lead to larger clusters and thus less separation between data points with different OMA, which does not affect our conclusions.

III. RESULTS AND DISCUSSION

A. Local atomic environment of Fe atoms

In our previous work [17], we calculated the MAE for 50 configurations with $P_z = 0.75$ for the equiatomic composition ($\text{Fe}_{0.5}\text{Ni}_{0.5}$). Many of these configurations exhibited a MAE larger than that of the fully ordered structure ($76\ \mu\text{eV}/2$ atoms), with one configuration even exceeding an MAE of $125\,\mu\text{eV}/2$ atoms. This raises the question of what factors determine the MAE in FeNi and how exactly it depends on the specific distribution of Fe and Ni atoms. To address this question, we now assume that the MAE can be understood, at least approximately, as a sum of local contributions that are determined by the local environment of the individual atoms in the system. We then use the OMA, i.e., the difference in the orbital magnetic moment for different orientations of the magnetization relative to the crystal axes, as a proxy for such a local contribution to the MAE. As shown by Bruno and others [28, 29], using a perturbative treatment of the spin-orbit coupling within the tight binding approximation, the MAE is proportional to the OMA under certain conditions. Indeed, previous work on L1_0 FeNi has found a correlation between MAE and the (site-averaged) OMA both for the fully ordered state [30] as well as for varying degrees of order [17] and also showed that the OMA is dominated by the contribution of the Fe atoms.

The latter can also be seen from Fig 2, which shows the distribution of the OMA for the individual Fe and Ni atoms in all 50 configurations with $P_z = 0.75$. Here, we define the OMA as $\Delta L = L^{[001]} - L^{[100]}$, where $L^{[001]}$ and $L^{[100]}$ are the orbital magnetic moments obtained when the total magnetization is oriented along [001] and [100] directions, respectively. We do not consider the [010] direction, since all 50 configurations are designed to have $P_x = P_y = 0$ and thus the anisotropy between the x and y direction is assumed to be small. Note that a positive OMA indicates that the orbital magnetic moment is larger if the magnetization is oriented along the easy axis, i.e., along the [001] direction. The distribution of the OMA for the Fe atoms in Fig. 2 is asymmetric around zero, with the majority of Fe atoms exhibiting a positive OMA. In contrast, the distribution for the Ni
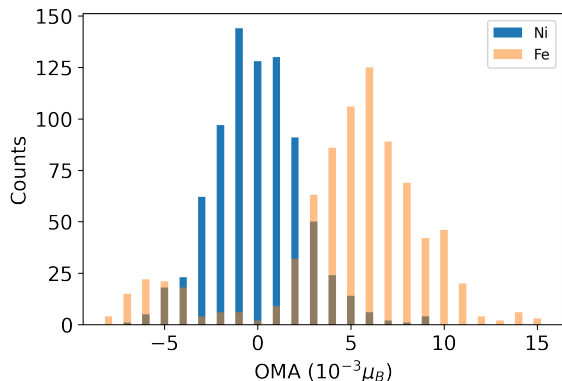
FIG. 2. Distribution of the individual OMA values (in $10^{-3}\mu_B$), obtained for all Fe and Ni atoms included in the 50 equiatomic configurations of FeNi with long range order parameter $P_z = 0.75$.
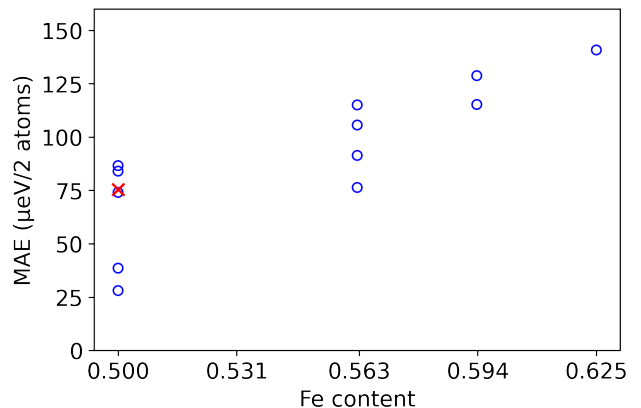

FIG. 3. MAE calculated for different configurations with varying Fe content, obtained by randomly replacing some Fe atoms with Ni starting from the optimized structure with 20 Fe atoms ($x = 0.625$). The red cross represents the MAE of the fully ordered structure.

atoms is rather symmetric, with a peak centered around zero OMA. This confirms that the total OMA is dominated by the Fe contribution, consistent with previous first principles calculations [17, 30], and also magnetic circular dichroism measurements which found a strong angular dependence of the orbital moments for Fe but not for Ni [31]. In the following, we therefore focus on analyzing only the local environment of the Fe atoms.

From Fig. 2, one can also see that a small number of Fe atoms exhibit a particular high OMA of $0.015\,\mu_B$. Analysis of their local atomic environment reveals that all these Fe atoms exhibit an equivalent first nearest neighbor (1NN) environment, which is shown in Fig. 1c. Each central Fe atom is surrounded by six Fe and six Ni atoms, with four Fe atoms in the same x-y plane and the remaining two Fe atoms as nearest neighbors to each other in the plane either above or below the central Fe atom. All other 1NN positions are occupied by Ni atoms. There are also some other Fe atoms in our 50 configurations that have exactly the same (or an equivalent) 1NN environment as depicted in Fig. 1c but exhibit an OMA smaller than 0.015 μ_B. This indicates that the OMA (and thus likely the MAE) is not completely determined by only the 1NN environment, but that further neighbors also play a role (a further analysis of this is presented in Sec. III C). Nevertheless, most Fe atoms with this specific 1NN environment exhibit a OMA higher than that of the fully ordered case (i.e., higher than 0.006 μ_B), and from now on we will therefore refer to this as the "favorable environment".

B. New configurations based on the favorable local environment

Next, we use the favorable environment as a guide to design optimized configurations with potentially high OMA, and thus high MAE. We start with a $2 \times 2 \times 2$ su-

percell of the conventional cubic cell and place Fe atoms at positions $(0, 0, 0)$ and $(0.5, 0.5, 0.5)$. We then arrange Fe and Ni atoms on the corresponding 1NN positions of the two initial Fe atoms according to the favorable environment. The remaining six positions in the supercell are then filled with Fe atoms, thereby maximizing the number of Fe atoms exhibiting the favorable environment. This procedure results in a configuration with 20 Fe and 12 Ni atoms ($x = 0.625$), depicted in Fig. 1d, where 16 Fe atoms exhibit the favorable environment. The corresponding long-range order parameter is $P_x = P_y = 0$ and $P_z = 0.75$. Note that the Fe:Ni ratio on the 12 1NN-sites of the favorable environment is 6:6, whereas it is 4:8 for the fully ordered equiatomic case. This results in an excess Fe content of the specifically designed structure, with 20 Fe and 12 Ni atoms in the unit cell.

We now use DFT to calculate the MAE of this specifically designed structure and obtain a value of 141 $\mu eV/2$ atoms. This value is nearly a factor of two higher than the MAE of 76 $\mu eV/2$ atoms obtained for the perfectly ordered structure. Further analysis shows that the 16 Fe atoms with the favorable environment exhibit an OMA of 0.008 μ_B, consistent with the analysis in Sec. III A. The remaining four Fe atoms have an OMA of only 0.001 μ_B while the 12 Ni atoms exhibit small OMA ranging between -0.002 and $0.003\,\mu_B$. The total OMA of the 32-atom supercell is $0.144\,\mu_B$, which is also much higher than that of the perfectly ordered structure ($0.064\,\mu_B$). It thus appears that optimizing the local 1NN environment of the Fe atoms can indeed lead to configurations with particularly high MAE.

Motivated by this encouraging result, we create additional structures with Fe to Ni ratios of 19:13 ($x = 0.594$), 18:14 ($x = 0.563$), and 16:16 ($x = 0.5$), by starting from the optimized 20:12 structure and then successively replacing one or more Fe atoms by Ni (without further opti-

mization of the local environment). The calculated MAE for these structures as well as or the fully ordered structure are shown in Fig. 3. It can be seen that, compared to the optimized structure with 62.5 % Fe, the MAE decreases with decreasing Fe content while simultaneously the number of Fe atoms exhibiting the favorable environment is reduced to 11 and 8 for $x = 0.594$, and to 6, 8, 6, and 0 for $x = 0.563$ (listed from highest to lowest MAE in each case). However, all structures with Fe content larger than 0.5 exhibit a MAE that is higher than that of the perfectly ordered equiatomic structure. For the equiatomic composition, some structures also exhibit a relatively low MAE, and the number of Fe atoms exhibiting the favorable environment in this case varies between 0 and 4. Thus, the corresponding structures cannot be viewed any more as specifically optimized with respect to the local environment.

Nevertheless, this simple analysis indicates that it is in principle possible to enhance the MAE in L1$_0$ FeNi by moving to slightly Fe rich compositions and optimizing the distribution of Fe and Ni atoms, and confirms our previous result that the perfectly ordered equiatomic state is not the one with the highest MAE. However, in order to obtain guidelines on how to potentially achieve the corresponding structures in an experimental synthesis, a more detailed understanding of the relationship between atomic configuration and the resulting MAE is required.

C. Correlation between OMA and the local chemical environment

To obtain a deeper insight into the correlation between the local atomic environment of an Fe atom and its OMA, it is desirable to have a more systematic and quantitative way to characterize the distribution of atoms within the different local atomic environments. For this purpose, we employ the smooth overlap of atomic positions (SOAP) approach [18], which encodes the local atomic structure around an atom up to a specified cutoff distance in the form of well-defined *descriptors*. The "SOAP vectors" provide a rotationally invariant representation of the different local chemical environments, i.e., an abstract parameterization of the spatial distribution of all atoms up to the cutoff distance, around each site. We generate SOAP vectors corresponding to local atomic environments including up to first-nearest neighbors (1NN), second-nearest neighbors (2NN), and third-nearest neighbors (3NN) for all Fe atoms in the various configurations.

For better analysis and visualization, the high-dimensional SOAP vectors need to be projected into two dimensions in a way that preserves the relative distances between the SOAP vectors as much as possible. Note that the "distances" between different SOAP vectors are a measure of how similar or dissimilar the corresponding chemical environments are. As briefly outlined in Sec. II, we use t-SNE to map each high-dimensional SOAP vector into a two dimensional data-point in such a way that sim-

ilar vectors, i.e. SOAP vectors representing similar local chemical environments, are modeled by data-points that are near to each other, while dissimilar vectors, i.e., vectors representing different local chemical environments, are modeled by points that are far away from each other. Thus, similar atomic environments will form clusters in the low-dimensional representation, while atomic environments that are very different from each other will be separated into different clusters. However, we note that the specific distances between different clusters in the low-dimensional representation are not meaningful, as t-SNE mainly preserves the *local* similarity structure of the data while mapping objects from high to low dimensions.

Fig. 4 shows the t-SNE visualization of the SOAP vectors representing different local atomic environments, including up to 1NN, 2NN, and 3NN, for Fe atoms in different equiatomic configurations with different P_z. For each value of the long range order parameter, 50 configurations have been randomly generated. The x and y axes of the subplots represent the reduced dimensions of the SOAP vectors obtained using the t-SNE technique, while the symbols are colored according to the *absolute value* of the OMA of the corresponding Fe atoms. We note that a potential correlation between the local environment and the local OMA implies that, if two local environments are mapped onto each other by some rotation, then the corresponding anisotropies should be rotated accordingly. We therefore relate only the absolute values of the OMA to the corresponding SOAP vectors. Nevertheless, since we are not evaluating the OMA relative to the y-direction, a data-point with very low OMA in Fig. 4 could still exhibit a strong uniaxial anisotropy along y, which represents a certain limitation of our analysis. However, at least for $P_z = 0.75$, and since $P_x = P_y = 0$ was imposed for all configurations, such cases can be considered as unlikely.

We first consider the case with $P_z \geq 0.75$ with only the 1NN included [Fig. 4(c)]. The zoomed version of Fig. 4(c) shows some examples of the local 1NN environment of the Fe atoms corresponding to selected data points. Case (c1) corresponds to the local atomic environment found in the perfectly ordered structure, while the cluster of yellow and light green triangles denoted as (c2) corresponds to the previously identified "favorable" environment with the highest OMA (see Sec. III A). Note that due to the small truncation error in the SOAP expansion and other numerical inaccuracies, the corresponding data-points are slightly separated in the t-SNE representation, even though they in fact correspond to identical atomic environments. However, we have carefully verified that such small numerical differences in the SOAP vectors do not lead to an artificial separation of equivalent points into different clusters.

For another cluster, (c3), containing only dark blue triangles indicative of a very small OMA, one can see that one of these configurations corresponds to an atomic environment that resembles an Fe atom within a nominal Ni plane, and that the other configuration that is shown indeed exhibits a nearly identical environment, but with
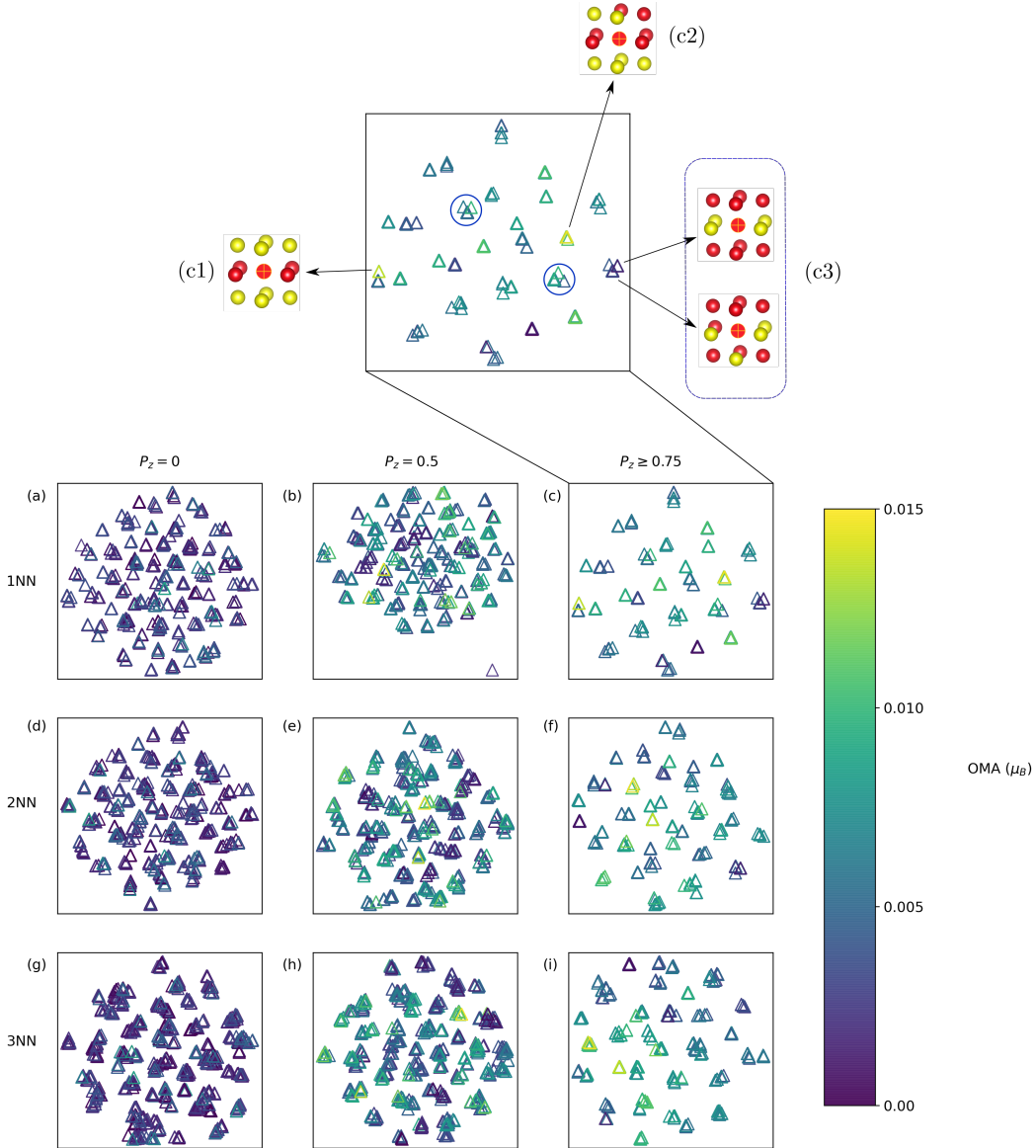
FIG. 4. The t-SNE visualization of the SOAP vectors representing different local chemical environments of Fe atoms including up to 1NN, [(a)-(c)], 2NN [(d)-(f)], and 3NN [(g)-(i)] environments corresponding to configurations with $P_z = 0.0$, $P_z = 0.5$, and $P_z \geq 0.75$. The axes of the subplots represent the reduced dimensions of the SOAP vectors. The color indicates the corresponding absolute value of the OMA. The zoomed version of subplot (c) depicts different local atomic environments (1NN only) corresponding to selected data points.

one Fe-Ni pair exchanged between the lower Fe plane and the nominal Ni plane in the middle.

One can also identify some clusters in Fig. 4(c) that contain a range of colors, indicating Fe atoms with similar 1NN environment but rather different values of the OMA [e.g., the two clusters that are encircled in the zoomed version, or the "cluster" corresponding to the favorable environment (c2)].

On including further neighbors into the local atomic environment, up to 2NN (Fig. 4(f)) and 3NN (Fig. 4(i)), the coloring of data points within individual clusters (and

thus the correlation between OMA and atomic environment) seems to become more consistent. However, the correlation is still not perfect. This indicates that one certainly needs to go beyond 1NN (and perhaps even beyond 3NN) to establish a clear correlation between a specific atomic environment and the corresponding OMA of the central Fe atom.

For configurations with $P_z = 0.5$, one can see that the correlation between the local atomic environment of the Fe atoms and their OMA becomes even weaker, even when including up to 3NN [indicated by several clusters

containing both light green and dark blue triangles in Fig. 4(h)].

For $P_z = 0.0$ [Fig. 4(a), (d), and (g)], the picture is less clear, since there are only few data points with a large OMA. However, it seems that many clusters contain the full spectrum of available OMA values (from dark blue to light green), with no systematic improvement on including further neighbors in the atomic environment.

We conclude that in general (i.e., independent of the global configuration and the resulting value of the long range order parameter P_z) the OMA is not uniquely determined by the local environment, even if including up to 3NN. It is therefore unlikely that the MAE of partially ordered FeNi can be efficiently described by a simple model based on a sum of local contributions determined mainly by the local environment of the Fe atoms. This seems also consistent with Ref. 32, where the MAE of fully ordered L1$_0$ FeNi was decomposed in inter- and intra-atomic contributions using Wannier functions, and it was found that the inter-atomic term is dominant, questioning the applicability of a single ion model of the MAE for FeNi.

Thus, even though the manual identification of the "favorable environment" has allowed to successfully design configurations with high MAE in Sec. III B, the analysis in Fig. 4 shows that there is only a partial correlation between OMA and the 1NN environment. Furthermore, even if considering up to 3NN, this partial correlation seems to only hold for $P_z \geq 0.75$, i.e., when a high degree of chemical order (and our limited supercell size) introduces an implicit constraint on the available further neighbor configurations.

D. Perfectly ordered structure doped with excess Fe

The SOAP analysis in Sec. III C shows that it is unlikely that the MAE in FeNi can be understood within a simple model based on the local atomic environment of individual atoms. Furthermore, even if such a simple model could explain the high MAE of our specifically designed structure based on the favorable environment in Sec. III B, it would be virtually impossible to synthesize the corresponding structure experimentally. Here, we therefore pursue a different route to further optimize the MAE in FeNi. It is based on the observation that the favorable environment implies an excess Fe content compared to the perfectly ordered equiatomic case, and that the specifically designed structure with high MAE shown in Fig. 1(d) essentially corresponds to the perfectly ordered case, but with some additional Fe atoms located in the nominal Ni planes. In the following, we therefore investigate how a random introduction of excess Fe atoms into the nominal Ni planes affect the MAE. Such configurations could be obtained experimentally either by using layer-by-layer growth methods, or by maximizing the chemical order parameter in a structure with slightly
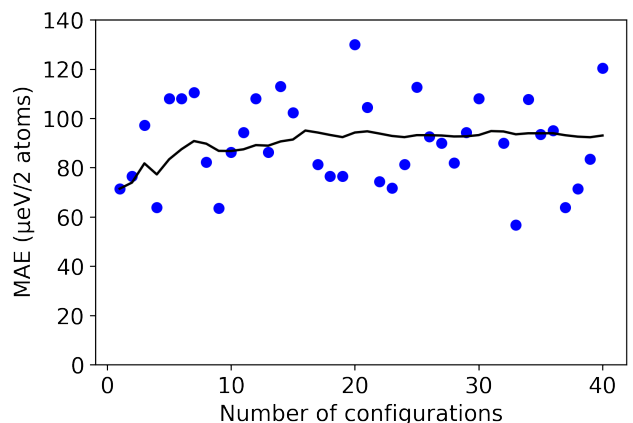
FIG. 5. Calculated MAE values for 40 random configurations with composition belonging to Fe$_{0.625}$Ni$_{0.375}$ and a maximum long-range order parameter of $P_z = 0.75$ (blue dots). The cumulative average is shown by the solid black line.

more than $50\,\%$ Fe content.

We create configurations corresponding to different stoichiometries by randomly replacing Ni atoms with Fe starting from the perfectly ordered structure, i.e., we keep $p_\alpha = p_\beta = 1$ in Eq. (1), whereas p_γ and p_δ become nonzero, such that $\sum_i p_i = 4x$, according to the given stoichiometry. Note that this automatically leads to the highest possible value of the long range order parameter, $P_z = 2(1 - x)$, achievable for a specific Fe content with $x > 0.5$. We consider up to $62.5\,\%$ Fe, which corresponds to 20 Fe atoms within our 32 atom supercell.

For compositions $x = 0.531$, $x = 0.563$, and $x = 0.594$, corresponding to 17, 18, and 19 Fe atoms within the supercell, we create all possible configurations and then use XtalComp [33] to identify symmetry-equivalent structures. For these three specific stoichiometries, we find 1, 7, and 12 distinct groups of equivalent structures within the 32-atom supercell. We then calculate the MAE as average over MAE$_x$ and MAE$_y$ of one representative structure for each distinct group, and evaluate the average over all groups by considering the correct multiplicities. For $x = 0.625$, i.e., 20 Fe atoms in the supercell, the number of possible configuration becomes very high and we therefore do not perform a full symmetry analysis of equivalent structures. Instead, we sample the MAE for 40 randomly created configurations. Fig. 5 shows the evolution of the cumulative average of the MAE for an increasing number of sampled configurations. One can see that the cumulative average converges to a constant value after about 30-40 configurations, which shows that we average over a sufficient number of configurations.

Fig. 6 shows the resulting MAE as a function of Fe content. The corresponding reduction of the long range order parameter P_z is also indicated. Remarkably, the average MAE continuously increases with increasing Fe content, at least up to the highest considered Fe content of $62.5\,\%$. For this case the average MAE is $93\,\mu$eV/2
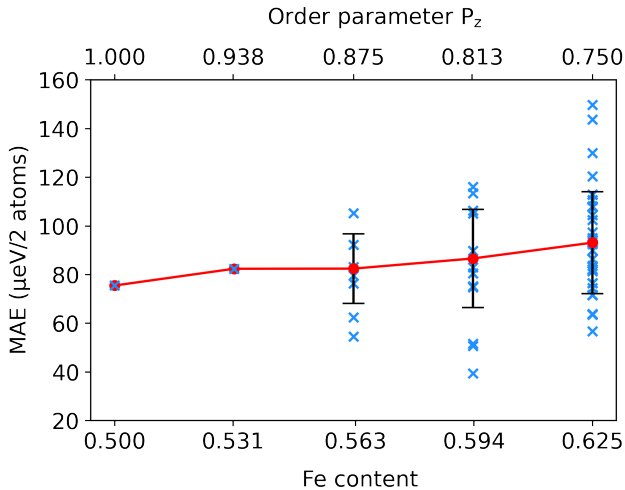
FIG. 6. Calculated MAE as function of Fe content obtained by randomly replacing Ni atoms with Fe, starting from the perfectly ordered case. The corresponding reduction of the long range order parameter P_z is indicated on the upper horizontal axis. The MAE values of the individual configurations for each Fe content are indicated by blue crosses, with the corresponding standard deviation marked by the black vertical bars. Corresponding average values are shown as connected red dots.

atoms, which corresponds to a $23\,\%$ increase compared to the fully ordered equiatomic case. Thus, it appears that the MAE of L1$_0$ FeNi can be increased by considering Fe-rich stoichiometries as long as the degree of chemical order can be kept high. This is consistent with the experimental results obtained by Kotsugi *et al.* [15], even though in their case the degree of chemical order was significantly lower than in our calculations. We note that, for increasing Fe content, it will likely become significantly more difficult to maintain a high degree of chemical order in the system, and thus we do not consider Fe concentrations higher than $62.5\,\%$. Furthermore, the ferromagnetic ground state becomes more and more unstable towards the Fe-rich side, in favor of noncollinear antiferromagnetic or spin-spiral-type ordering (see, e.g., [34, 35]).

IV. SUMMARY AND CONCLUSIONS

In summary, we have investigated the effect of chemical disorder on the MAE in L1$_0$-ordered FeNi using first prin-

ciples DFT calculations. Our calculations clearly show that the perfectly ordered equiatomic configuration is not the one with the highest MAE in this system. By analyzing the local OMA in a number of configurations with reduced chemical order, we were able to identify an apparently favorable 1NN environment, which then allowed us to design an optimized configuration with $62.5\,\%$ Fe content and a MAE nearly twice that of the fully ordered case.

However, further analysis using SOAP as descriptor for the local atomic environment, indicates that a purely local model might not be applicable for the MAE in FeNi, and thus developing a detailed understanding of how the MAE depends on the specific distribution of Fe and Ni atoms is rather challenging.

Nevertheless, our identification of the favorable environment implies that an increase of the MAE in partially ordered FeNi might be possible by inserting additional Fe atoms into the nominal Ni planes of the L1$_0$ structure. Indeed, our corresponding DFT calculations confirm an increase of the MAE by nearly $25\,\%$ compared to the fully ordered case for an Fe content of 0.625. We note that our analysis presented in Fig. 2 and also in our previous work, Ref. 17, indicates that the dominant contribution to the total OMA, and probably also to the MAE, stems from the Fe atoms. It therefore appears that incorporating more Fe atoms into the system can potentially increase the MAE as long as the degree of chemical order can be kept sufficiently high. Thus, our results suggest a realistic route for optimizing the MAE in L1$_0$ FeNi using, e.g., layer-by-layer growth methods that allow to incorporate excess Fe atoms while keeping the degree of order as high as possible.

* claude.ederer@mat.ethz.ch
[1] O. Gutfleisch, M. A. Willard, E. Brück, C. H. Chen, S. G. Sankar, and J. P. Liu, Advanced Materials 23, 821 (2011).

[2] F. Ronning and S. Bader, Journal of Physics: Condensed Matter 26, 060301 (2014).
[3] J. Coey, Scripta Materialia 67, 524 (2012).
[4] Paulevé, J., Dautreppe, D., Laugier, J., and Néel, L., J.

Phys. Radium **23**, 841 (1962).

[5] L. Néel, J. Pauleve, R. Pauthenet, J. Laugier, and D. Dautreppe, Journal of Applied Physics **35**, 873 (1964).

[6] J. Petersen, M. Aydin, and J. Knudsen, Physics Letters A **62**, 192 (1977).

[7] J. F. Albertsen, J. M. Knudsen, and G. B. Jensen, Nature **273**, 453 (1978).

[8] J. Danon, R. B. Scorzelli, I. S. Azevedo, and M. Christophe-Michel-Lévy, Nature **281**, 469 (1979).

[9] J. Danon, R. B. Scorzelli, I. Souza-Azevedo, J. Laugier, and A. Chamberod, Nature **284**, 537 (1980).

[10] R. S. Clarke and E. R. D. Scott, American Mineralogist **65**, 624 (1980).

[11] K. B. Reuter, D. B. Williams, and J. I. Goldstein, Metallurgical Transactions A **20**, 711 (1989).

[12] S. Goto, H. Kura, E. Watanabe, Y. Hayashi, H. Yanagihara, Y. Shimada, M. Mizuguchi, K. Takanashi, and E. Kita, Scientific Reports **7** (2017).

[13] A. Makino, P. Sharma, K. Sato, A. Takeuchi, Y. Zhang, and K. Takenaka", Scientific Reports **5** (2015).

[14] M. Saito, H. Ito, Y. Suzuki, M. Mizuguchi, T. Koganezawa, T. Miyamachi, F. Komori, K. Takanashi, and M. Kotsugi, Applied Physics Letters **114**, 072404 (2019).

[15] T. Kojima, M. Ogiwara, M. Mizuguchi, M. Kotsugi, T. Koganezawa, T. Ohtsuki, T.-Y. Tashiro, and K. Takanashi, Journal of Physics: Condensed Matter **26**, 064207 (2014).

[16] A. Edström, J. Chico, A. Jakobsson, A. Bergman, and J. Rusz, Physical Review B **90**, 014402 (2014).

[17] A. Izardar and C. Ederer, Phys. Rev. Materials **4**, 054418 (2020).

[18] A. P. Bartók, R. Kondor, and G. Csányi, Phys. Rev. B **87**, 184115 (2013).

[19] G. Kresse and J. Furthmüller, Physical Review B **54**, 11169 (1996).

[20] P. E. Blöchl, Physical Review B **50**, 17953 (1994).

[21] G. Kresse and D. Joubert, Physical Review B **59**, 1758 (1999).

[22] J. P. Perdew, K. Burke, and M. Ernzerhof, Physical Review Letters **77**, 3865 (1996).

[23] M. Weinert, R. E. Watson, and J. W. Davenport, Physical Review B **32**, 2115 (1985).

[24] G. H. O. Daalderop, P. J. Kelly, and M. F. H. Schuurmans, Physical Review B **41**, 11919 (1990).

[25] L. Himanen, M. O. Jäger, E. V. Morooka, F. Federici Canova, Y. S. Ranawat, D. Z. Gao, P. Rinke, and A. S. Foster, Computer Physics Communications **247**, 106949 (2020).

[26] L. van der Maaten and G. Hinton, Journal of Machine Learning Research **9**, 2579 (2008).

[27] F. Pedregosa, G. Varoquaux, A. Gramfort, V. Michel, B. Thirion, O. Grisel, M. Blondel, P. Prettenhofer, R. Weiss, V. Dubourg, J. Vanderplas, A. Passos, D. Cournapeau, M. Brucher, M. Perrot, and E. Duchesnay, Journal of Machine Learning Research **12**, 2825 (2011).

[28] P. Bruno, Phys. Rev. B **39**, 865 (1989).

[29] G. v. d. Laan, Journal of Physics: Condensed Matter **10**, 3239 (1998).

[30] Y. Miura, S. Ozaki, Y. Kuwahara, M. Tsujikawa, K. Abe, and M. Shirai, Journal of Physics: Condensed Matter **25**, 106005 (2013).

[31] M. Kotsugi, M. Mizuguchi, S. Sekiya, M. Mizumaki, T. Kojima, T. Nakamura, H. Osawa, K. Kodama, T. Ohtsuki, T. Ohkochi, *et al.*, Journal of magnetism and magnetic materials **326**, 235 (2013).

[32] L. Ke, Physical Review B **99**, 054418 (2019).

[33] D. C. Lonie and E. Zurek, Computer Physics Communications **183**, 690 (2012).

[34] I. A. Abrikosov, A. E. Kissavos, F. Liot, B. Alling, S. I. Simak, O. Peil, and A. V. Ruban, Physical Review B **76**, 014434 (2007).

[35] M. Y. Lavrentiev, J. S. Wróbel, D. Nguyen-Manh, and S. L. Dudarev, Physical Chemistry Chemical Physics **16**, 16049 (2014).

In this chapter, we investigate the effect of $+U$ which incorporates second Hund's rule, on the magnetic properties in L1$_0$-FeNi by employing DFT$+U$ calculations.

5.1 MOTIVATION

In Section 3.3, we discussed that our calculated MAE for chemical long-range order parameter $P_z = 0.5$ is lower as compared to the value obtained experimentally in Ref. [69]. Indeed, it is well known that orbital magnetic moments are typically underestimated due to the absence of any mechanism establishing Hund's second rule in LDA, GGA, etc. Since orbital magnetic moments (and their anisotropy) are closely related to the MAE, as a result, this also leads to the underestimation of the MAE. To circumvent this, one can apply an empirical correction known as orbital polarization correction which has often been used in the past [73, 157, 158]. Both Solovyev *et al.* [112] and Bultmark *et al.* [113], showed that this empirical correction is included in the much more general DFT$+U$ method, where $+U$ is essentially the electron-electron interaction in an atomic d-orbital.

In a study by Shick *et al.* [162], they showed that the effects related to the electron-electron interaction in the ordered transition metal alloys (L1$_0$-CoPt and L1$_0$-FePt) that are not well described in the standard LDA/GGA functionals, tend to strongly affect the orbital magnetic moments and the MAE, and that employing DFT$+U$ calculations can lead to an increase in the calculated MAE.

In another study by Yang *et al.* [163], they showed that by taking into account the effects due to the electron-electron interactions in Fe and Ni, the experimental value of the MAE was correctly predicted near $U = 1.2\,\text{eV}$ $J = 0.8\,\text{eV}$ for Fe and $U = 1.9\,\text{eV}$ $J = 1.2\,\text{eV}$ for Ni.

In the following, we therefore employ DFT$+U$ calculations to investigate the effects of electron-electron interactions on the magnetic properties in L1$_0$-FeNi. As described in Section. 2.2, we use a rotationally invariant form of DFT$+U$ [110] as implemented in VASP. To calculate the MAE, we perform self-consistent calculations with spin-orbit coupling included, and then take the difference in the total energies between the two different orientations of the magnetization direction. We do not employ magnetic force theorem to calculate the MAE since the use of DFT$+U$ with the force theorem is rather questionable [164]. All calculations are performed for a 4-atom conventional cubic fcc cell with 2 Fe and 2 Ni atoms with lattice constant $a = 3.56\,\text{Å}$ and $c/a = 1$.

In the following, we describe our results on the effect of varying U and J values on key magnetic properties in L1$_0$-FeNi. For simplicity, we always apply the same U upto 2 eV and $J \leq U$ to both Fe and Ni.

5.2 RESULTS
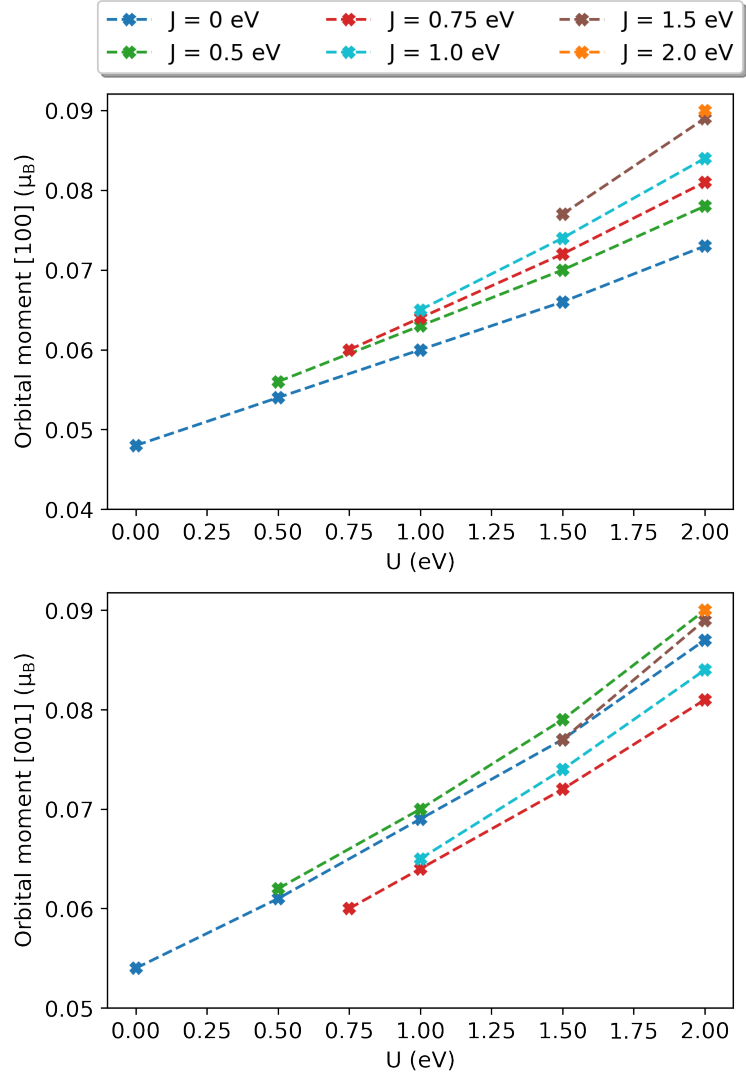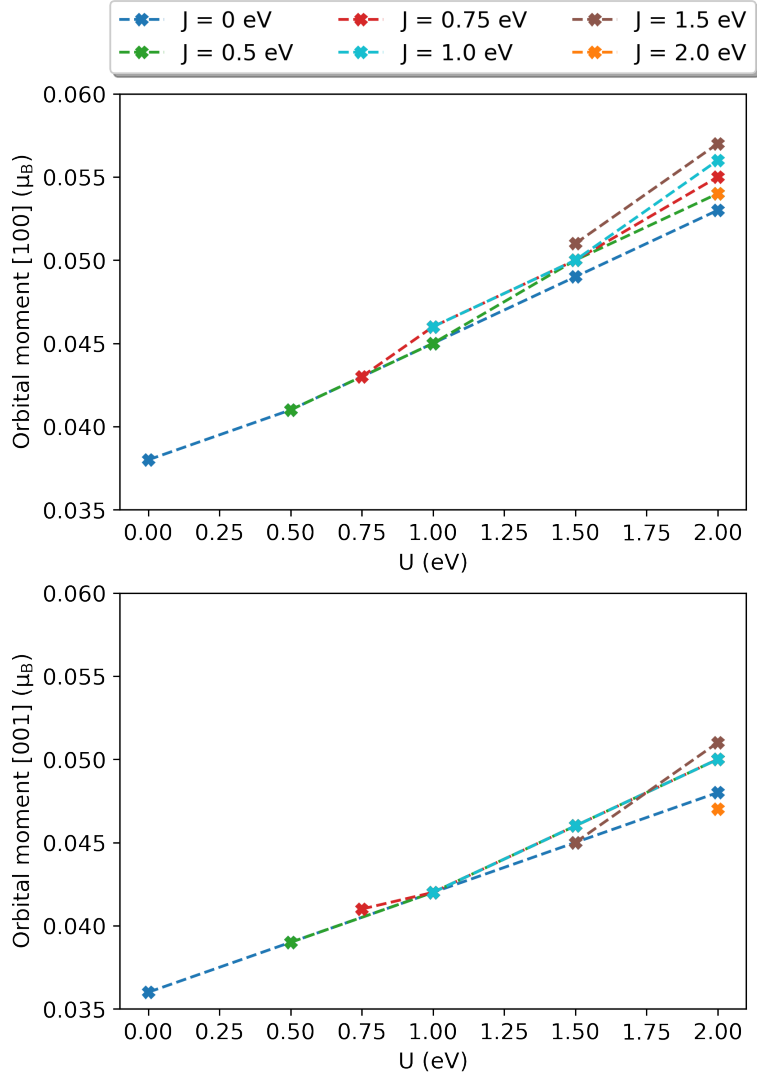

Figure 9: Orbital magnetic moment of Fe for magnetization along [100] (top) and [001] (bottom) present in L1$_0$-ordered FeNi as a function U and J values.

U AND J DEPENDENCE ON ORBITAL MAGNETIC MOMENTS
First, we investigate the effect of U and J on the orbital magnetic moments in L1$_0$-FeNi. The calculated orbital magnetic moments for both Fe and Ni as a function of U and J are shown in Fig. 9 and Fig. 10, respectively. One can see in both figures, that for a fixed value

Figure 10: Orbital magnetic moment of Ni for magnetization along [100] (top) and [001] (bottom) present in L1$_0$-ordered FeNi as a function U and J values.

of J, increasing U results in increasing orbital magnetic moments of both Fe and Ni. Moreover, it can also be seen that for a constant value of U, no systematic trend with respect to increasing J can be seen except for one case (orbital magnetic moments of Fe along [100]). We also note that for Ni, effect of increasing J is rather small. Furthermore, we note that varying U has a larger effect on the magnitude of orbital magnetic moments of both Fe and Ni, as compared to the effect due to the variation in J. Thus, our calculations indicate that taking into account $+U$ correction indeed leads to an increase in the orbital magnetic moments as expected. Note that this observation is similar with the more empirical orbital polarization correction which also results in the increased orbital magnetic moments.
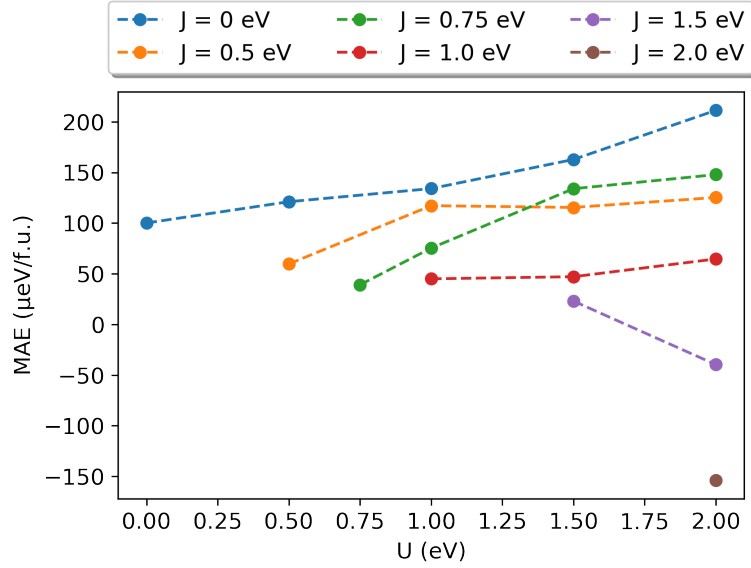
Figure 11: MAE as a function of different U and J values in L1$_0$-FeNi obtained from DFT$+U$ calculations.

U AND J DEPENDENCE ON THE MAE   Fig. 11 shows the dependence of the MAE in L1$_0$-FeNi on U and J values. First, we set $U = J = 0$ eV, and find the calculated MAE $= 100 \, \mu$eV/f.u. obtained using the self-consistent approach. Note that the MAE for the fully ordered FeNi obtained by employing the magnetic force theorem in Paper [1] is a bit lower ($75 \, \mu$eV/f.u.), resulting in a deviation of $25 \, \mu$eV/f.u. as compared to the MAE obtained using SC approach. We note that although magnetic force theorem often gives good estimate of the self-consistent MAE value, deviations in the MAE values are known to occur. In a study by Blanco-Rey $et\ al.$ [122], they calculated the MAE values for several transition-metal alloys FeX (X=Co, Cu, Pd, Pt, and Au) using SC approach and the MFT. For instance, in bulk L1$_0$-FeCo, they found a deviation of $160 \, \mu$eV/f.u. in the MAE calculated using the SC and MFT approach (MAE$_{\mathrm{SC}} = 390 \, \mu$eV/f.u., MAE$_{\mathrm{MFT}} = 550 \, \mu$eV/f.u.). In L1$_0$-FeNi, we assume that the relative differences, e.g., variations of the MAE (calculated using the MFT method) with chemical long-range order and/or Fe-content, are meaningful.

For a fixed value of $J = 0$ eV, the MAE increases with increasing value of U and reaches to about 200 μeV/f.u for $U = 2$ eV and $J = 0$ eV, which is twice the value as compared to the case where $U = 0$ eV. Note that this observation is consistent with a study by Ravindran $et\ al.$ [157], where they employed the full-potential linear muffin-tin orbital method to calculate the MAE in L1$_0$-FeNi. They showed that the MAE increases by about a factor of 2 when orbital polarization correction is taken into account.

Furthermore, one can see that for a fixed value of U, increasing J results in the reduction of the MAE. In particular, a large reduction

and even a change in sign can be seen for $J \geq 1.5$. Finally, from Fig. 11, we note that for this system, the orbital polarization-like behaviour is seen for $0.5\,\mathrm{eV} \leq U \leq 2.0\,\mathrm{eV}$ and $J \leq 1\,\mathrm{eV}$.

U AND J DEPENDENCE ON OMA   In Chapter 3, we demonstrated that there exists a linear correlation between the MAE and the OMA of Fe atoms. Therefore, we next investigate whether the OMA of Fe atoms follows the same trend as observed for the MAE in Fig. 11. In Fig. 12, we plot Fe OMA as a function of different U and J values. Note that the OMA of Fe is calculated by taking the difference between the orbital magnetic moment values shown in Fig. 9. For a fixed value of $J \leq 1.0\,\mathrm{eV}$, a clear increase in the OMA values of Fe can be seen for increasing U. On the other hand, there seems to be a reduction in the OMA values for increasing J, which is consistent with the trend as observed for the MAE. However, for $J \geq 1.5\,\mathrm{eV}$, the MAE values do not fit this trend. We not that this maybe partially hindered due to the smallness of the OMA values which only differs by $0.001\,\mu_B$.
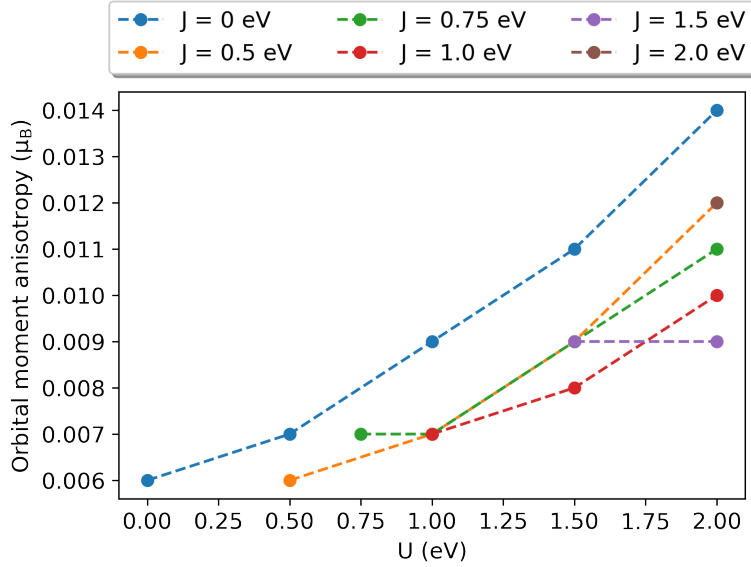
Figure 12: Orbital moment anisotropy of Fe as a function of different U and J values obtained from DFT+U calculations for L1$_0$-FeNi.

5.3 IMPLICATIONS

In conclusion, we demonstrate the effect of incorporating the second Hund's rule on the magnetic properties in L1$_0$-FeNi, by employing DFT+U calculations. Such effects are not captured by the DFT functionals such as PBE, but are well described by taking into account the on-site Coulomb interactions within the DFT+U method. We show that +U can have a significant impact on the orbital magnetic moments and the MAE in L1$_0$-FeNi. A clear increase in the orbital magnetic mo-

ment of both Fe and Ni can be seen with increasing U. Moreover, we find that varying U has a larger effect on the orbital magnetic moment of both Fe and Ni, as compared to the effect due to the variation in J.

Depending on the U and J values, the MAE can either increase or decrease. Moreover, an orbital polarization-like behaviour is only seen for $J \leq 1\,\text{eV}$. Thus, it is likely that the plain PBE underestimates the MAE. Note that this indicates that the orbital polarization correction would result in even further enhancement of the MAE calculated for various Fe-content as discussed in Paper [2]. Finally, we note that the choice of double counting correction could also play a role. However, this aspect still needs to be verified and will be investigated in future work.

5.4 PUBLICATION

The manuscript for this study is currently "under preparation".

MAGNETIC EXCHANGE INTERACTIONS IN L1$_0$-FENI

In Chapter 3 and Chapter 4, we showed that there exists a strong coupling between the chemical and magnetic state in L1$_0$-FeNi and that chemical disorder strongly affects the important magnetic properties such as magnetic anisotropy. In this chapter, we focus on the effect of chemical disorder on the magnetic exchange interactions and consequently, the Curie temperature in L1$_0$-FeNi.

6.1 MOTIVATION

While the Curie temperature of the disordered FeNi system has already been measured in several experimental studies ($T_c \sim 785\,\mathrm{K}$ [165, 166]), the measurement of the Curie temperature of the ordered phase poses a real challenge. The reason for this is that, depending on the heating rate, the ordered FeNi disorders completely upon heating at temperatures above $\sim 700\,\mathrm{K}$, indicating that the disordering in FeNi is a kinetically limited process [63]. Moreover, at the time-scales which are typical for the magnetization measurements, the disordering occurs above the Curie temperature of the disordered phase, resulting in the sudden disappearance of the magnetization [57].

Several previous first principles based studies have calculated the Curie temperature of the ordered FeNi. For example, Edström *et al.* [74] predicted the Curie temperature of the ordered phase to be around 916 K by employing spin-polarized relativistic Korringa-Kohn-Rostocker method. Furthermore, they found a reduction in the transition temperature when chemical disorder was introduced. In another study by Tian *et al.* [167], they calculated by employing exact-muffin-tin orbitals method the Curie temperature of the ordered FeNi to be around 780 K. Moreover, they too observed a reduction in the Curie temperature by around 150 K for the case of chemically disordered system.

It is important to note that both studies employ coherent potential approximation which is an effective medium approach to model the chemical disorder in random alloys [75, 76]. Note that, however, CPA fails to take into account the effects which occur due to the distribution of different atomic species in real disordered alloys. These effects are important to study the impact of chemical disorder on the MAE as shown in chapter 3 and 4, where we found that a slight increase in the Fe-content can lead to an increase in the MAE, an observation that

was not seen by a previous study employing CPA approach to model chemical disorder [74].

In this work, we provide further insights into how the variation in the local chemical environment can affect magnetic exchange interactions and consequently, the Curie temperature in tetrataenite. We follow a similar approach as in previous chapters, i.e., to capture the effect of local chemical environment around an atom, we employ supercell approach to model the chemical disorder. We find that local chemical environment can have significant impact on the magnitude of first nearest neighbour Fe-Fe couplings. This also naturally raises a question of whether there is a correlation between the local chemical environment and the magnetic exchange couplings. However, from our analysis, we did not find any simple relation between these two variables. This as a result also makes it difficult to incorporate the information about the variations of magnetic exchange couplings into a Heisenberg model to obtain T_c. Nevertheless, we try to estimate the effect of such variations by using a simple model with random exchange couplings. From our Monte-Carlo calculations, we find that if one employs local atomic environment-independent "average" magnetic exchange couplings to obtain the Curie temperature of the disordered system, then this would lead to an overestimate of the T_c of a chemically disordered system.

6.2 SUMMARY OF RESULTS

To obtain the magnetic exchange couplings in L1$_0$-FeNi, we employ a method based on the magnetic force theorem [126], where one can obtain J_{ij} values by considering the change in the total energy when magnetic moments are rotated by a very small angle (see Eq. 33 in Sec. 2.4). In order to obtain the quantities in Eq. 33, the DFT Kohn-Sham Hamiltonian is then transformed into a localized Wannier functions basis (see Sec. 2.5). Often, one uses maximally localized Wannier functions (MLWFs) to obtain a unique set of Wannier functions from the Kohn-Sham bands. However, in the FeNi system, this leads to Wannier functions that are not centered on the atoms and, therefore, MLWFs cannot be used in connection with Eq. 33. To circumvent this problem, we refrain from minimizing the quadratic spread and just use "initial projection", which we find all to be atom centered. From our calculations, we find that the resulting Wannier functions for the 2-atom cell of the chemically ordered FeNi are in quite good agreement with all occupied Kohn-Sham bands below ~ 10 eV (see Fig. 1 of Paper [3]).

In the next step, we obtain the magnetic exchange couplings by considering different sets and subsets of Wannier functions to check whether one can obtain a good estimate for the magnetic exchange couplings by constructing fewer WFs corresponding to only a subset of bands (e.g., d bands only). Note that by considering different terms in Eq. 33, one can decompose the magnetic exchange couplings into

different orbital contributions. The calculated couplings are shown in Table II of Paper [3]. We first construct Wannier functions by considering the initial projections of all $s + p + d$ bands and then obtain magnetic exchange couplings by considering (i) all terms in Eq. 33, and (ii) d-only part in Eq. 33. We find that if d-only part is considered, then one obtains a first nearest neighbor magnetic exchange coupling of 29.6 meV which is larger than 27.2 meV when all terms are considered in Eq. 33. This shows that indeed, the main contribution to the magnetic exchange couplings comes from the d orbitals while the s, p, and mixed orbital terms leads to a minor negative contribution. This leads to a question whether it is sufficient to consider d orbitals while constructing Wannier functions to obtain a good estimate for the magnetic exchange couplings. To address this, we construct two more sets of Wannier functions from the d orbitals where in the first set, we obtain Wannier functions by orthonormalized initial projections, and for the second set, we obtain MLWFs by minimization of the quadratic spread functional. The magnetic exchange couplings for the first nearest neighbour Fe-Fe pair is shown in Table II of Paper [3]. From the table, one can see that not only the d-bands but also s and p bands are necessary while constructing Wannier functions and their subsequent use, in obtaining the accurate values of magnetic exchange couplings in L1$_0$-FeNi.

Next, we calculate the magnetic exchange couplings in the fully ordered phase of FeNi and compare with those obtained by Edström *et al.* [74] (see Fig. 2 of Paper [3]). Note that we make this comparison as Wannier-based method, i.e., using Eq. 33 on top of a plane-wave-based DFT method is not so well established and, in particular, the difficulties one encounters to obtain an atom-centered basis, it appears desirable to compare our calculated magnetic exchange couplings with results from a more established method. From our calculations, we find that overall there is a good agreement between our calculated magnetic exchange couplings and those obtained by Edström *et al.*, despite the fact that both methods employ different electronic structure methods which involve different approximations and basis sets.

We then perform Monte-Carlo simulations to investigate the effect of including long-range Fe-Fe couplings on the Curie temperature in ordered FeNi. We find that due to the long-range nature of the Fe-Fe couplings, the Curie temperature shows strong variations when plotted as a function of the Fe-Fe cutoff distance and converges to about 700 K when all Fe-Fe couplings are considered until a distance of around 8 Å. This shows that it is important to consider Fe-Fe interactions upto a very large distance to get an accurate estimate of the T_{c} in this system.

Based on this observation, we then calculate the Curie temperature of the ordered FeNi where we consider calculated magnetic exchange couplings for all pairs, i.e., Fe-Fe, Fe-Ni, and Ni-Ni up to a maximum distance of $10 \cdot a_0$, where a_0 is the equilibrium lattice constant of the
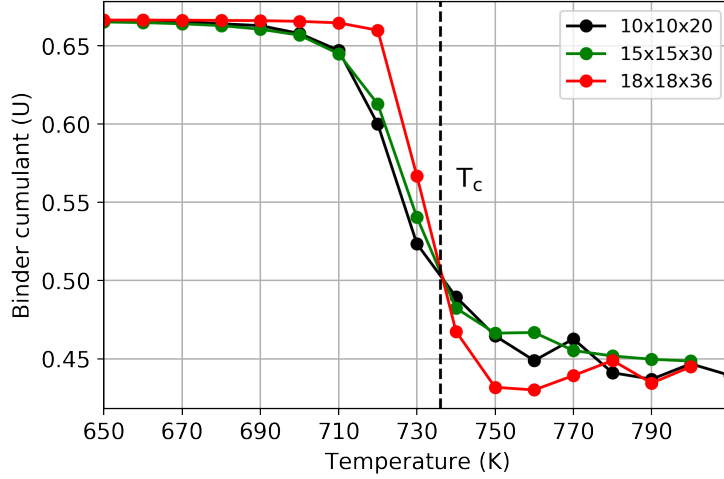
Figure 13: Evaluation of the Curie temperature (T_c) of L1$_0$ FeNi based on the Binder cumulant curves. T_c is obtained by locating the crossing of the curves (shown by a vertical dashed line) obtained by performing Monte-Carlo simulations for three different simulation cell sizes.

ordered FeNi. To obtain an accurate estimate of T_c, we employ Binder cumulant method [151], which allows one to calculate properties in the thermodynamic limit. Within this method, one calculates Binder cumulant (also known as fourth-order cumulant),

$$U = 1 - \frac{\langle m^4 \rangle}{3 \langle m^2 \rangle^2}, \tag{57}$$

where $\langle m^2 \rangle$ and $\langle m^4 \rangle$ corresponds to the second and the fourth moment of the magnetization. U is then plotted as a function of temperature for different system sizes and the critical temperature is obtained by locating the point of intersection of different curves. Fig. 13 shows the Binder cumulant curves for the L1$_0$-FeNi obtained by performing Monte-Carlo simulations for three different simulation cell sizes. From Fig. 13, we obtain a $T_c = 736$ K, which agrees well with the value of 780 K obtained by Tian *et al.* [167]. On the other hand, we note that our calculated T_c is lower than the value of 916 K obtained by Edström *et al.* [74]. We note that this is due to the stronger second nearest-neighbour Fe-Fe and first nearest-neighbour Fe-Ni couplings obtained by Edström *et al.*.

In the next step, we calculate the magnetic exchange couplings in chemically disordered configurations to investigate the effect of chemical disorder on the coupling constants. We create two different partially ordered configurations (see Fig. 4(a) and 4(b) of Paper [3]). The calculated magnetic exchange couplings for first nearest neighbour Fe-Fe pairs are shown in Fig. 5(b) of Paper [3]. From the figure, one can see a large variation in the calculated couplings ranging from 4.7 meV to 36.5 meV. This indicates that chemical disorder can have a signifi-

cant impact on the magnitude of the magnetic exchange couplings in disordered FeNi.

We then study the effect of relaxation of atoms in the supercell on the magnetic exchange couplings and compare the couplings after relaxation with their corresponding values for the unrelaxed case. We find that on an average, relaxation leads to change in the value of couplings by about $2\,\mathrm{meV}$ (see Table I of Paper [3]). However, this change is significantly weaker than the change in the values of couplings due to the different local chemical environments.

Next, we investigate whether the magnitude of the first nearest neighbor Fe-Fe magnetic exchange couplings in Fig. 5(b) of Paper [3] can be correlated to the local chemical environments. From our analysis of the first and first/second nearest neighbours, we do not find any correlation between the magnitude of the magnetic exchange couplings and the chemical distribution around the pair of Fe atoms and conclude that the magnitude of the exchange couplings is affected by effects which are rather long range, as can be expected in itinerant system like FeNi. Note that the dependence of the magnetic exchange couplings on the local environment makes it difficult to incorporate the information about the variations of magnetic exchange couplings into a Heisenberg model to obtain T_c.

Instead, we try to estimate the effect of such variations of the magnetic exchange couplings by using a simple model with random exchange couplings. In our model study, we consider a Heisenberg model with only first nearest neighbour interactions on an fcc lattice. We consider a $15 \times 15 \times 15$ supercell of the conventional 4-atom cubic cell with equivalent sites and then draw random magnetic exchange couplings (equivalent to number of bonds in our supercell) from a Gaussian distribution whose mean value corresponds to the average coupling constant and its standard deviation, σ, represents the local chemical environment-dependent variations in the magnetic exchange couplings.

Note that for each of the $\sigma > 0.0$, we sample 100 random instances of the magnetic exchange couplings and then take the average over all calculated T_c to obtain a sufficiently converged T_c. This can be seen in Fig. 14 where the evolution of the cumulative average of T_c is shown for an increasing number of instances. From the figure, one can also see strong variations in T_c values for a corresponding σ value. This indicates that the cell size is perhaps small to give sufficient "self-averaging", as one would expect from an infinitely large cell. Hence, instead of increasing the cell size, we use a rather efficient method where we sample different random instances, which gives good convergence as shown by the cumulative average that converges to a fixed value after around 80 instances and, thus, shows that the number of instances we sample over are sufficient.

Next, we investigate why such variations in the T_c occurs for different randomly sampled instances with fixed σ. Fig. 15 shows the distribution
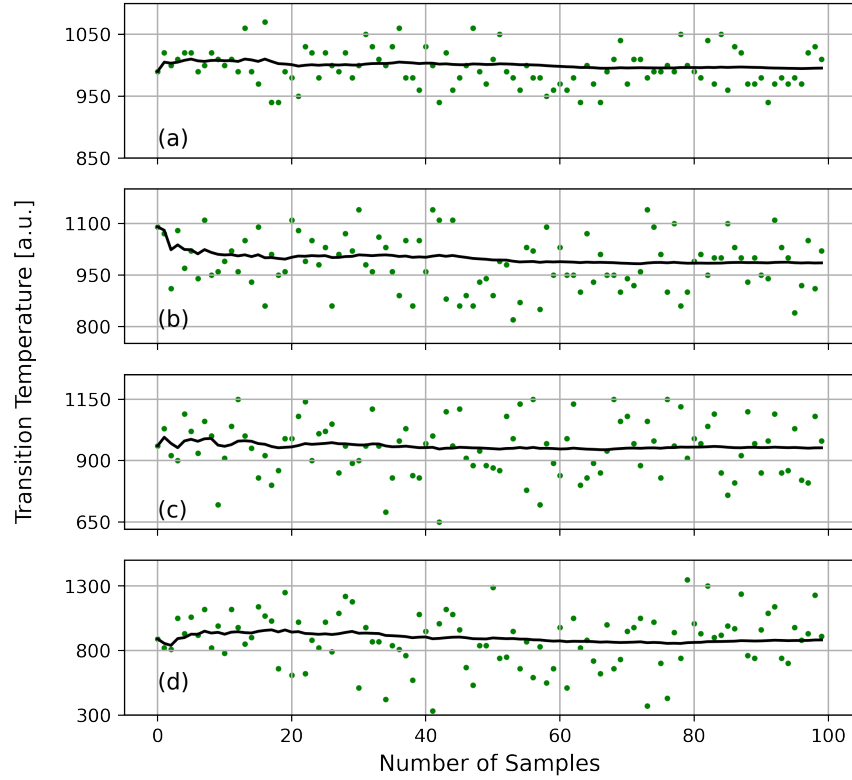
Figure 14: Calculated T_c for 100 random instances (shown by green dots) sampled from a Gaussian distribution with mean = 1 and (a) $\sigma = 0.1$, (b) $\sigma = 0.25$, (c) $\sigma = 0.4$, and (d) $\sigma = 0.6$. The cumulative average is shown by black line in the subplots. Each T_c is obtained by locating the peak value of susceptibility.
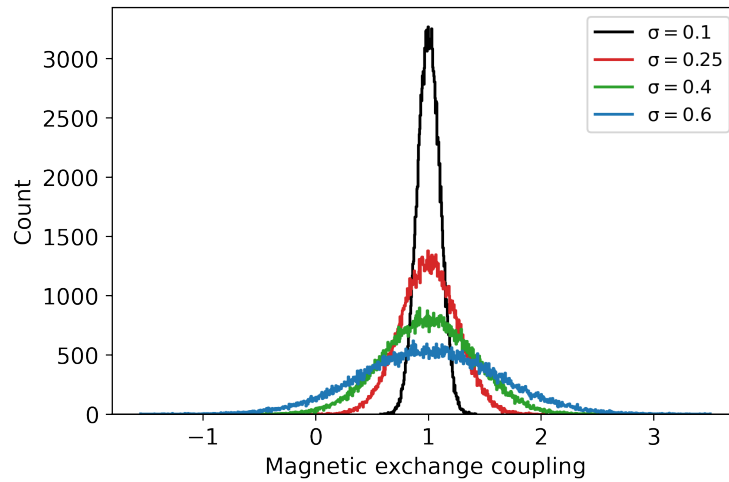

Figure 15: Histogram showing the distribution for one of the instances of randomly sampled magnetic exchange couplings for various σ values. Note that the histograms are normalized such that the total area of each histogram equals 1. For $\sigma = 0.0$, all couplings are identical (not shown here).

of the magnetic exchange couplings for one randomly sampled instance for various σ values. One can see from the figure that the histogram of the couplings for each σ seems to approximate the Gaussian distribution rather well. This indicates that variations in the T_c for fixed σ do not occur due to the small sample size (magnetic exchange couplings) that would result in non-Gaussian distribution. As per our initial test calculations, we attribute these variations to the distribution of the magnetic exchange couplings within the supercell.

Fig. 7 of Paper [3] shows the results of our model study. We find that T_c decreases with increasing σ, i.e., with increasing variation in the magnetic exchange couplings. For $\sigma = 0.6$, which corresponds to the corrected standard deviation of the seven different values of first nearest neighbor Fe-Fe magnetic exchange interactions shown in Fig. 5(b) of Paper [3], our results indicates that if one uses local chemical environment-independent "average" magnetic exchange couplings as obtained by employing methods such as CPA, then this will lead to an overestimation of the Curie temperature for a chemically disordered FeNi by about 10%.

6.3 IMPLICATIONS

In this chapter, we demonstrate the effect of local chemical environment on the magnetic exchange couplings in disordered FeNi. From our calculations, we demonstrate a large variation in the first nearest neighbour Fe-Fe couplings that vary from 4.7 meV to 36.5 meV in comparison to the value of 26.5 meV for the Fe-Fe magnetic exchange couplings that are present in a fully ordered FeNi. The use of supercell technique with different distributions of Fe and Ni atoms allow us to include effects that occur due to the symmetry-broken local chemical environment around individual atoms. Note that these effects are not included in effective mean-field approaches such as CPA. Thus, this shows that the effects beyond CPA are necessary to obtain accurate magnitude of magnetic exchange couplings in systems with chemical disorder.

The absence of the simple relation between the magnitude of the magnetic exchange couplings and the local chemical environment (upto second nearest neighbour) around different Fe-Fe pairs present in our supercells implies that the correlation between the magnitude of the magnetic exchange couplings and the local chemical environment is rather long-ranged as can be expected in an itinerant magnetic system like FeNi. At the same time, this also makes it very difficult to incorporate the information about the variations of magnetic exchange coupling values into a Heisenberg model to obtain T_c.

Finally, from our model study of the Heisenberg model with first nearest neighbour interactions sampled from Gaussian distributions on an fcc lattice, we demonstrate that the variation occurring in the magnetic exchange coupling due to the chemical disorder can lead to a reduction in T_c. This implies that if one uses local environment-independent "average" magnetic exchange couplings obtained by mean-field approaches such as CPA to estimate the critical temperature of a disordered system, then this would lead to an overestimate of the critical temperature in such systems. Finally, we note that the results presented in this thesis do not yet allow, for a conclusive understanding of a decrease in T_c with increasing standard deviation of the Gaussian distribution. Therefore, this is currently an open question. We will explore more on this in the future work.

6.4   PUBLICATION

This work is available as a preprint as *»Impact of chemical disorder on magnetic exchange interactions in L1$_0$-FeNi (tetrataenite)«* on arXiv [3]. I performed all the calculations and wrote the first draft which was further discussed and corrected by my supervisor C. Ederer.

Impact of chemical disorder on magnetic exchange interactions in L1$_0$-FeNi (tetrataenite)

Ankit Izardar and Claude Ederer

Materials Theory, ETH Zürich, Wolfgang-Pauli-Strasse 27, 8093 Zürich, Switzerland

(Dated: March 2, 2022)

We investigate the effect of chemical disorder on the magnetic exchange couplings and the Curie temperature (T_c) in L1$_0$-ordered FeNi using first-principles-based calculations. We use supercells to model chemical disorder, to account for the specific symmetry-broken local chemical environments around the individual atoms. We find a very strong variation of the most dominant first-nearest neighbor Fe-Fe interaction for different inequivalent Fe-Fe pairs, ranging from around 5 meV to 37 meV, compared to a coupling strength of 27 meV in the ordered state. To estimate the influence of such strong variations of the magnetic coupling constants on the Curie temperature of the disordered or partially ordered state, we study a simple Heisenberg model with random Gaussian-distributed nearest neighbor couplings on an fcc lattice. Our Monte Carlo simulations for this model indicate that strongly varying exchange couplings, such as those obtained for FeNi, can lead to a reduction of T_c of around 10 % relative to the one obtained using only the average coupling.

I. INTRODUCTION

The chemically ordered ferromagnet L1$_0$-FeNi (tetrataenite) has recently generated considerable interest as a rare-earth-free, low-cost permanent magnet, due to its high magneto-crystalline anisotropy energy and large saturation magnetization [1–11]. Since its discovery by Néel and coworkers in the early 1960s [12, 13], several attempts have been made to synthesize L1$_0$-FeNi with a high degree of chemical order [14–17]. However, the synthesis of a fully ordered structure remains challenging, due to the rather low order-disorder transition temperature, which is around 590 K [12, 13, 18]. At this temperature, the diffusivity of atoms is too low for the ordered structure to form on reasonable timescales. Therefore, "naturally occurring" tetrataenite has only been found in iron meteorites [19–23]. Due to the difficulties in obtaining fully ordered samples, it becomes essential to investigate and understand how deviations from the perfect order affect the magnetic properties, in particular the Curie temperature, T_c, and magnetic anisotropy, of L1$_0$-FeNi.

Experimentally, only the Curie temperature of the disordered system ($T_c \approx 785$ K [24, 25]) is accessible, since the ordered system disorders on heating at temperatures above ~ 700 K. Thereby, the effective "disordering temperature" depends strongly on the heating rate [26]. On time-scales typical for magnetization measurements, disordering occurs around 820 K, i.e., above the Curie temperature of the disordered system, and results in an abrupt vanishing of the magnetization [3]. This indicates that the nominal Curie temperature of the ordered system would be noticeably higher than that of the disordered system.

Several previous studies have used first-principles calculations to obtain the Curie temperature in L1$_0$-FeNi. For example, Edström *et al.* [5] and Tian *et al.* [9] obtained values for the Curie temperature of the ordered phase of 916 K and 780 K, respectively, using slightly different electronic structure methods. They also found that chemical disorder leads to a reduction of the Curie temperature.

Both of these studies have used the coherent-potential approximation (CPA) [27, 28] to incorporate chemical disorder in the material. The CPA is based on an effective medium description of the atomic environments, and thus provides a very efficient method for the treatment of disorder effects in random alloys using only a single unit cell. However, CPA does not include effects related, e.g,. to the local symmetry-breaking of a specific chemical environment around an individual atom. Such effects beyond CPA can be particularly relevant, e.g., for the magnetic anisotropy, as we showed in our previous work, where we have used supercells with different distributions of Fe and Ni atoms to investigate the effect of chemical disorder [10, 29]. These calculations indicate that, for example, a moderate increase in Fe content, while reducing the degree of chemical order in the system, leads to an increase of the magneto-crystalline anisotropy energy, an effect not captured within the CPA.

In the present work, we use first principles calculations based on density functional theory (DFT) to provide further insights into the effect of variations in the local chemical environment on the magnetic exchange interactions, and consequently the Curie temperature, in partially ordered FeNi. To model the chemical disorder, we follow a similar approach as in our previous work [10, 29], i.e., we incorporate the effect of a disordered local atomic environment on the magnetic coupling by employing supercells. We find that treating the disorder on a local level gives rise to remarkably strong variations of the first nearest neighbour Fe-Fe coupling. Our subsequent analysis of the correlation between the specific local chemical environment and the corresponding magnetic exchange couplings indicates that the magnetic coupling is governed by long range effects that clearly go beyond the closest neighbor environment. This makes it extremely challenging to consider such configuration-dependent couplings for the calculation of T_c and other thermodynamic properties. In order to obtain a rough es-

timate of how such strong variations of the magnetic coupling constants will affect the Curie temperature, compared to using only an average coupling, obtained, e.g. from an effective medium treatment of chemical disorder, we perform Monte Carlo simulations for a simple Heisenberg model with random Gaussian-distributed coupling constants. We find that variations of the same order as obtained in our DFT calculations for FeNi can lead to a reduction of T_c of around 10%.

In the following, we first describe the computational method we use to obtain magnetic exchange couplings, and then present our results for both ordered and partially disordered FeNi.

II. COMPUTATIONAL METHOD

A. Magnetic exchange interactions

Within the (classical) Heisenberg model, the energy of a magnetic system is expressed as a sum over pairwise (bilinear) interactions between localized magnetic moments:

$$E = -\frac{1}{2}\sum_{i\neq j} J_{ij}\mathbf{S}_i \cdot \mathbf{S}_j \quad . \tag{1}$$

We use the convention that $\mathbf{S}_i$ is a normalized vector describing only the direction of the magnetic moment at site i.

It is well known that, for an itinerant magnetic material such as FeNi, the Heisenberg model is not necessarily a good approximation [30], and Eq. (1) is typically only valid for not too large fluctuations around the ferromagnetic ground state. Thus, to calculate magnetic exchange couplings, J_{ij}, we use the following well-known equation based on the magnetic force theorem, which is obtained by considering the energy variation with respect to infinitesimal rotations of the magnetic moments [31]:

$$J_{ij} = \frac{1}{2\pi}\mathrm{Im}\int_{-\infty}^{\varepsilon_{\mathrm{F}}} \mathrm{d}\varepsilon \sum_{mm'm''m'''} \Delta_i^{mm'} G_{ij,\downarrow}^{m'm''}(\varepsilon)\Delta_j^{m''m'''} G_{ji,\uparrow}^{m'''m}(\varepsilon) \quad . \tag{2}$$

Here, $\Delta_i^{mm'}$ ($\Delta_j^{m''m'''}$) is the local exchange splitting on site i (j), and $G_{ji,\uparrow}^{m'''m}$ ($G_{ij,\downarrow}^{m'm''}$) is the spin-up (spin-down) intersite Green's function. Both quantities are expressed within a tight-binding-like basis, where each basis-orbital (with index m) is localized on a specific site.

To evaluate the quantities in Eq. (2), we first obtain the electronic structure from plane-wave-based density-functional theory (DFT) calculations, and then transform the corresponding Kohn-Sham Hamiltonian into a basis of localized Wannier functions [32–35]. As described in more detail in Sec. III A, we use Wannier functions defined by orbital projection and subsequent orthonormalization (corresponding to the "initial projections" in the `wannier90` code [36]). This leads to a set of atom-centered basis orbitals. As shown in Sec. III A, an excellent representation of all occupied bands in FeNi can be achieved by using a full set of s, p, and d projections for each atom.

In contrast, constructing maximally localized Wannier functions (MLWFs) [37] for FeNi, results in a set of Wannier functions where the Wannier orbitals corresponding to the s and p projections become localized in between the atoms, and thus cannot be used to evaluate Eq. (2). This is similar to what has been described for the nearly free-electron-like bands in fcc Cu (and other $3d$ transition metals), see e.g., Ref. 38. Further details are presented in Sec. III A.

After a suitable set of Wannier functions has been constructed, we follow the approach outlined in Ref. [35] to obtain exchange couplings for different pairs of atoms.

B. Computational details

In order to accommodate both the fully ordered L1$_0$ structure of FeNi as well as some configurations with (partial) chemical disorder, we use an 8-atom cell, corresponding to a $\sqrt{2}\times\sqrt{2}\times 1$ supercell of the conventional cubic 4-atom fcc unit cell, or, equivalently, to a $2\times 2\times 1$ supercell of the 2-atom tetragonal primitive unit cell of the L1$_0$ structure. For test purposes, we also perform some calculations for the perfectly ordered L1$_0$ structure using the 2-atom primitive unit cell. In all cases, except where otherwise noted, we fix the lattice parameters and atomic positions to that of a perfectly cubic fcc lattice with lattice constant $a = 3.56$ Å, and then distribute Fe and Ni atoms over the available sites within the cell in different ways.

We perform DFT calculations using the Vienna *ab initio* Simulation package (VASP) [39], the projector-augmented wave method (PAW) [40, 41], and the generalized gradient approximation according to Perdew, Burke, and Ernzerhof (PBE) [42]. Brillouin zone integrations are performed using the tetrahedron method with Blöchl corrections and a Γ-centered $12\times 12\times 16$ **k**-point mesh for the 8-atom cell. The plane wave energy cut-off is set to 550 eV, and the total energy is converged to an accuracy of 10^{-8} eV. Our PAW potentials include $3p$, $4s$, and $3d$

states in the valence for both Fe and Ni. All calculations are performed for the ferromagnetically ordered state.

A Wannier representation of the Kohn-Sham Hamiltonian is then obtained using the `wannier90` code [36], using the same k-point mesh as for the DFT calculations. To check the convergence of the calculated magnetic exchange couplings with respect to the **k**-point sampling, we perform calculations using up to $14 \times 14 \times 18$ **k**-points and find our results to be sufficiently converged using a $12 \times 12 \times 16$ **k**-point mesh.

To obtain the Curie temperature for the ordered case, using the Heisenberg model, Eq. (1), with the coupling constants obtained from our DFT calculations, we perform Metropolis Monte Carlo simulations, as implemented in the UppASD package [43]. We consider magnetic exchange couplings for all pairs of atoms up to a distance of $10a$ (~ 25.17 Å). To accurately determine T_c, accounting for potential finite size effects due to the limited size of our simulation cells, we use the Binder cumulant method [44]. Thus, T_c is obtained as the temperature where the fourth-order Binder cumulants, obtained for three different cell sizes, cross. We consider cell-sizes of $20 \times 20 \times 20$, $30 \times 30 \times 30$, and $36 \times 36 \times 36$, relative to the primitive tetragonal 2-atom cell of the L1_0 structure. For the test calculations presented in Fig. 3(b), we use a cell size of $20 \times 20 \times 20$.

For the model study presented in Sec. III D, we use a $15 \times 15 \times 15$ supercell of the conventional fcc cubic cell. We then initialize the magnetic couplings for all nearest neighbor pairs within this cell individually by drawing random numbers from a Gaussian distribution with varying standard deviation, $\sigma > 0$, and a mean value of $\mu = 1$. For $\sigma = 0.0$, the coupling constants of all nearest neighbor pairs are identical and equal to the mean of the Gaussian distribution ($\mu = 1.0$). The Curie temperature for each $\sigma > 0.0$ is obtained by taking an average over 100 instances of the Gaussian-distributed magnetic exchange couplings with different random seeds. Convergence with respect to the number of instances of the randomized system has been verified by monitoring the cumulative average of T_c with increasing number of instances over all 100 samples.

III. RESULTS AND DISCUSSION

A. Construction of Wannier functions

As outlined in Sec. II A, we start by constructing a set of Wannier functions from orthonormalized projections on s, p, and d orbitals for each Fe and Ni atom in the unit cell. We use an outer energy window ranging from -10 eV up to about 31 eV, which contains all occupied valence bands plus a certain number of empty bands. Furthermore, in order to accurately reproduce all occupied bands, we employ a frozen (inner) energy window from -10 eV up to about 1 eV above the Fermi energy. The band dispersion (only for the majority spin
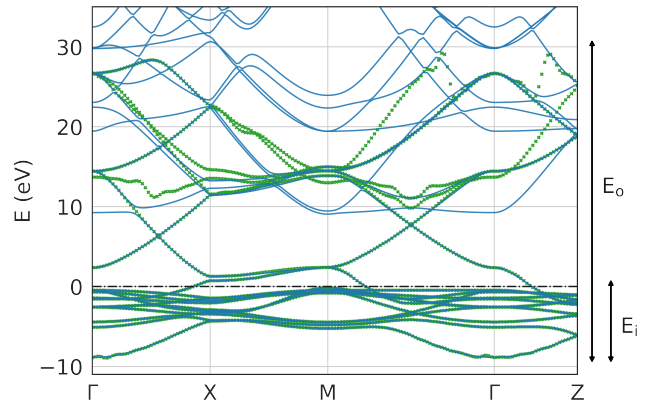
FIG. 1. Majority spin bandstructure of chemically ordered L1$_0$-FeNi. Blue and green dots represent the Kohn-Sham and Wannier-interpolated bands, respectively. Outer and inner energy windows, E_o and E_i, are indicated on the right side of the plot. The Fermi level defines zero energy.

component) obtained from the resulting Wannier functions for the minimal 2-atom cell of the fully ordered L1$_0$ structure is shown in Fig. 1, together with the underlying Kohn-Sham bandstructure.

One can see that all bands below ~ 10 eV are well described by the Wannier-interpolated bands. Some weak oscillations can be seen in the lowest lying, free-electron-like band around the Γ-point. These are due to the fact that the k-mesh along the high-symmetry lines used to obtain the interpolated bandstructure is much finer than the homogeneous k-mesh used to construct the Wannier functions, and that, in order to obtain atom-centered Wannier functions, we do not apply the usual "disentanglement procedure" to obtain an optimally k-connected subspace. We note that the calculation of the magnetic exchange couplings is based on the original homogeneous k-point mesh, where the Wannier bands are identical to the DFT Kohn-Sham bands by construction. For the minority-spin bands (not shown), we obtain a similar good agreement between the Wannier-interpolated and the occupied Kohn-Sham bands.

B. Magnetic interactions in L1$_0$-ordered FeNi

Next, we calculate the magnetic exchange couplings for the ordered L1$_0$-phase of FeNi, using the method described in Sec. II A. In Fig. 2, we compare the magnetic exchange couplings obtained in the present study (shown by the black dots) with those calculated by Edström *et al.* [5] (shown by the green triangles). The different subpanels show the couplings corresponding to Fe-Fe, Fe-Ni, and Ni-Ni pairs as a function of distance. Overall, there is very good agreement between the two data-sets, except for a few cases discussed further below. One can see that the Fe-Fe couplings are strongest and rather long-ranged while the Fe-Ni and Ni-Ni interaction is weaker
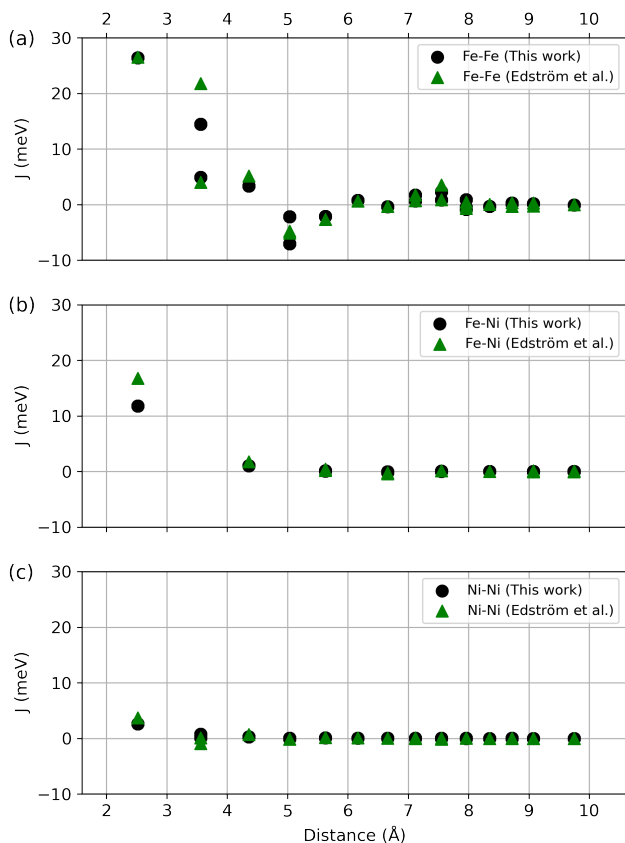
FIG. 2. Magnetic exchange couplings for (a) Fe-Fe, (b) Fe-Ni, and (c) Ni-Ni pairs as a function of atomic distance in the ordered $L1_0$ phase of FeNi as calculated in this work (black dots) and by Edström et al. [5] (green triangles).

and decays rather quickly with distance.

Note that for certain distances (e.g., for the one corresponding to second nearest-neighbour distance, $d_{ij} = a_0 = 3.56$ Å), two distinct values for J_{ij} are obtained, depending on the orientation (in-plane versus out-of-plane) of the corresponding pair relative to the tetragonal axis, i.e., the axis defined by the long range order. In particular for the second nearest neighbor Fe-Fe interaction, this difference is rather large. This already indicates a strong configuration dependence of the magnetic coupling, which will be further analyzed in Sec. III C using supercells with partial chemical disorder.

For the second nearest neighbor Ni-Ni pairs, the coupling is rather weak and thus the (absolute) difference between in-plane and out-of-plane coupling is small. Furthermore, one can see that Fe-Ni couplings for certain distances are "missing" (e.g., corresponding to second nearest neighbors on the fcc lattice, $d_{ij} = a_0 = 3.56$ Å). This is due to the arrangement of Fe and Ni atoms in the underlying $L1_0$ structure.

The good agreement between our results and the calculations of Edström et al. (Ref. [5]) is remarkable, since rather different electronic structure methods, involving
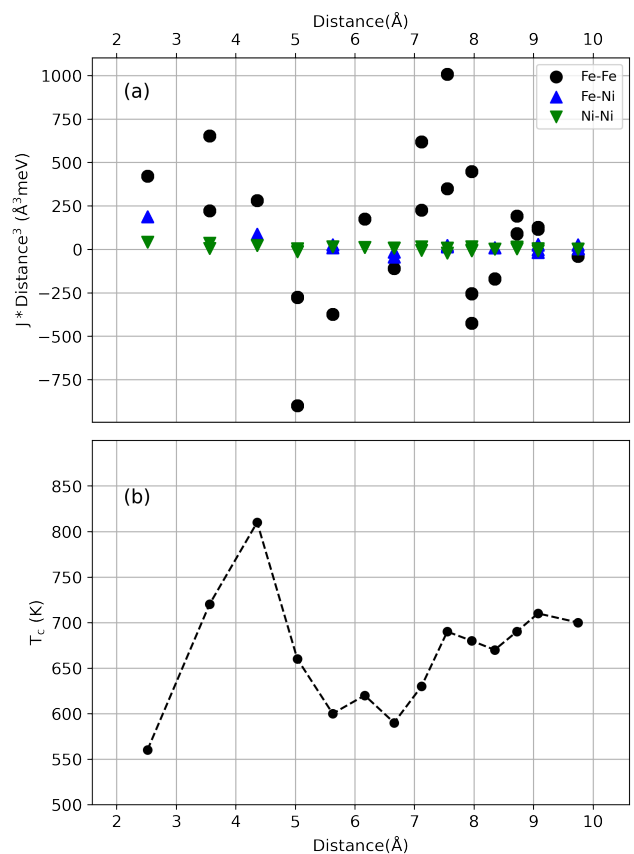
FIG. 3. (a) Magnetic coupling constants as a function of atomic distance multiplied with the cube of the corresponding atomic distance, $J_{ij} \cdot d_{ij}^3$, calculated for the ordered phase of FeNi. Coupling constants corresponding to Fe-Fe, Fe-Ni, and Ni-Ni pairs are shown by black, blue, and green markers, respectively. (b) Ferromagnetic Curie temperature T_c, obtained from Monte Carlo simulations, as a function of the cutoff distance used for the Fe-Fe interactions (see text).

different approximations and basis sets, have been employed. Furthermore, our calculations are based on a metrically cubic fcc lattice, whereas Edström et al. have used tetragonal lattice vectors with a slightly different c/a ratio. The biggest difference is observed for the second nearest neighbor (in-plane) Fe-Fe coupling and the first nearest neighbor Fe-Ni coupling, for which Edström et al. obtain a noticeably stronger coupling (by around 7 meV and 5 meV, respectively). Our calculated coupling constants also appear to be in good agreement with more recent calculations by Tian et al. [9] [45]

From Fig. 2(a) one can see that there are noticeable Fe-Fe couplings even for rather large atomic distances. To further analyze this distance dependence, Fig. 3(a) shows the same coupling constants as in Fig. 2, but multiplied with the cube of the corresponding inter-atomic distances, i.e. $J_{ij} \cdot d_{ij}^3$. For the Fe-Ni and Ni-Ni couplings, the corresponding data-points still converge quickly towards zero for large distances, which means that these

couplings decay with distance faster than d_{ij}^{-3}. On the other hand, for the Fe-Fe pairs, one can see that the data-points oscillate and do not seem to decay even for very long atomic distances. As pointed out in previous works [5, 46], this indicates an approximate d_{ij}^{-3} dependence of the Fe-Fe interaction which, together with the oscillatory behavior, is typical for metals with RKKY-like exchange interactions.

Fig. 3(b) shows the ferromagnetic Curie temperature, T_c, obtained from Monte Carlo simulations of the Heisenberg model, where the Fe-Fe interactions are considered only up to a certain maximum inter-atomic distance. For the Fe-Ni and Ni-Ni pairs, all calculated coupling constants have been included, i.e., up to a very large distance of $10a_0$. Note that due to the fast decay of these couplings, the following results should be unaffected by the specific cutoff-distance used for the Fe-Ni and Ni-Ni interactions. It can be seen that, due to the long range of the Fe-Fe interaction, the calculated T_c exhibits strong variations as function of the Fe-Fe cutoff distance, but seems to converge to a value around 700 K once all Fe-Fe interactions up to a distance of around 8 Å are taken into account. This shows that, in order to obtain a reliable estimate of T_c in this system, it is essential to include Fe-Fe interactions up to rather large distances.

Based on these test calculations, we now obtain an accurate estimate for T_c from Monte Carlo simulations of the Heisenberg model including all calculated coupling constants up to a maximum distance of $10a_0$ and then perform a Binder cumulant analysis, as described in Sec. II B. We obtain a value of $T_c = 736$ K. Note that for the test calculations shown in Fig. 3(b), T_c is obtained simply from the peak position of the calculated temperature dependence of the specific heat, and thus differs somewhat from the more accurate value obtained via the Binder cumulants. Our calculated T_c agrees well with the value of about 780 K obtained by Tian *et al.* [9], whereas the T_c of 916 K obtained by Edström *et al.* [5] is noticeably higher. This is due to the stronger second nearest neighbor Fe-Fe and first nearest neighbor Fe-Ni coupling constants obtained in Ref. 5 (see Fig. 2). Note that both our and the value of Tian *et al.* are lower than the experimental T_c of the disordered system and thus seem to underestimate the "true" Curie temperature of the ordered state.

C. Magnetic interactions for (partially) disordered FeNi

We now investigate the effect of chemical disorder on the magnetic exchange couplings by starting from the fully ordered case, and then successively exchanging the positions of one or two pairs of Fe and Ni atoms within an 8-atom supercell, resulting in the two configurations shown in Fig. 4(b) and (c). Note that all other configurations that can be created by exchanging one Fe-Ni pair in this 8-atom supercell are equivalent to the one shown

TABLE I. First nearest-neighbour Fe-Fe magnetic exchange interaction (in meV) for relaxed and unrelaxed 1-pair-exchanged and 2-pairs-exchanged configurations.

	Unrelaxed	Relaxed
1-pair-exchanged	7.4	10.1
	36.5	38.8
	19.1	19.9
	4.7	6.8
2-pairs-exchanged	23.1	21.9
	14.7	15.5

in Fig. 4(b), whereas several distinct configurations can be created by exchanging two Fe-Ni pairs. For simplicity we limit our study to the configuration depicted in Fig. 4(c). In the following, we refer to these two configurations as "1-pair-exchanged" and "2-pairs-exchanged", respectively.

In Fig. 5(b), we list the magnetic exchange couplings obtained for all inequivalent first nearest neighbor Fe-Fe pairs in the three different configurations. The corresponding local atomic environments are also indicated and will be discussed further below. One can see that the calculated values vary drastically, from 4.7 meV to 36.5 meV, while the corresponding value in the fully ordered structure is 26.5 meV. We note that, if the nearest neighbor Fe-Fe coupling would be completely configuration-independent, then all values listed in Fig. 5(b) would be identical. The large variation of the Fe-Fe nearest neighbor coupling in the different cases thus shows that the local chemical environment has a significant influence on the magnitude of the magnetic exchange interactions in FeNi. As already discussed in Sec. I, such variations are not captured by effective medium methods such as the CPA, which are often used to model chemical disorder in alloys.

The magnetic exchange couplings shown in Fig. 5(b) are obtained by decorating the sites within a perfect fcc lattice in different ways with Fe and Ni atoms, without allowing the atomic positions to relax within the resulting lower symmetry. In order to assess the effect of such relaxations, we now recalculate the magnetic coupling constants for the 1-pair-exchanged and 2-pairs-exchanged configurations after allowing all atomic positions to relax, while still keeping the lattice vectors of the supercell fixed. The results for the first nearest neighbor Fe-Fe couplings are shown in Table I and are compared to the corresponding values for the unrelaxed case. It can be seen that the relaxation leads to changes in the magnetic coupling constants of up to about 2 meV, but the effect is clearly significantly weaker than the effect due to the different chemical environments.

The strong configuration dependence of the first nearest Fe-Fe coupling raises the question of whether it is possible to identify simple rules on how the strength of this coupling depends on the local atomic environment.
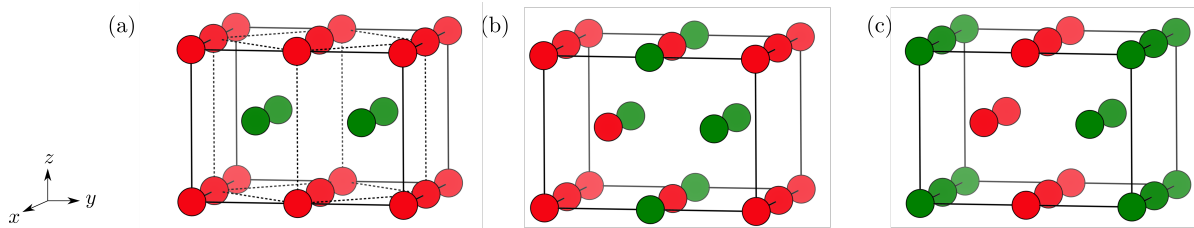
FIG. 4. Different ordered and (partially) disordered configurations considered in this work, depicted in the $2 \times 2 \times 1$ supercell relative to the primitive tetragonal cell of the $L1_0$ structure: (a) ordered, (b) 1-pair-exchanged, and (c) 2-pairs-exchanged. Fe and Ni atoms are represented by red and green spheres, respectively. Dotted lines in (a) indicate the underlying conventional cubic cell of the fcc lattice.
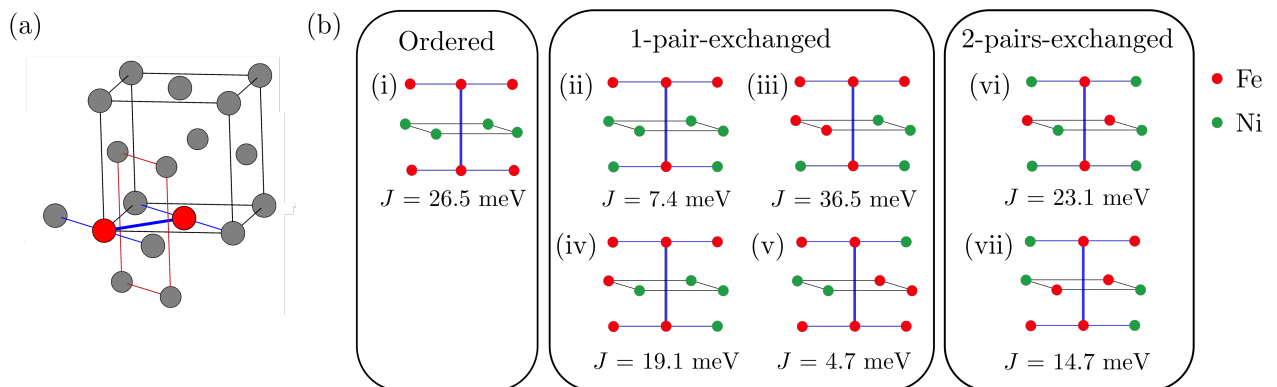

FIG. 5. (a) Depiction of the shared first nearest and first/second nearest neighbor environment for a pair of nearest neighbor sites (indicated as red colored spheres) in an fcc lattice. The conventional cubic cell is also shown for clarity. (b) Schematic showing the occupation of the shared first and first/second nearest neighbour environments for all nearest neighbor Fe-Fe pairs that are present in the ordered [(i)], 1-pair-exchanged [(ii)-(v)], and 2-pairs-exchanged configurations [(vi)-(vii)] along with the corresponding values of the magnetic coupling constant J.

For this purpose, we analyze the distribution of atoms on the sites that are closest neighbors to *both* Fe atoms forming the pair under consideration. As shown in Fig. 5(a) there are four such sites, which form a square in the midplane perpendicular to the line connecting the two coupled sites. These four sites represent the minimal environment to be considered in any model describing the configuration dependence of the first nearest neighbor coupling. The next "shell" around the coupled Fe-Fe pair is formed by those sites that are first nearest neighbors to one of the coupled sites and second nearest neighbors to the other site. There are again four such sites, which form a rectangle in the plane parallel to the Fe-Fe distance vector and perpendicular to the plane formed by the common first nearest neighbors (see Fig. 5(a)).

In Fig. 5, we schematically depict the occupation of both the shared first nearest and the shared first/second nearest neighbor sites for all the inequivalent nearest neighbor Fe-Fe pairs included in the ordered, 1-pair-exchanged, and 2-pairs-exchanged configurations, along with the value of the corresponding magnetic exchange couplings. It is obvious that the shared first nearest neighbor environment is not sufficient to classify the different coupling constants, since, e.g., cases (iii), (v), and

(vi) all have an equivalent shared first nearest neighbor environment but exhibit vastly different magnetic coupling constants (including both the highest and lowest calculated values of 36.5 meV and 4.7 meV). The same holds for cases (i) and (ii).

Considering both the shared first and first/second nearest neighbor environment, all inequivalent Fe-Fe pairs contained in our three configurations exhibit different local environments, which is in principle compatible with a local model for the exchange coupling based on this environment. However, to really establish or disprove such a model, one has to consider much larger supercells, that allow to sample more configurations, and also include cases with identical first/second nearest neighbor environment but different further neighbor environment. This would require an excessive computational effort. Considering that, in general, the applicability of a short-range local model for an itinerant magnetic system such as FeNi is rather questionable, we therefore refrain from sampling further couplings using larger and larger supercells. Instead, we try to estimate the effect of a strong configuration dependence of the magnetic coupling constants on the Curie temperature of a disordered magnetic system using a simple Heisenberg model with
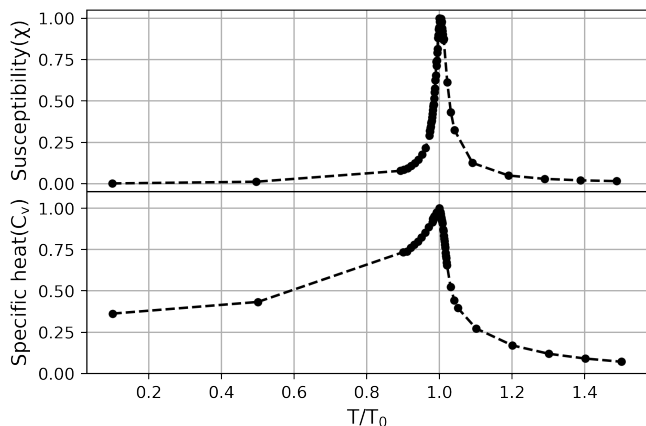
FIG. 6. (a) Susceptibility, and (b) specific heat as a function of temperature (in relative units) obtained from Monte Carlo simulations for a simple Heisenberg model with only nearest neighbor couplings on an fcc lattice for the case when all coupling constants are identical ($\sigma = 0$). T_0 is the critical temperature for $\sigma = 0$.
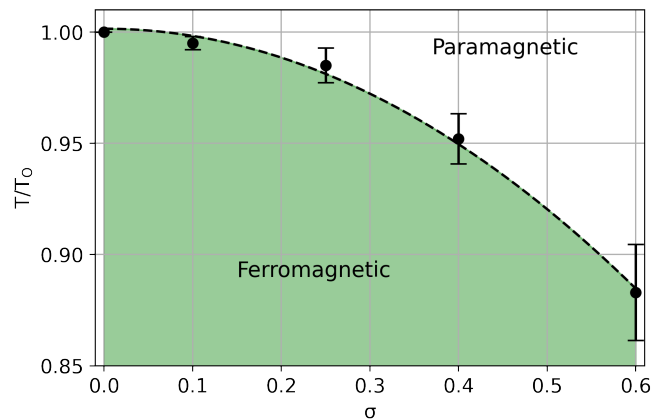

FIG. 7. Curie temperature T_c of the Heisenberg model with Gaussian-distributed coupling constants as a function of the standard deviation, σ (defined relative to the mean value of the Gaussian distribution). $T_0 = T_c(\sigma = 0)$ is the Curie temperature obtained for the average coupling, and the error bars indicate the standard deviation of the mean obtained by averaging over 100 instances with different random seeds for each σ (see text). The black dashed line is a quadratic fit to the data.

random couplings.

D. Model study with random couplings

The very high sensitivity of the magnetic coupling constants on the specific chemical environment, and the high computational effort to fully resolve this configuration dependence (if at all possible), represents a big obstacle for the reliable estimation of magnetic ordering temperatures for disordered itinerant magnets such as FeNi from first principles calculations. In the following, we therefore employ a strongly simplified model to obtain a rough estimate of how the strong configuration-dependent variations of the exchange couplings can affect the Curie temperature of a disordered magnetic system, in comparison to the Curie temperature obtained using only configuration-independent "average" magnetic coupling constants.

Specifically, we consider a Heisenberg model with only nearest neighbor interactions on an fcc lattice, and we approximate the configuration-dependent variations of the magnetic coupling constants by a Gaussian-distributed random variable, where the mean value of the Gaussian distribution represents the average coupling constant, and its standard deviation, σ, quantifies the configuration-dependent variations. We then perform temperature-dependent Monte Carlo simulations as outlined in Sec. II B, and analyze how the obtained Curie temperature depends on σ, i.e., on the strength of the variation in the magnetic coupling constants.

Fig. 6 shows the calculated susceptibility (χ) and specific heat (C_v) as a function of temperature for this model for the case when all coupling constants are identical to the average one ($\sigma = 0$). One can see that both χ and

C_v exhibit clear peaks at the same critical temperature T_0. However, since the peak in the susceptibility appears much sharper than the one in the specific heat, in the following we use the peak value of χ to accurately determine the Curie temperature as function of σ.

Fig. 7 shows the variation of the average Curie temperature, T_c, relative to T_0, as a function of the standard deviation σ of the Gaussian distributed random magnetic coupling constants. Note that σ corresponds to a Gaussian distribution with a mean equal to the average magnetic coupling, and is therefore defined relative to this average coupling. One can see that T_c decreases with increasing standard deviation σ, i.e. with increasing "randomness" of the magnetic exchange couplings, and that this decrease can be fitted well with a quadratic dependence. This indicates that using configuration-independent "average" magnetic exchange couplings obtained by effective medium approaches such as CPA are expected to overestimate the critical temperature of a disordered system.

If we take the seven different values for the configuration-dependent nearest neighbor interaction obtained from the ordered, the 1-pair-exchanged, and the 2-pairs exchanged configuration and evaluate the empirical standard deviation, we obtain $\sigma \approx 0.6$ (relative to an average value of $18.9\,\mathrm{meV}$). Comparing this with the data shown in Fig. 7, this would correspond to a reduction of T_c of about $10\,\%$ compared to the value obtained using only an average coupling strength. We note that this is clearly a very naive estimation based on a very small number of samples, but it shows that a strong configuration dependence of the magnetic coupling, as observed

for FeNi in Sec. III C, can indeed lead to a noticeable reduction of T_c compared to that obtained from average effective medium couplings.

Note that the effect of random magnetic exchange couplings on the magnetic transition temperature of a Heisenberg model with nearest and next-nearest antiferromagnetic coupling on a two-dimensional square lattice was studied previously by Li *et al.* [47]. Thereby, the nearest neighbor coupling was obtained from a homogeneous random distribution within a given range, and it was also found that the transition temperature decreases with increasing variation of the random magnetic exchange couplings.

IV. SUMMARY AND CONCLUSIONS

In summary, we have investigated the effect of chemical disorder on the magnetic exchange couplings in L1$_0$-FeNi using first principles DFT calculations. Thereby, we have used supercells with different atomic distributions, to specifically include effects due to the symmetry-broken local environments around the individual atoms that are not included in effective medium approaches such as CPA. We find that such effects can lead to rather large variations of the magnetic exchange couplings, exemplified by our analysis of the nearest neighbor Fe-Fe coupling, which exhibits values ranging from 4.7 meV up to 36.5 meV, with a value of 26.5 meV obtained for the fully ordered structure.

Our analysis of the shared first and shared first/second nearest neighbor chemical environments of the different inequivalent Fe-Fe nearest neighbor pairs included in our supercells indicates that the strength of the couplings is affected by long range effects that go beyond the closest neighbor shell, as can be expected for an itinerant metallic material such as FeNi. The lack of a simple relation that relates the variation of an individual J_{ij} (relative to the corresponding average value) to its local chemical environment makes it very challenging to incorporate effects beyond CPA in the calculation of T_c. However, our simple model study using random Gaussian-distributed nearest neighbor couplings on an fcc lattice suggests that such local variations of the coupling constants can lead to a reduction of T_c of up to 10 %, compared to that obtained using only an average coupling.

Thus, there is a hierarchy of effects that in general tend to reduce the magnetic ordering temperature in random alloys such as partially ordered FeNi. First, the "average" coupling strength is affected by the chemical disorder. For example, Tian *et al.* obtain a reduction of around 30-35 % of the nearest neighbor Fe-Fe coupling obtained within CPA for the disordered system compared to the fully ordered case [9]. This is in principle consistent with our supercell calculations, where the simple average of this coupling over all inequivalent Fe-Fe pairs in our two disordered configurations gives about 17.6 meV, i.e., a reduction by about 35 % compared to the ordered case.

However, one should note that this average is based on only very few samples. Second, the random connectivity between different magnetic atoms (Fe and Ni in our case) will also affect the Curie temperature relative to the ordered case, which corresponds to a very regular network of Fe-Fe, Fe-Ni and Ni-Ni bonds. Finally, the variation of the coupling strength according to the specific chemical environment around the atoms in the random alloy can lead to a further decrease of T_c, as indicated by our simple model. It is mainly this last effect that we have quantified within this work.

Furthermore, it appears that our first-principles-based results are underestimating the (hypothetical) Curie temperature of the fully ordered system. It is unclear whether this underestimation is related to the general applicability of the (classical) Heisenberg model to FeNi or whether it is caused by deficiencies of the generalized gradient approximation in the underlying DFT calculations (or other approximations in the method). However, we note that the comparison with the results obtained by Edström *et al.* [5] also demonstrates that moderate changes in specific calculated coupling constants can lead to rather strong differences in the predicted Curie temperatures.

Appendix A: Orbital decomposition of nearest neighbor Fe-Fe coupling

Eq. (2) in principle allows for a decomposition of the coupling constants J_{ij} into different orbital contributions. However, for the case of L1$_0$-FeNi, the quantities appearing in Eq. (2), in particular the exchange splitting $\Delta_i^{mm'}$, contain off-diagonal elements mixing the d and s type Wannier orbitals. Nevertheless, by restricting the summation in Eq. (2) to only the diagonal elements Δ_i^{mm} and considering only contributions from the d-type orbitals, one can obtain a "d-only" contribution to the magnetic coupling.

In this way, we obtain a d-only contribution to the Fe-Fe coupling of 29.6 meV (second row in Table II). This value is larger than the full value of 27.2 meV (first row in Table II), obtained by considering all contributions in Eq. (2), showing that here the combination of sp and orbitally mixed terms leads to a small negative contribution to J_{ij} [48]. Furthermore, it demonstrates that,

TABLE II. Magnetic exchange couplings, J_{ij}, for the nearest-neighbor Fe-Fe interaction in L1$_0$-FeNi obtained using different sets and subsets of Wannier functions. The first column indicates the different sets of Wannier functions that have been constructed, while the second column indicates which terms are considered in Eq. 2 when evaluating the corresponding J_{ij}. All calculations are performed for the primitive 2-atom unit cell.

Wannier set	Terms in Eq. 2	J_{ij} (meV)
$d + s + p$ (projections)	all	27.2
$d + s + p$ (projections)	d-only	29.6
d (projections)	all	35.7
d (MLWFs)	all	43.4

as probably expected, the main contribution to the magnetic coupling stems from the d orbitals.

This raises the question of whether it would be sufficient to consider only the d-bands in the first place, i.e., construct a smaller set of Wannier functions describing only the d bands, and still obtain a good estimate for J_{ij}. To test this hypothesis, we construct two additional sets of Wannier functions, where we include only five d-orbitals per atom. For the first set, we obtain the Wannier functions from orthonormalized atomic projections as before, while for the second set we perform a subsequent minimization of the quadratic spread functional to obtain MLWFs. In both cases we use an (outer) energy window ranging from $-10\,\mathrm{eV}$ to about $5\,\mathrm{eV}$ above the Fermi level and obtain a set of atom-centered d-like orbitals suitable to evaluate Eq. (2). In both cases also the Wannier-interpolated bands resemble the DFT band-structure in the energy range of the d-bands, i.e., between approximately $-5\,\mathrm{meV}$ and the Fermi level for the majority spin channel.

The magnetic coupling constants for the nearest-neighbour Fe-Fe coupling obtained from these two additional sets of Wannier functions are listed in the third and fourth row of Table. II. It can be seen that the corresponding values (in particular for the set of MLWFs) are significantly larger than the d-only contribution obtained from the full description using also s and p bands. This shows that, even though the d-orbitals make up the main contribution to the magnetic coupling constants, it is nevertheless important to include s and p states to accurately account for their effect on the d band dispersion. We note that, due to the entanglement of d and sp contributions in the bandstructure of FeNi, the d subset of the full $d + s + p$ Wannier basis and the two different d-only Wannier sets (projected and MLWFs) are all describing slightly different subspaces of the occupied Kohn-Sham states.

Only the $d + s + p$ Wannier set results is a complete and accurate description of all occupied bands in FeNi, and therefore only the corresponding value of J_{ij} should be considered as "correct" (or most accurate). Nevertheless, our analysis raises the question of a potential basis set dependence of the magnetic coupling constants, for example in cases where a complete description of all occupied bands can be achieved using different sets of Wannier functions, e.g., corresponding to different degrees of localization. In the present case, a more systematic analysis is hindered by the strong entanglement of bands and the fact that spread minimization on the full set of Wannier functions leads to orbitals that are not atom-centered. We therefore leave this question open for future research.

[1] J. Paulevé, A. Chamberod, K. Krebs, and A. Bourret, Journal of Applied Physics **39**, 989 (1968).
[2] T. Kojima, M. Mizuguchi, T. Koganezawa, M. Ogiwara, M. Kotsugi, T. Ohtsuki, T.-Y. Tashiro, and K. Takanashi, J. Phys. D Appl. Phys. **47**, 425001 (2014).
[3] L. H. Lewis, F. E. Pinkerton, N. Bordeaux, A. Mubarok, E. Poirier, J. I. Goldstein, R. Skomski, and K. Barmak, IEEE Magnetics Letters **5**, 1 (2014).
[4] L. H. Lewis, A. Mubarok, E. Poirier, N. Bordeaux, P. Manchanda, A. Kashyap, R. Skomski, J. Goldstein, F. E. Pinkerton, R. K. Mishra, R. C. K. Jr, and K. Barmak, Journal of Physics: Condensed Matter **26**, 064213 (2014).
[5] A. Edström, J. Chico, A. Jakobsson, A. Bergman, and J. Rusz, Physical Review B **90**, 014402 (2014).
[6] M. Werwiński and W. Marciniak, Journal of Physics D: Applied Physics **50**, 495008 (2017).
[7] J. Cui, M. Kramer, L. Zhou, F. Liu, A. Gabay, G. Hadjipanayis, B. Balasubramanian, and D. Sellmyer, Acta Materialia **158**, 118 (2018).
[8] L.-Y. Tian, H. Levämäki, O. Eriksson, K. Kokko, Á. Nagy, E. K. Délczeg-Czirják, and L. Vitos, Scientific Reports **9**, 8172 (2019).
[9] L.-Y. Tian, O. Eriksson, and L. Vitos, Scientific Reports **10**, 14766 (2020).
[10] A. Izardar and C. Ederer, Phys. Rev. Materials **4**, 054418 (2020).
[11] L.-Y. Tian, O. Gutfleisch, O. Eriksson, and L. Vitos, Scientific Reports **11**, 5253 (2021).
[12] J. Pauleve, D. Dautreppe, J. Laugier, and L. Néel, J. Phys. Radium **23**, 841 (1962).
[13] L. Néel, J. Pauleve, R. Pauthenet, J. Laugier, and D. Dautreppe, Journal of Applied Physics **35**, 873 (1964).
[14] S. Goto, H. Kura, E. Watanabe, Y. Hayashi, H. Yanagihara, Y. Shimada, M. Mizuguchi, K. Takanashi, and E. Kita, Scientific Reports **7** (2017).
[15] A. Makino, P. Sharma, K. Sato, A. Takeuchi, Y. Zhang, and K. Takenaka", Scientific Reports **5** (2015).
[16] M. Saito, H. Ito, Y. Suzuki, M. Mizuguchi, T. Koganezawa, T. Miyamachi, F. Komori, K. Takanashi, and M. Kotsugi, Applied Physics Letters **114**, 072404 (2019).
[17] T. Kojima, M. Ogiwara, M. Mizuguchi, M. Kotsugi,

T. Koganezawa, T. Ohtsuki, T.-Y. Tashiro, and K. Takanashi, Journal of Physics: Condensed Matter **26**, 064207 (2014).

[18] K. B. Reuter, D. B. Williams, and J. I. Goldstein, Metallurgical Transactions A **20**, 711 (1989).

[19] J. F. Albertsen, J. M. Knudsen, and G. B. Jensen, Nature **273**, 453 (1978).

[20] J. Petersen, M. Aydin, and J. Knudsen, Physics Letters A **62**, 192 (1977).

[21] J. Danon, R. B. Scorzelli, I. S. Azevedo, and M. Christophe-Michel-Lévy, Nature **281**, 469 (1979).

[22] J. Danon, R. B. Scorzelli, I. Souza-Azevedo, J. Laugier, and A. Chamberod, Nature **284**, 537 (1980).

[23] R. S. Clarke and E. R. D. Scott, American Mineralogist **65**, 624 (1980).

[24] S. Onodera, Y. Ishikawa, and K. Tajima, Journal of the Physical Society of Japan **50**, 1513 (1981).

[25] Q. Wei, S. A. Gilder, and B. Maier, Physical Review B **90**, 144425 (2014).

[26] E. D. Santos, J. Gattacceca, P. Rochette, G. Fillion, and R. Scorzelli, Journal of Magnetism and Magnetic Materials **375**, 234 (2015).

[27] P. Soven, Phys. Rev. **156**, 809 (1967).

[28] B. L. Gyorffy, Phys. Rev. B **5**, 2382 (1972).

[29] M. Si, A. Izardar, and C. Ederer, "Effect of chemical disorder on the magnetic anisotropy in L1$_0$ FeNi from first principles calculations," (2021), arXiv:2111.12492 [cond-mat.mtrl-sci].

[30] T. Moriya, *Spin Fluctuations in Itinerant Electron Magnetism* ((Springer-Verlag, Berlin, Heidelberg, 1985).

[31] A. Liechtenstein, M. Katsnelson, V. Antropov, and V. Gubanov, Journal of Magnetism and Magnetic Materials **67**, 65 (1987).

[32] A. N. Rudenko, F. J. Keil, M. I. Katsnelson, and A. I. Lichtenstein, Phys. Rev. B **88**, 081405 (2013).

[33] D. M. Korotin, V. V. Mazurenko, V. I. Anisimov, and S. V. Streltsov, Phys. Rev. B **91**, 224405 (2015).

[34] R. Logemann, A. N. Rudenko, M. I. Katsnelson, and A. Kirilyuk, Journal of Physics: Condensed Matter **29**, 335801 (2017).

[35] X. Zhu, A. Edström, and C. Ederer, Phys. Rev. B **101**, 064401 (2020).

[36] A. A. Mostofi, J. R. Yates, G. Pizzi, Y.-S. Lee, I. Souza, D. Vanderbilt, and N. Marzari, Computer Physics Communications **185**, 2309 (2014).

[37] N. Marzari and D. Vanderbilt, Phys. Rev. B **56**, 12847 (1997).

[38] I. Souza, N. Marzari, and D. Vanderbilt, Physical Review B **65**, 035109 (2001).

[39] G. Kresse and J. Furthmüller, Physical Review B **54**, 11169 (1996).

[40] P. E. Blöchl, Physical Review B **50**, 17953 (1994).

[41] G. Kresse and D. Joubert, Physical Review B **59**, 1758 (1999).

[42] J. P. Perdew, K. Burke, and M. Ernzerhof, Physical Review Letters **77**, 3865 (1996).

[43] B. Skubic, J. Hellsvik, L. Nordström, and O. Eriksson, Journal of Physics: Condensed Matter **20**, 315203 (2008).

[44] D. P. Landau and K. Binder, *A Guide to Monte Carlo Simulations in Statistical Physics*, 4th ed. (Cambridge University Press, 2014).

[45] Note that Tian *et al.* use a different normalization in the Heisenberg model and therefore the absolute values in Ref. 9 are different from ours.

[46] A. S. Belozerov, A. A. Katanin, and V. I. Anisimov, Journal of Physics: Condensed Matter **32**, 385601 (2020).

[47] W. C. Li, X. Song, J. J. Feng, X. T. Jia, M. Zeng, X. S. Gao, and M. H. Qin, Journal of Applied Physics **118**, 013901 (2015).

[48] The small difference to the value of 26.5 meV listed in Fig. 5 is due to the the different unit cells (8-atom cell versus 2-atom cell) used in the calculations.

SUMMARY AND PERSPECTIVE

In this thesis, I present a detailed study on the effect of chemical disorder on the magnetic properties in $L1_0$-FeNi based on first-principles based DFT calculations and Monte-Carlo simulations. In the following, I answer questions that were raised earlier in Chapter 1.

In Chapter 3, I showed that:

- There exists a strong coupling between the magnetic and chemical degrees of freedom in $L1_0$-FeNi. This result which was obtained using the supercell approach is consistent with previous studies employing effective medium type approaches to model the chemical disorder. Furthermore, I showed that the Curie temperature of the chemically disordered structure is lower as compared to that of the fully ordered structure.
- Within the accuracy of our method, the MAE increases with increasing chemical long-range order and reaches its maximal value for $P_z = 0.75$. In other words, a decrease in the chemical disorder by about 25% does not lead to a significant decrease in the MAE relative to the MAE of a fully ordered equiatomic FeNi.
- There exists a linear correlation between the average OMA of Fe atoms and the MAE and this demonstrates that one can use OMA as a proxy to the MAE in order to optimize the MAE in $L1_0$-FeNi.

In Chapter 4, I showed that:

- The analysis of the orbital moment anisotropy of Fe atoms and their corresponding local chemical environment enabled us to identify a favorable first nearest neighbor chemical environment that allowed us to design an optimized Fe-rich structure with an MAE almost two times to that of the fully ordered structure.
- Analysis of the local atomic environment using the SOAP descriptor reveals that there exists only a partial correlation between the local orbital moment anisotropy of Fe atoms and its first nearest neighbors. This correlation vanishes when chemical disorder is introduced.
- One can optimize the MAE in this system by increasing the Fe-content. For the highest considered Fe-content of 62.5%, we obtain the MAE of $93\,\mu$eV/2-atoms (about 25% more than the MAE of the $L1_0$-FeNi).

In Chapter 5, I showed that:

- Effects arising due to the incorporation of the second Hund's rule can have a significant impact on the magnetic properties, in particular, the MAE in $L1_0$-FeNi.

In Chapter 6, I showed that:

- The effects occurring due to the different local chemical environment around a pair of atoms can have significant impact on the magnitude of the magnetic exchange couplings in FeNi.
- Our model study of the Heisenberg model with first nearest neighbors interactions sampled from Gaussian distributions with varying standard deviation indicates that the variation in the magnetic exchange coupling occurring due to the chemical disorder can lead to a reduction in T_c in chemically disordered systems. Thus, one would overestimate the critical temperature in chemically disordered systems if local environment-independent "average" magnetic exchange couplings are used.

The findings in this thesis present new aspects of the important role played by chemical disorder on the magnetic properties in $L1_0$-FeNi. The use of supercells with different distributions of Fe and Ni atoms to model the chemical disorder results in the symmetry-broken local chemical environments around the individual atoms, which is key to understanding the vital role played by such effects on the magnetic properties. Thus, I showed that the effects beyond CPA are necessary to understand the impact of the chemical disorder on the magnetic properties in FeNi. Note that such effects could also play an important role in the accurate estimation of the magnetic properties in other disordered materials. Thus, the research presented in this thesis is an important advancement in our understanding of the magnetic properties in disordered materials, which in turn will allow us to design functional magnetic materials with better performance.

The work performed in my thesis allows to identify routes for future research work. In Chap. 6, we saw that it is extremely challenging to incorporate the information about the variations of the magnetic exchange interaction occurring due to the chemical disorder into a Heisenberg model to obtain the Curie temperature. As a next step, one could employ larger supercells to incorporate the chemical disorder which would allow to sample more different chemical environments and the corresponding magnitude of the exchange couplings. This as a result could allow obtaining an even better estimation of the variation of the Curie temperature as a function of the standard deviation of the magnetic exchange couplings in our model study.

Another research direction could be to focus on further optimizing the MAE in $L1_0$-FeNi. Note that as already mentioned in Sec. 1.3, optimizing the magnetic properties, in particular, the MAE in $L1_0$-FeNi to match with those of rare-earth-based magnets is a very challenging task, since the absence of a rare-earth-element causes a significant loss

of the MAE. However, the MAE could be tuned in FeNi, for example, by alloying with 3d or 5d elements. For this purpose, the computational methods used in this thesis, for example, the supercell approach used to model the distribution of different atomic species should be of great value since it allows to include effects due to the symmetry-broken local environments around the individual atoms which are found to be very important for an accurate estimation of a critical magnetic quantity such as the MAE.

Recently, Wysocki *et al.* [168] considered the formation of $FeNi_{1-x}Co_x$ alloy by substitutional doping of the $L1_0$-FeNi with Co and identified a new ordered phase, $FeNi_{0.5}Co_{0.5}$ with a large MAE of $180\,\mu eV/atom$. In their study, they employed electronic structure calculations along with CPA to model the chemical disorder. One can revisit this study by employing the supercell approach and investigate whether the effects occurring due to the different distribution of the atoms could lead to significant changes in the magnitude of the MAE. Moreover, one can extend this study by alloying the $L1_0$-FeNi with different 3d elements such as Mn, Cr, etc., to study the impact of such dopants on the MAE in this system.

Further optimization of the MAE in $L1_0$-FeNi could be obtained by alloying with 5d elements. Edström *et al.* [169] investigated the effect of adding one atomic percent of 5d impurities (from Lutetium with atomic number 71 until Mercury with atomic number 80) in $L1_0$-FeNi using the SPR-KKR-CPA method. From their calculations, they found that there is a strong increase in the MAE as one goes from Lu to Os and then a rapid decrease as one continues from Os to Hg. One can also revisit this study by employing the supercell approach and investigate whether one gets a similar trend in the MAE across the series. Note that while in this study a low dopant concentration was considered, a further increase in the MAE could be obtained by increasing the concentration of 5d dopants.

In Chap. 4, we saw that the SOAP descriptor of the local chemical environment is able to reveal only a partial correlation between the local orbital moment anisotropy of Fe atoms and its nearest neighbors. One could investigate this further by using a different descriptor e.g., atomic cluster expansion [170] of the local atomic environment to better understand this correlation.

Finally, to conclude, with the different routes described above, there seems to be no physical limitation that could hinder from optimizing the properties of $L1_0$-FeNi in order to reach a performance closer to that of the rare-earth-based magnets.

BIBLIOGRAPHY

[1] Ankit Izardar and Claude Ederer. "Interplay between chemical order and magnetic properties in $L1_0$ FeNi (tetrataenite): A first-principles study." In: *Phys. Rev. Materials* 4 (2020), p. 054418. DOI: 10.1103/PhysRevMaterials.4.054418.

[2] Mayan Si, Ankit Izardar, and Claude Ederer. "Effect of chemical disorder on the magnetic anisotropy in $L1_0$ FeNi from first principles calculations." In: *ArXiv e-prints* (2021). eprint: 2111.12492 (cond-mat.mtrl-sci).

[3] Ankit Izardar and Claude Ederer. "Impact of chemical disorder on magnetic exchange interactions in $L1_0$-FeNi (tetrataenite)." In: *ArXiv e-prints* (2022). eprint: 2203.00640 (cond-mat.mtrl-sci).

[4] K. Strnat, G. Hoffer, J. Olson, W. Ostertag, and J. J. Becker. "A Family of New Cobalt-Base Permanent Magnet Materials." In: *Journal of Applied Physics* 38.3 (1967), pp. 1001–1002. DOI: 10.1063/1.1709459.

[5] G. Hoffer and K. Strnat. "Magnetocrystalline Anisotropy of Two Yttriu-Cobalt Compounds." In: *Journal of Applied Physics* 38.3 (1967), pp. 1377–1378. DOI: 10.1063/1.1709630.

[6] K.J. Strnat. "The Recent Development of Permanent Magnet Materials Containing Rare Earth Metals." In: *IEEE Transactions on Magnetics* 6.2 (1970), pp. 182–190. DOI: 10.1109/TMAG.1970.1066743.

[7] J.F. Liu, Y. Zhang, D. Dimitrov, and G.C. Hadjipanayis. "Microstructure and high temperature magnetic properties of $Sm(Co, Cu, Fe, Zr)_z$ ($z = 6.7$-9.1) permanent magnets." In: *Journal of Applied Physics* 85.5 (1999), pp. 2800–2804. DOI: 10.1063/1.369597.

[8] J. J. Croat, J. F. Herbst, R. W. Lee, and F. E. Pinkerton. "Pr-Fe and Nd-Fe-based materials: A new class of high-performance permanent magnets (invited)." In: *Journal of Applied Physics* 55.6 (1984), pp. 2078–2082. DOI: 10.1063/1.333571.

[9] J. F. Herbst. "$R_2Fe_{14}B$ materials: Intrinsic properties and technological aspects." In: *Rev. Mod. Phys.* 63 (1991), pp. 819–898. DOI: 10.1103/RevModPhys.63.819.

[10] M. Sagawa, S. Fujimura, N. Togawa, H. Yamamoto, and Y. Matsuura. "New material for permanent magnets on a base of Nd and Fe (invited)." In: *Journal of Applied Physics* 55.6 (1984), pp. 2083–2087. DOI: 10.1063/1.333572.

[11] Oliver Gutfleisch et al. "Magnetic Materials and Devices for the 21st Century: Stronger, Lighter, and More Energy Efficient." In: *Advanced Materials* 23.7 (2011), pp. 821–842. DOI: https://doi.org/10.1002/adma.201002180.

[12] T. Folger. *National Geographic Magazine.* June 2011. URL: https://www.nationalgeographic.com/magazine/2011/06/rare-earth-elements/.

[13] K. Bourzac. *MIT Technology Review.* 2011. URL: https://www.technologyreview.com/s/423730/the-rare-earth-crisis/.

[14] Karen Smith Stegen. "Heavy rare earths, permanent magnets, and renewable energies: An imminent crisis." In: *Energy Policy* 79 (2015), pp. 1–8. DOI: https://doi.org/10.1016/j.enpol.2014.12.015.

[15] R.W. McCallum, L.H. Lewis, R. Skomski, M.J. Kramer, and I.E. Anderson. "Practical Aspects of Modern and Future Permanent Magnets." In: *Annual Review of Materials Research* 44.1 (2014), pp. 451–477. DOI: 10.1146/annurev-matsci-070813-113457.

[16] L.H. Lewis and F. Jimenez-Villacorta. "Perspectives on Permanent Magnetic Materials for Energy Conversion and Power Generation." In: *Metallurgical and Materials Transactions A* 44A (2012). DOI: 10.1007/s11661-012-1278-2.

[17] Karl-Hartmut Müller, Simon Sawatzki, Roland Gauß, and Oliver Gutfleisch. "Permanent Magnet Materials." In: *Handbook of Magnetism and Magnetic Materials.* Cham: Springer International Publishing, 2020, pp. 1–65. ISBN: 978-3-030-63101-7. DOI: 10.1007/978-3-030-63101-7_29-1.

[18] European Commission, Study on the EU's list of Critical Raw Materials – Final Report (2020). DOI: 10.2873/11619.

[19] Sveriges Geologiska Undersökning (SGU). Metallprisutveckling 11, 2015.

[20] Manuel Richter. "Band structure theory of magnetism in 3d-4f compounds." In: *Journal of Physics D: Applied Physics* 31.9 (1998), pp. 1017–1048. DOI: 10.1088/0022-3727/31/9/002.

[21] J.M.D. Coey. "Permanent magnets: Plugging the gap." In: *Scripta Materialia* 67.6 (2012), pp. 524–529. DOI: https://doi.org/10.1016/j.scriptamat.2012.04.036.

[22] G. Couderchon and J.F. Tiers. "Some aspects of magnetic properties of Ni-Fe and Co-Fe alloys." In: *Journal of Magnetism and Magnetic Materials* 26.1 (1982), pp. 196–214. DOI: https://doi.org/10.1016/0304-8853(82)90152-4.

[23] J M D Coey. "New permanent magnets manganese compounds." In: *Journal of Physics: Condensed Matter* 26.6 (2014), p. 064211. DOI: 10.1088/0953-8984/26/6/064211.

[24] A. J. J. Koch, P. Hokkeling, M. G. v. d. Steeg, and K. J. de Vos. "New Material for Permanent Magnets on a Base of Mn and Al." In: *Journal of Applied Physics* 31.5 (1960), S75–S77. DOI: 10.1063/1.1984610.

[25] J. H. Park et al. "Saturation magnetization and crystalline anisotropy calculations for MnAl permanent magnet." In: *Journal of Applied Physics* 107.9 (2010), 09A731. DOI: 10.1063/1.3337640.

[26] S. H. Nie et al. "Perpendicularly magnetized -MnAl (001) thin films epitaxied on GaAs." In: *Applied Physics Letters* 102.15 (2013), p. 152405. DOI: 10.1063/1.4801932.

[27] Y. Kinemuchi, A. Fujita, and K. Ozaki. "High-pressure synthesis of L10 MnAl with near-stoichiometric composition." In: *Dalton Trans.* 45 (2016), pp. 10936–10941. DOI: 10.1039/C6DT00947F.

[28] Akimasa Sakuma. "Electronic structures and magnetism of CuAu-type MnNi and MnGa." In: *Journal of Magnetism and Magnetic Materials* 187.1 (1998), pp. 105–112. DOI: https://doi.org/10.1016/S0304-8853(98)00115-2.

[29] Erdong Lu, David C. Ingram, Arthur R. Smith, J. W. Knepper, and F. Y. Yang. "Reconstruction Control of Magnetic Properties during Epitaxial Growth of Ferromagnetic $Mn_{3-\delta}Ga$ on Wurtzite GaN(0001)." In: *Phys. Rev. Lett.* 97 (2006), p. 146101. DOI: 10.1103/PhysRevLett.97.146101.

[30] Kangkang Wang, Erdong Lu, Jacob W. Knepper, Fengyuan Yang, and Arthur R. Smith. "Structural controlled magnetic anisotropy in Heusler L10MnGa epitaxial thin films." In: *Applied Physics Letters* 98.16 (2011), p. 162507. DOI: 10.1063/1.3582244.

[31] H. Kurt, K. Rode, M. Venkatesan, P. Stamenov, and J. M. D. Coey. "$Mn_{3-x}Ga$ ($0 \leq x \leq 1$): Multifunctional thin film materials for spintronics and magnetic recording." In: *physica status solidi (b)* 248.10 (2011), pp. 2338–2344. DOI: https://doi.org/10.1002/pssb.201147122.

[32] D. P. Hoydick, E. J. Palmiere, and W. A. Soffa. "Microstructural development in MnAl-base permanent magnet materials: New perspectives." In: *Journal of Applied Physics* 81.8 (1997), pp. 5624–5626. DOI: 10.1063/1.364619.

[33] Z.C. Yan et al. "Magnetic and structural properties of MnAl/Ag granular thin films with $L1_0$ structure." In: *Scripta Materialia* 53.4 (2005), pp. 463–468. DOI: https://doi.org/10.1016/j.scriptamat.2005.04.045.

[34] J. Z. Wei et al. "τ-MnAl with high coercivity and saturation magnetization." In: *AIP Advances* 4.12 (2014), p. 127113. DOI: 10.1063/1.4903773.

[35] J.-U. Thiele, L. Folks, M. F. Toney, and D. K. Weller. "Perpendicular magnetic anisotropy and magnetic domain structure in sputtered epitaxial FePt (001) L1$_0$ films." In: *Journal of Applied Physics* 84.10 (1998), pp. 5686–5692. DOI: 10.1063/1.368831.

[36] Shouheng Sun, C. B. Murray, Dieter Weller, Liesl Folks, and Andreas Moser. "Monodisperse FePt Nanoparticles and Ferromagnetic FePt Nanocrystal Superlattices." In: *Science* 287.5460 (2000), pp. 1989–1992. DOI: 10.1126/science.287.5460.1989.

[37] J Zhou et al. "Permanent-magnet properties of thermally processed FePt and FePt-Fe multilayer films." In: *IEEE Transactions on Magnetics* 38.5, 1 (2002), 2802–2804. DOI: 10.1109/TMAG.2002.803109.

[38] Balachandran Jeyadevan et al. "Direct Synthesis of fct-FePt Nanoparticles by Chemical Route." In: *Japanese Journal of Applied Physics* 42 (2003), pp. L350–L352. DOI: 10.1143/jjap.42.1350.

[39] Shouheng Sun et al. "Controlled Synthesis and Assembly of FePt Nanoparticles." In: *The Journal of Physical Chemistry B* 107.23 (2003), pp. 5419–5425. DOI: 10.1021/jp027314o.

[40] O. Gutfleisch, J. Lyubina, KH. Muller, and L. Schultz. "FePt hard magnets." In: *Advanced Engineering Materials* 7.4 (2005), 208–212. DOI: 10.1002/adem.200400183.

[41] Kevin E. Elkins, Girija S. Chaubey, Vikas Nandwana, and J.Ping Liu. "A Novel Approach to Synthesis of FePt Magnetic Nanoparticles." In: *Journal of Nano Research* 1 (2007), pp. 23–30. DOI: 10.4028/www.scientific.net/JNanoR.1.23.

[42] Weiwei Yang et al. "From FePt–Fe$_3$O$_4$ to L1$_0$-FePt–Fe nanocomposite magnets with a gradient interface." In: *J. Mater. Chem. C* 3 (2015), pp. 7075–7080. DOI: 10.1039/C5TC01145K.

[43] M. Pousthomis et al. "On the advantages of spring magnets compared to pure FePt: Strategy for rare-earth free permanent magnets following a bottom-up approach." In: *Journal of Magnetism and Magnetic Materials* 424 (2017), 304–313. DOI: 10.1016/j.jmmm.2016.10.071.

[44] Frank M. Abel et al. "Enhancing the Ordering and Coercivity of L10 FePt Nanostructures with Bismuth Additives for Applications Ranging from Permanent Magnets to Catalysts." In: *ACS Applied Nano Materials* 2.5 (2019), pp. 3146–3153. DOI: 10.1021/acsanm.9b00463.

[45]   Till Burkert, Lars Nordström, Olle Eriksson, and Olle Heinonen. "Giant Magnetic Anisotropy in Tetragonal FeCo Alloys." In: *Phys. Rev. Lett.* 93 (2004), p. 027203. DOI: 10 . 1103 / PhysRevLett.93.027203.

[46]   Gabriella Andersson et al. "Perpendicular Magnetocrystalline Anisotropy in Tetragonally Distorted Fe-Co Alloys." In: *Phys. Rev. Lett.* 96 (2006), p. 037205. DOI: 10.1103/PhysRevLett.96. 037205.

[47]   Jun Cui et al. "Current progress and future challenges in rare-earth-free permanent magnets." In: *Acta Materialia* 158 (2018), pp. 118–137. DOI: https://doi.org/10.1016/j.actamat. 2018.07.049.

[48]   K.P. Skokov and O. Gutfleisch. "Heavy rare earth free, free rare earth and rare earth free magnets - Vision and reality." In: *Scripta Materialia* 154 (2018), pp. 289–294. DOI: https : //doi.org/10.1016/j.scriptamat.2018.01.032.

[49]   Filip Ronning and Sam Bader. "Rare earth replacement magnets." In: *Journal of Physics: Condensed Matter* (2014).

[50]   Zefan Shao and Shenqiang Ren. "Rare-earth-free magnetically hard ferrous materials." In: *Nanoscale Adv.* 2 (2020), pp. 4341–4349. DOI: 10.1039/D0NA00519C.

[51]   Paulevé, J., Dautreppe, D., Laugier, J., and Néel, L. "Une nouvelle transition ordre-désordre dans Fe-Ni (50-50)." In: *J. Phys. Radium* 23.10 (1962), pp. 841–843. DOI: 10.1051/jphysrad: 019620023010084100.

[52]   J.F. Petersen, M. Aydin, and J.M. Knudsen. "Mössbauer spectroscopy of an ordered phase (superstructure) of FeNi in an iron meteorite." In: *Physics Letters A* 62.3 (1977), pp. 192 –194. DOI: https://doi.org/10.1016/0375-9601(77)90023-8.

[53]   J. F. Albertsen, J. M. Knudsen, and G. B. Jensen. "Structure of taenite in two iron meteorites." In: *Nature* 273.5662 (1978), pp. 453–454. DOI: 10.1038/273453a0.

[54]   J. Danon, R. B. Scorzelli, I. Souza Azevedo, and M. Christophe-Michel-Lévy. "Iron-nickel superstructure in metal particles of chondrites." In: *Nature* 281.5731 (1979), pp. 469–471. DOI: 10. 1038/281469a0.

[55]   J. Danon, R. B. Scorzelli, I. Souza-Azevedo, J. Laugier, and A. Chamberod. "Santa Catharina meteorite and phase composition of irradiated Fe-Ni Invar alloys." In: *Nature* 284.5756 (1980), pp. 537–538. DOI: 10.1038/284537a0.

[56]   Roy S. Clarke and Edward R. D. Scott. "Tetrataenite-ordered FeNi, a new mineral in meteorites." In: *American Mineralogist* 65.7-8 (1980), pp. 624–630.

[57] L. H. Lewis et al. "De Magnete et Meteorite: Cosmically Motivated Materials." In: *IEEE Magnetics Letters* 5 (2014), pp. 1–4. DOI: 10.1109/LMAG.2014.2312178.

[58] J. Paulevé, A. Chamberod, K. Krebs, and A. Bourret. "Magnetization Curves of Fe-Ni (50-50) Single Crystals Ordered by Neutron Irradiation with an Applied Magnetic Field." In: *Journal of Applied Physics* 39.2 (1968), pp. 989–990. DOI: 10.1063/1.1656361.

[59] T. Kojima et al. "Addition of Co to $L1_0$-ordered FeNi films: influences on magnetic properties and ordered structures." In: *Journal of Physics D Applied Physics* 47, 425001 (2014), p. 425001. DOI: 10.1088/0022-3727/47/42/425001.

[60] L. H. Lewis et al. "Inspired by nature: investigating tetrataenite for permanent magnet applications." In: 26.6 (2014), p. 064213. DOI: 10.1088/0953-8984/26/6/064213.

[61] C.W. Yang, D.B. Williams, and J.I. Goldstein. "Low-temperature phase decomposition in metal from iron, stony-iron, and stony meteorites." In: *Geochimica et Cosmochimica Acta* 61.14 (1997), pp. 2943 –2956. DOI: 10.1016/S0016-7037(97)00132-4.

[62] L. Néel, J. Pauleve, R. Pauthenet, J. Laugier, and D. Dautreppe. "Magnetic Properties of an Iron-Nickel Single Crystal Ordered by Neutron Bombardment." In: *Journal of Applied Physics* 35.3 (1964), pp. 873–876. DOI: 10.1063/1.1713516.

[63] E. Dos Santos, J. Gattacceca, P. Rochette, G. Fillion, and R.B. Scorzelli. "Kinetics of tetrataenite disordering." In: *Journal of Magnetism and Magnetic Materials* 375 (2015), pp. 234 –241. DOI: https://doi.org/10.1016/j.jmmm.2014.09.051.

[64] R.B. Scorzelli. "A study of phase stability in invar Fe–Ni alloys obtained by non-conventional methods." In: *Hyperfine Interactions* 110.1 (1997), pp. 143–150. DOI: 10.1023/A:1012679517295.

[65] Sho Goto et al. "Synthesis of single-phase L10-FeNi magnet powder by nitrogen insertion and topotactic extraction." In: *Scientific Reports* 7.1 (2017). DOI: 10.1038/s41598-017-13562-2.

[66] Takahiro Nishio, Hiroaki Kura, Keita Ito, Koki Takanashi, and Hideto Yanagihara. "Fabrication of L10-FeNi films with island structures by nitrogen insertion and topotactic extraction for improved coercivity." In: *APL Materials* 9.9 (2021), p. 091108. DOI: 10.1063/5.0062692.

[67] Akihiro Makino et al. "Artificially produced rare-earth free cosmic magnet." In: *Scientific Reports* 5 (2015). DOI: 10.1038/srep16627.

[68]   Masahiro Saito et al. "Fabrication of L1$_0$-FeNi by pulsed-laser deposition." In: *Applied Physics Letters* 114.7 (2019), p. 072404. DOI: 10.1063/1.5087041.

[69]   Takayuki Kojima et al. "Magnetic Anisotropy and Chemical Order of Artificially Synthesized L1$_0$-Ordered FeNi Films on Au–Cu–Ni Buffer Layers." In: *Japanese Journal of Applied Physics* 51.1 (2011), p. 010204. DOI: 10.1143/jjap.51.010204.

[70]   M.-Z. Dang and D. G. Rancourt. "Simultaneous magnetic and chemical order-disorder phenomena in Fe$_3$Ni, FeNi, and FeNi$_3$." In: *Physical Review B* 53 (1996), pp. 2291–2302. DOI: 10.1103/PhysRevB.53.2291.

[71]   M. Yu. Lavrentiev, J. S. Wróbel, D. Nguyen-Manh, and S. L. Dudarev. "Magnetic and thermodynamic properties of face-centered cubic Fe–Ni alloys." In: *Physical Chemistry Chemical Physics* 16 (2014), pp. 16049–16059. DOI: 10.1039/C4CP01366B.

[72]   Li-Yun Tian et al. "Density Functional Theory description of the order-disorder transformation in Fe-Ni." In: *Scientific Reports* 9.1 (2019), p. 8172. DOI: 10.1038/s41598-019-44506-7.

[73]   Yoshio Miura et al. "The origin of perpendicular magneto-crystalline anisotropy in L1$_0$–FeNi under tetragonal distortion." In: *Journal of Physics: Condensed Matter* 25.10 (2013), p. 106005. DOI: 10.1088/0953-8984/25/10/106005.

[74]   Alexander Edström, Jonathan Chico, Adam Jakobsson, Anders Bergman, and Jan Rusz. "Electronic structure and magnetic properties of L1$_0$ binary alloys." In: *Physical Review B* 90.1 (2014), p. 014402. DOI: 10.1103/PhysRevB.90.014402.

[75]   Paul Soven. "Coherent-Potential Model of Substitutional Disordered Alloys." In: *Phys. Rev.* 156 (1967), pp. 809–813. DOI: 10.1103/PhysRev.156.809.

[76]   B. L. Gyorffy. "Coherent-Potential Approximation for a Nonoverlapping-Muffin-Tin-Potential Model of Random Substitutional Alloys." In: *Phys. Rev. B* 5 (1972), pp. 2382–2384. DOI: 10.1103/PhysRevB.5.2382.

[77]   Takayuki Kojima et al. "Fe–Ni composition dependence of magnetic anisotropy in artificially fabricated L1$_0$-ordered FeNi films." In: 26.6 (2014), p. 064207. DOI: 10.1088/0953-8984/26/6/064207.

[78]   F. Giustino. *Materials modelling using Density Functional Theory.* Oxford University Press, 2014. ISBN: 9780199662432.

[79]   Joachim Stöhr and Hans Christoph Siegmann. *Magnetism.* Springer Berlin Heidelberg, 2006. DOI: 10.1007/978-3-540-30283-4.

[80]   Nicola A. Spaldin. *Magnetic Materials: Fundamentals and Applications.* 2nd ed. Cambridge University Press, 2010. DOI: 10.1017/CBO9780511781599.

[81]   Burak Himmetoglu, Andrea Floris, Stefano de Gironcoli, and Matteo Cococcioni. "Hubbard-corrected DFT energy functionals: The LDA+U description of correlated systems." In: *International Journal of Quantum Chemistry* 114.1 (2014), pp. 14–49. DOI: https://doi.org/10.1002/qua.24521.

[82]   M. Born and R. Oppenheimer. "Zur Quantentheorie der Molekeln." In: *Ann. Phys.* 84 (1927), pp. 457–484. DOI: 10.1002/andp.19273892002.

[83]   P. Hohenberg and W. Kohn. "Inhomogeneous Electron Gas." In: *Phys. Rev.* 136 (1964), B864–B871. DOI: 10.1103/PhysRev.136.B864.

[84]   W. Kohn and L. J. Sham. "Self-Consistent Equations Including Exchange and Correlation Effects." In: *Phys. Rev.* 140 (1965), A1133–A1138.

[85]   P. A. M. Dirac. "Note on Exchange Phenomena in the Thomas Atom." In: *Mathematical Proceedings of the Cambridge Philosophical Society* 26.3 (1930), 376–385. DOI: 10.1017/S0305004100016108.

[86]   J. C. Slater. "A Simplification of the Hartree-Fock Method." In: *Phys. Rev.* 81 (1951), pp. 385–390. DOI: 10.1103/PhysRev.81.385.

[87]   D. M. Ceperley and B. J. Alder. "Ground State of the Electron Gas by a Stochastic Method." In: *Phys. Rev. Lett.* 45 (1980), pp. 566–569. DOI: 10.1103/PhysRevLett.45.566.

[88]   J. P. Perdew and Alex Zunger. "Self-interaction correction to density-functional approximations for many-electron systems." In: *Phys. Rev. B* 23 (1981), pp. 5048–5079. DOI: 10.1103/PhysRevB.23.5048.

[89]   Jing Zhu, X. W. Wang, and Steven G. Louie. "First-principles pseudopotential calculations of magnetic iron." In: *Phys. Rev. B* 45 (1992), pp. 8887–8893. DOI: 10.1103/PhysRevB.45.8887.

[90]   John P. Perdew et al. "Atoms, molecules, solids, and surfaces: Applications of the generalized gradient approximation for exchange and correlation." In: *Phys. Rev. B* 46 (1992), pp. 6671–6687. DOI: 10.1103/PhysRevB.46.6671.

[91]   J. P. Perdew, K. Burke, and M. Ernzerhof. "Generalized Gradient Approximation Made Simple." In: *Phys. Rev. Lett.* 77 (1996), p. 3865. DOI: 10.1103/PhysRevLett.77.3865.

[92]   J. Kohanoff. *Electronic Structure Calculations for Solids and Molecules.* Cambridge University Press, 2006. ISBN: 9780521815918.

[93]   P. E. Blöchl. "Projector augmented-wave method." In: *Phys. Rev. B* 50 (1994), pp. 17953–17979. DOI: `10.1103/PhysRevB.50.17953`.

[94]   G. Kresse and J. Furthmüller. "Efficient iterative schemes for ab initio total-energy calculations using a plane-wave basis set." In: *Phys. Rev. B* 54 (1996), p. 11169. DOI: `10.1103/PhysRevB.54.11169`.

[95]   G. Kresse and D. Joubert. "From ultrasoft pseudopotentials to the projector augmented-wave method." In: *Phys. Rev. B* 59 (1999), pp. 1758–1775. DOI: `10.1103/PhysRevB.59.1758`.

[96]   Antoine Georges and Gabriel Kotliar. "Hubbard model in infinite dimensions." In: *Phys. Rev. B* 45 (1992), pp. 6479–6483. DOI: `10.1103/PhysRevB.45.6479`.

[97]   Antoine Georges, Gabriel Kotliar, Werner Krauth, and Marcelo J. Rozenberg. "Dynamical mean-field theory of strongly correlated fermion systems and the limit of infinite dimensions." In: *Rev. Mod. Phys.* 68 (1996), pp. 13–125. DOI: `10.1103/RevModPhys.68.13`.

[98]   S. Sharma, J. K. Dewhurst, N. N. Lathiotakis, and E. K. U. Gross. "Reduced density matrix functional for many-electron systems." In: *Phys. Rev. B* 78 (2008), p. 201103. DOI: `10.1103/PhysRevB.78.201103`.

[99]   Vladimir I. Anisimov, Jan Zaanen, and Ole K. Andersen. "Band theory and Mott insulators: Hubbard U instead of Stoner I." In: *Phys. Rev. B* 44 (1991), pp. 943–954. DOI: `10.1103/PhysRevB.44.943`.

[100] V. I. Anisimov, I. V. Solovyev, M. A. Korotin, and G. A. Sawatzky. "Density-functional theory and NiO photoemission spectra." In: *Phys. Rev. B* 48 (1993), pp. 16929–16934. DOI: `10.1103/PhysRevB.48.16929`.

[101] A. I. Liechtenstein, V. I. Anisimov, and J. Zaanen. "Density-functional theory and strong interactions: Orbital ordering in Mott-Hubbard insulators." In: *Phys. Rev. B* 52 (1995), R5467–R5470. DOI: `10.1103/PhysRevB.52.R5467`.

[102] V. I. Anisimov, F. Aryasetiawan, and A. I. Lichtenstein. "First-principles calculations of the electronic structure and spectra of strongly correlated systems: the LDA+U method." In: *Journal of Physics: Condensed Matter* 9.4 (1997), pp. 767–808. DOI: `10.1088/0953-8984/9/4/002`.

[103]   Martin C. Gutzwiller. "Effect of Correlation on the Ferromagnetism of Transition Metals." In: *Phys. Rev. Lett.* 10 (1963), pp. 159–162. DOI: 10.1103/PhysRevLett.10.159.

[104]   Junjiro Kanamori. "Electron Correlation and Ferromagnetism of Transition Metals." In: *Progress of Theoretical Physics* 30.3 (1963), pp. 275–289. DOI: 10.1143/PTP.30.275.

[105]   J. Hubbard. "Electron correlations in narrow energy bands." In: *Proceedings of the Royal Society of London. Series A. Mathematical and Physical Sciences* 276.1365 (1963), pp. 238–257. DOI: 10.1098/rspa.1963.0204.

[106]   J. Hubbard. "Electron correlations in narrow energy bands III. An improved solution." In: *Proceedings of the Royal Society of London. Series A. Mathematical and Physical Sciences* 281.1386 (1964), pp. 401–419. DOI: 10.1098/rspa.1964.0190.

[107]   M. T. Czyzzyk and G. A. Sawatzky. "Local-density functional and on-site correlations: The electronic structure of La_2CuO_4 and $LaCuO_3$." In: *Phys. Rev. B* 49 (1994), pp. 14211–14228. DOI: 10.1103/PhysRevB.49.14211.

[108]   A. G. Petukhov, I. I. Mazin, L. Chioncel, and A. I. Lichtenstein. "Correlated metals and the $LDA + U$ method." In: *Phys. Rev. B* 67 (2003), p. 153106. DOI: 10.1103/PhysRevB.67.153106.

[109]   V. I. Anisimov, A. V. Kozhevnikov, M. A. Korotin, A. V. Lukoyanov, and D. A. Khafizullin. "Orbital density functional as a means to restore the discontinuities in the total-energy derivative and the exchange–correlation potential." In: *Journal of Physics: Condensed Matter* 19.10 (2007), p. 106206. DOI: 10.1088/0953-8984/19/10/106206.

[110]   A. I. Liechtenstein, V. I. Anisimov, and J. Zaanen. "Density-functional theory and strong interactions: Orbital ordering in Mott-Hubbard insulators." In: *Phys. Rev. B* 52 (1995), R5467–R5470. DOI: 10.1103/PhysRevB.52.R5467.

[111]   S. L. Dudarev, G. A. Botton, S. Y. Savrasov, C. J. Humphreys, and A. P. Sutton. "Electron-energy-loss spectra and the structural stability of nickel oxide: An LSDA+U study." In: *Phys. Rev. B* 57 (1998), pp. 1505–1509. DOI: 10.1103/PhysRevB.48.16929.

[112]   I. V. Solovyev, A. I. Liechtenstein, and K. Terakura. "Is Hund's Second Rule Responsible for the Orbital Magnetism in Solids?" In: *Phys. Rev. Lett.* 80 (1998), pp. 5758–5761. DOI: 10.1103/PhysRevLett.80.5758.

[113]   Fredrik Bultmark, Francesco Cricchio, Oscar Grånäs, and Lars Nordström. "Multipole decomposition of $LDA + U$ energy and its application to actinide compounds." In: *Phys. Rev. B* 80 (2009), p. 035121. DOI: 10.1103/PhysRevB.80.035121.

[114]   J. M. D. Coey. *Magnetism and Magnetic Materials*. Vol. 48. Cambridge University Press, 2010, pp. 16929–16934. DOI: `10.1017/CBO9780511845000`.

[115]   J. H. van Vleck. "On the Anisotropy of Cubic Ferromagnetic Crystals." In: *Phys. Rev.* 52 (1937), pp. 1178–1198. DOI: `10.1103/PhysRev.52.1178`.

[116]   Patrick Bruno. "Tight-binding approach to the orbital magnetic moment and magnetocrystalline anisotropy of transition-metal monolayers." In: *Physical Review B* 39 (1989), pp. 865–868. DOI: `10.1103/PhysRevB.39.865`.

[117]   C. Andersson et al. "Influence of Ligand States on the Relationship between Orbital Moment and Magnetocrystalline Anisotropy." In: *Phys. Rev. Lett.* 99 (2007), p. 177207. DOI: `10.1103/PhysRevLett.99.177207`.

[118]   M. Weinert, R. E. Watson, and J. W. Davenport. "Total-energy differences and eigenvalue sums." In: *Phys. Rev. B* 32 (1985), pp. 2115–2119. DOI: `10.1103/PhysRevB.32.2115`.

[119]   G. H. O. Daalderop, P. J. Kelly, and M. F. H. Schuurmans. "First-principles calculation of the magnetocrystalline anisotropy energy of iron, cobalt, and nickel." In: *Phys. Rev. B* 41 (1990), pp. 11919–11937. DOI: `10.1103/PhysRevB.41.11919`.

[120]   J. Trygg, B. Johansson, O. Eriksson, and J. M. Wills. "Total Energy Calculation of the Magnetocrystalline Anisotropy Energy in the Ferromagnetic 3d Metals." In: *Phys. Rev. Lett.* 75 (1995), pp. 2871–2874. DOI: `10.1103/PhysRevLett.75.2871`.

[121]   Xindong Wang, Ding sheng Wang, Ruqian Wu, and A.J. Freeman. "Validity of the force theorem for magnetocrystalline anisotropy." In: *Journal of Magnetism and Magnetic Materials* 159.3 (1996), pp. 337–341. DOI: `https://doi.org/10.1016/0304-8853(95)00936-1`.

[122]   M Blanco-Rey, J I Cerdá, and A Arnau. "Validity of perturbative methods to treat the spin–orbit interaction: application to magnetocrystalline anisotropy." In: *New Journal of Physics* 21.7 (2019), p. 073054. DOI: `10.1088/1367-2630/ab3060`.

[123]   W. Heisenberg. "On the theory of ferromagnetism." In: *Z. Physik* 49 (1928), p. 619. DOI: `10.1103/PhysRevB.48.16929`.

[124]   H. J. Xiang, E. J. Kan, Su-Huai Wei, M.-H. Whangbo, and X. G. Gong. "Predicting the spin-lattice order of frustrated systems from first principles." In: *Phys. Rev. B* 84 (2011), p. 224429. DOI: `10.1103/PhysRevB.84.224429`.

[125]   T. Moriya. *Spin Fluctuations in Itinerant Electron Magnetism*. Vol. 48. Springer-Verlag, Berlin, Heidelberg, 1985, pp. 16929–16934. DOI: `10.1103/PhysRevB.48.16929`.

[126] A.I. Liechtenstein, M.I. Katsnelson, V.P. Antropov, and V.A. Gubanov. "Local spin density functional approach to the theory of exchange interactions in ferromagnetic metals and alloys." In: *Journal of Magnetism and Magnetic Materials* 67.1 (1987), pp. 65 –74. DOI: https://doi.org/10.1016/0304-8853(87)90721-9.

[127] A. N. Rudenko, F. J. Keil, M. I. Katsnelson, and A. I. Lichtenstein. "Exchange interactions and frustrated magnetism in single-side hydrogenated and fluorinated graphene." In: *Phys. Rev. B* 88 (2013), p. 081405. DOI: 10.1103/PhysRevB.88.081405.

[128] Dm. M. Korotin, V. V. Mazurenko, V. I. Anisimov, and S. V. Streltsov. "Calculation of exchange constants of the Heisenberg model in plane-wave-based methods using the Green's function approach." In: *Phys. Rev. B* 91 (2015), p. 224405. DOI: 10.1103/PhysRevB.91.224405.

[129] R. Logemann, A. N. Rudenko, M. I. Katsnelson, and A. Kirilyuk. "Exchange interactions in transition metal oxides: the role of oxygen spin polarization." In: *Journal of Physics: Condensed Matter* 29.33 (2017), p. 335801. DOI: 10.1088/1361-648x/aa7b00.

[130] Xiangzhou Zhu, Alexander Edström, and Claude Ederer. "Magnetic exchange interactions in $SrMnO_3$." In: *Phys. Rev. B* 101 (2020), p. 064401. DOI: 10.1103/PhysRevB.101.064401.

[131] Xiangzhou Zhu, Alexander Edström, and Ankit Izardar. *W2ij.* 2021. DOI: https://github.com/materialstheory/L10-FeNi/tree/main/W2ij.

[132] Nicola Marzari and David Vanderbilt. "Maximally localized generalized Wannier functions for composite energy bands." In: *Phys. Rev. B* 56 (20 1997), pp. 12847–12865. DOI: 10.1103/PhysRevB.56.12847.

[133] Nicola Marzari, Arash A. Mostofi, Jonathan R. Yates, Ivo Souza, and David Vanderbilt. "Maximally localized Wannier functions: Theory and applications." In: *Rev. Mod. Phys.* 84 (4 2012), pp. 1419–1475. DOI: 10.1103/RevModPhys.84.1419.

[134] Charles Kittel. *Introduction to Solid State Physics.* 6th. Vol. 48. New York: John Wiley & Sons, Inc., 1986, pp. 16929–16934. DOI: 10.1103/PhysRevB.48.16929.

[135] Ankit Izardar. *Disorder supercell Generator.* 2021. DOI: https://github.com/materialstheory/L10-FeNi/blob/main/Python-Scripts/disorder_supercell_generator.py.

[136] Albert P. Bartók, Risi Kondor, and Gábor Csányi. "On representing chemical environments." In: *Phys. Rev. B* 87 (2013), p. 184115. DOI: 10.1103/PhysRevB.87.184115.

[137] Karl Pearson F.R.S. "LIII. On lines and planes of closest fit to systems of points in space." In: *The London, Edinburgh, and Dublin Philosophical Magazine and Journal of Science* 2.11 (1901), pp. 559–572. DOI: 10.1080/14786440109462720.

[138] Ian T Jolliffe. *Principal component analysis for special types of data.* Vol. 48. Springer, 2002, pp. 16929–16934. DOI: 10.1103/PhysRevB.48.16929.

[139] Ian T. Jolliffe and Jorge Cadima. "Principal component analysis: a review and recent developments." In: *Philosophical Transactions of the Royal Society A: Mathematical, Physical and Engineering Sciences* 374.2065 (2016), p. 20150202. DOI: 10.1098/rsta.2015.0202.

[140] Joshua B. Tenenbaum, Vin de Silva, and John C. Langford. "A Global Geometric Framework for Nonlinear Dimensionality Reduction." In: *Science* 290.5500 (2000), pp. 2319–2323. DOI: 10.1126/science.290.5500.2319.

[141] Bernhard Schölkopf, Alexander Smola, and Klaus-Robert Müller. "Nonlinear Component Analysis as a Kernel Eigenvalue Problem." In: *Neural Computation* 10.5 (1998), pp. 1299–1319. DOI: 10.1162/089976698300017467.

[142] R. R. Coifman et al. "Geometric diffusions as a tool for harmonic analysis and structure definition of data: Diffusion maps." In: *Proceedings of the National Academy of Sciences* 102.21 (2005), pp. 7426–7431. DOI: 10.1073/pnas.0500334102.

[143] Ronald R. Coifman and Stéphane Lafon. "Diffusion maps." In: *Applied and Computational Harmonic Analysis* 21.1 (2006). Special Issue: Diffusion Maps and Wavelets, pp. 5–30. DOI: https://doi.org/10.1016/j.acha.2006.04.006.

[144] Michele Ceriotti, Gareth A. Tribello, and Michele Parrinello. "Simplifying the representation of complex free-energy landscapes using sketch-map." In: *Proceedings of the National Academy of Sciences* 108.32 (2011), pp. 13023–13028. DOI: 10.1073/pnas.1108486108.

[145] Laurens van der Maaten and Geoffrey Hinton. "Visualizing Data using t-SNE." In: *Journal of Machine Learning Research* 9.86 (2008), pp. 2579–2605. DOI: 10.1103/PhysRevB.48.16929.

[146] F. Pedregosa et al. "Scikit-learn: Machine Learning in Python." In: *Journal of Machine Learning Research* 12 (2011), pp. 2825–2830. DOI: 10.1103/PhysRevB.48.16929.

[147] Miguel A. Caro. "Optimizing many-body atomic descriptors for enhanced computational performance of machine learning based interatomic potentials." In: *Phys. Rev. B* 100 (2 2019), p. 024112. DOI: 10.1103/PhysRevB.100.024112.

[148]   Volker L. Deringer et al. "Gaussian Process Regression for Materials and Molecules." In: *Chemical Reviews* 121.16 (2021), pp. 10073–10141. DOI: 10.1021/acs.chemrev.1c00022.

[149]   Aldo Glielmo et al. "Unsupervised Learning Methods for Molecular Simulation Data." In: *Chemical Reviews* 121.16 (2021), pp. 9722–9758. DOI: 10.1021/acs.chemrev.0c01195.

[150]   Nicholas Metropolis and S. Ulam. "The Monte Carlo Method." In: *Journal of the American Statistical Association* 44.247 (1949), pp. 335–341. DOI: 10.1103/PhysRevB.48.16929.

[151]   David Landau and Kurt Binder. *A Guide to Monte Carlo Simulations in Statistical Physics*. 5th ed. Vol. 48. Cambridge University Press, 2021, pp. 16929–16934. DOI: 10.1017/9781108780346.

[152]   Richard LeSar. *Introduction to Computational Materials Science: Fundamentals to Applications*. Vol. 48. Cambridge University Press, 2013, pp. 16929–16934. DOI: 10.1017/CBO9781139033398.

[153]   Daan Frenkel and Berend Smit. *Understanding molecular simulation from algorithms to applications*. eng. 2nd ed. Vol. 48. Computational science series ; 1. San Diego: Academic Press, 2002, pp. 16929–16934. ISBN: 1-281-01974-7. DOI: https://doi.org/10.1016/B978-0-12-267351-1.X5000-7.

[154]   Nicholas Metropolis, Arianna W. Rosenbluth, Marshall N. Rosenbluth, Augusta H. Teller, and Edward Teller. "Equation of State Calculations by Fast Computing Machines." In: *The Journal of Chemical Physics* 21.6 (1953), pp. 1087–1092. DOI: 10.1063/1.1699114.

[155]   J. Staunton, B.L. Gyorffy, A.J. Pindor, G.M. Stocks, and H. Winter. "Density-functional theory and NiO photoemission spectra." In: *Phys. Rev. B* 48 (1993), pp. 16929–16934. DOI: 10.1103/PhysRevB.48.16929.

[156]   Gerrit van der Laan. "Microscopic origin of magnetocrystalline anisotropy in transition metal thin films." In: *Journal of Physics: Condensed Matter* 10.14 (1998), pp. 3239–3253. DOI: 10.1088/0953-8984/10/14/012.

[157]   P. Ravindran et al. "Large magnetocrystalline anisotropy in bilayer transition metal phases from first-principles full-potential calculations." In: *Physical Review B* 63 (2001), p. 144409. DOI: 10.1103/PhysRevB.63.144409.

[158]   C. T. Chen et al. "Experimental Confirmation of the X-Ray Magnetic Circular Dichroism Sum Rules for Iron and Cobalt." In: *Phys. Rev. Lett.* 75 (1995), pp. 152–155. DOI: 10.1103/PhysRevLett.75.152.

[159] Masato Kotsugi et al. "Origin of strong magnetic anisotropy in L10-FeNi probed by angular-dependent magnetic circular dichroism." In: *Journal of Magnetism and Magnetic Materials* 326 (2013), pp. 235–239. DOI: https://doi.org/10.1016/j.jmmm.2012.09.008.

[160] I. A. Abrikosov et al. "Competition between magnetic structures in the Fe rich fcc FeNi alloys." en. In: *Physical Review B* 76.1 (2007), p. 014434. DOI: 10.1103/PhysRevB.76.014434.

[161] Liqin Ke. "Intersublattice magnetocrystalline anisotropy using a realistic tight-binding method based on maximally localized Wannier functions." In: *Phys. Rev. B* 99 (2019), p. 054418. DOI: 10.1103/PhysRevB.99.054418.

[162] Alexander B. Shick and Oleg N. Mryasov. "Coulomb correlations and magnetic anisotropy in ordered $L1_0$ CoPt and FePt alloys." In: *Phys. Rev. B* 67 (2003), p. 172407. DOI: 10.1103/PhysRevB.67.172407.

[163] Imseok Yang, Sergej Y. Savrasov, and Gabriel Kotliar. "Importance of Correlation Effects on Magnetic Anisotropy in Fe and Ni." In: *Phys. Rev. Lett.* 87 (2001), p. 216405. DOI: 10.1103/PhysRevLett.87.216405.

[164] Alexander B. Shick, Franti šek Máca, and Peter M. Oppeneer. "Anomalous ferromagnetism of a monatomic Co wire at the Pt(111) surface step edge." In: *Phys. Rev. B* 69 (2004), p. 212410. DOI: 10.1103/PhysRevB.69.212410.

[165] Shigehumi Onodera, Yoshikazu Ishikawa, and Keisuke Tajima. "Spin Dynamics in Invar ($Fe_{65}Ni_{35}$, Fe_3Pt) and Non Invar ($Fe_{50}Ni_{50}$) Alloys." In: *Journal of the Physical Society of Japan* 50.5 (1981), pp. 1513–1522. DOI: 10.1143/JPSJ.50.1513.

[166] Qingguo Wei, Stuart Alan Gilder, and Bernd Maier. "Pressure dependence on the remanent magnetization of Fe-Ni alloys and Ni metal." In: *Physical Review B* 90 (2014), p. 144425. DOI: 10.1103/PhysRevB.90.144425.

[167] Li-Yun Tian, Olle Eriksson, and Levente Vitos. "Pressure effect on the order–disorder transformation in $L1_0$-FeNi." In: *Scientific Reports* 10.1 (2020), p. 14766. DOI: 10.1038/s41598-020-71551-4.

[168] Aleksander L. Wysocki et al. "Concentration-tuned tetragonal strain in alloys: Application to magnetic anisotropy of $FeNi_{1-x}Co_x$." In: *Phys. Rev. B* 100 (2019), p. 104429. DOI: 10.1103/PhysRevB.100.104429.

[169] Alexander Edström. "Theoretical and Computational Studies on the Physics of Applied Magnetism : Magnetocrystalline Anisotropy of Transition Metal Magnets and Magnetic Effects in Elastic Electron Scattering." Felaktigt ISBN i den tryckta versionen: 9789155497149. PhD thesis. Uppsala University, Materials Theory, 2016, p. 109. DOI: 10.1103/PhysRevB.48.16929.

[170] Ralf Drautz. "Atomic cluster expansion for accurate and transferable interatomic potentials." In: *Phys. Rev. B* 99 (2019), p. 014104. DOI: 10.1103/PhysRevB.99.014104.